ENHANCING THE RESOLUTION OF SINGLE MOLECULE LOCALIZATION MICROSCOPY USING QUANTUM DOTS AND ADAPTIVE OPTICS FOR IMAGING THICKER SAMPLES

by

KAYVAN FOROUHESH TEHRANI

(Under the Direction of Peter Kner)

ABSTRACT

More than a century after Abbe' discovered the diffraction-limit of a microscope; many new techniques were proposed and demonstrated which allow resolutions beyond the diffraction limit. These methods in general can be placed in two main categories; extension of optical transfer function (OTF), and optical shelving. The former category includes Structured Illumination microscopy (SIM), and the latter includes techniques such as Stimulated Emission Depletion (STED), and Single Molecule Localization (SML).

In this dissertation we focus our attention to improving the resolution of SML; the accuracy of which is a function of several factors such as the brightness of the fluorophores, and sharpness of the Point Spread Function (PSF). Improvement of the photon emission of fluorophores have been addressed by the development chemical buffers that facilitate blinking with higher brightness, as well as brighter dyes such as Quantum Dots (QD). The QDs promise to improve the resolution by producing 17 times more photons than organic dyes, which dramatically increases the accuracy of the SML.

The implementation of QD Blueing technique to SML provides a novel approach to overcome the high blinking duty cycle of the QDs. Here we present a novel two color QD blueing SML technique. Another critical challenge in improvement of the accuracy of the SML is by reducing the effect of optical aberrations. Aberrations tend to deviate propagating wavefronts from their flat form, and hence deform the shape of point spread function (PSF), which directly reduces the accuracy of SML. This can be caused by several factors including the imperfections in optical elements design, misalignments, and external factors such as refractive index mismatch in the propagating media. While the first two can be optimized by using aberration corrected elements and more effort on alignment, the latter cannot be reduced without the help of active optical elements. Biological samples induce aberrations due to their shape, and diversity of refractive index along their body. In this dissertation we demonstrate use of Adaptive Optics (AO) for compensation of wavefront aberrations for SML imaging on thick biological samples.

INDEX WORDS: Fluorescence Microscopy, Super-resolution, Single Molecule Localization microscopy, Quantum Dots, Wavefront correction, Adaptive Optics

ENHANCING THE RESOLUTION OF SINGLE MOLECULE LOCALIZATION MICROSCOPY USING QUANTUM DOTS AND ADAPTIVE OPTICS FOR IMAGING THICKER SAMPLES

by

KAYVAN FOROUHESH TEHRANI

BS, Azad University, Iran, 2005

MS, University of Nottingham, United Kingdom, 2009

A Dissertation Submitted to the Graduate Faculty of the University of Georgia in Partial Fulfillment of the Requirements for the Degree

DOCTOR OF PHILOSOPHY

ATHENS, GEORGIA

2015

ENHANCING THE RESOLUTION OF SINGLE MOLECULE LOCALIZATION MICROSCOPY USING QUANTUM DOTS AND ADAPTIVE OPTICS FOR IMAGING THICKER SAMPLES

by

KAYVAN FOROUHESH TEHRANI

Major Professor:	Peter Kner
Committee:	Mark A. Haidekker
	Mable Fok

Electronic Version Approved:

Suzanne Barbour
Dean of the Graduate School
The University of Georgia
August 2015

DEDICATION

I would like to dedicate this dissertation to my mother Afsaneh, my father Mohammad reza, my sister Katayoun, my grandmother Afshan, my late grandfather Mohammad hossein who wanted to see me as “Engineer”, and my best friend and soul mate Nahal, for their love and unconditional support throughout my studies.

ACKNOWLEDGEMENTS

I would like to express my deepest appreciation to my advisor Dr. Peter Kner for the knowledge of optics and microscopy I have gained from him. This dissertation would not have been possible without his continual guidance and persistent support.

I am indebted to my committee member Prof. Mark Haidekker for his knowledge of biomedical imaging and image analysis. His dedication to teaching and transfer of knowledge is exemplary. I would also like to extend my gratitude to my committee member Dr. Mable Fok for her time and support during this PhD work.

This dissertation is part of collaboration with three other universities and Boston museum of science, called QSTORM. I would like to thank the involved teams Dr. Jessica Winter's lab – Ohio State University, Dr. Ge Yang's lab - Carnegie Mellon University, Dr. Beth Brainerd's lab – Brown University, Carol Lynn Alpert – Boston museum of science, and Dr. Jianquan Xu. We improved our imaging techniques and performed more Adaptive Optics experiments using Jianquan's expertise and knowledge in cell culture and chemistry of the buffers.

In addition I would like to cordially thank Dr. Ping Shen and Ms. Yiwen Zhang whose help with providing *Drosophila* samples were an integral part of our Adaptive Optics experiments. I would also like to thank, Dr. William Kissalita for letting us use his lab for cell culture. As well as Dr. James Lauderdale who thought me the cell culture

process and let me use his cell culture lab for this purpose. I also like to thank Dr. Edward Kipreos and Ms. Snehal Chaudhari who provided us with *C.elegans* round worms. Images of *E.Coli* were obtained during collaboration with Drs. Jason Locklin, Vincent Starai, and Mr. Jeremy Yatvin, for which I am grateful.

A special thank you to my friend Thomas Huelsnitz; for being a great friend when his help was needed. And thank you to my lab mates Benjamin Thomas, Xiaolong Zhang, Andrew Herrington, and the newest member of Kner lab Keelan Lawrence, for providing a pleasant environment for study and research.

TABLE OF CONTENTS

LIST OF TABLES

LIST OF FIGURES

1. INTRODUCTION

Biomedical and biological imaging can be placed in two large categories; light microscopy and modalities which use other electromagnetic waves for projection of an image. The latter modalities - except Electron microscopy (EM) – are used to observe large internal tissues, with resolutions typically fall in micrometer and millimeter range. As can be seen in Figure 1-1, at one end we have Positron emission tomography (PET) [1] that by detection of positron emitting isotopes can reach about 1 cm resolution. Magnetic Resonance Imaging (MRI)[2] and Optical Coherence Tomography (OCT) have improved the resolution of imaging to about 1-100 μm. Light microscopy however by using photons image with resolution down to 200 nm. In biological imaging, it is very often necessary to identify particular parts of the subject under study such as a cell with a marker that can be distinguished from other organelles in the cell. Using Fluorescence microscopy techniques, specific parts of a sample can become fluorescent, and therefore can be separated by spectral filtering. This provides specificity for a particular protein under study, which is not available to transmission light microscopy. At the end of the resolution spectrum is the Electron Microscopy (EM). EM which was invented in 1931 by Ruska and Knoll [3], uses electrons instead of photons. The wavelength of an electron beam is given by plank's constant divided by the momentum of an electron. It can therefore produce wavelength of less than 1 nm, and hence a resolution of less than 1nm. However, because the variation of refractive index in biological samples is not

significant, EM shows lower contrast than Fluorescence microscopy, even though it provides 2 order of magnitude better resolution.

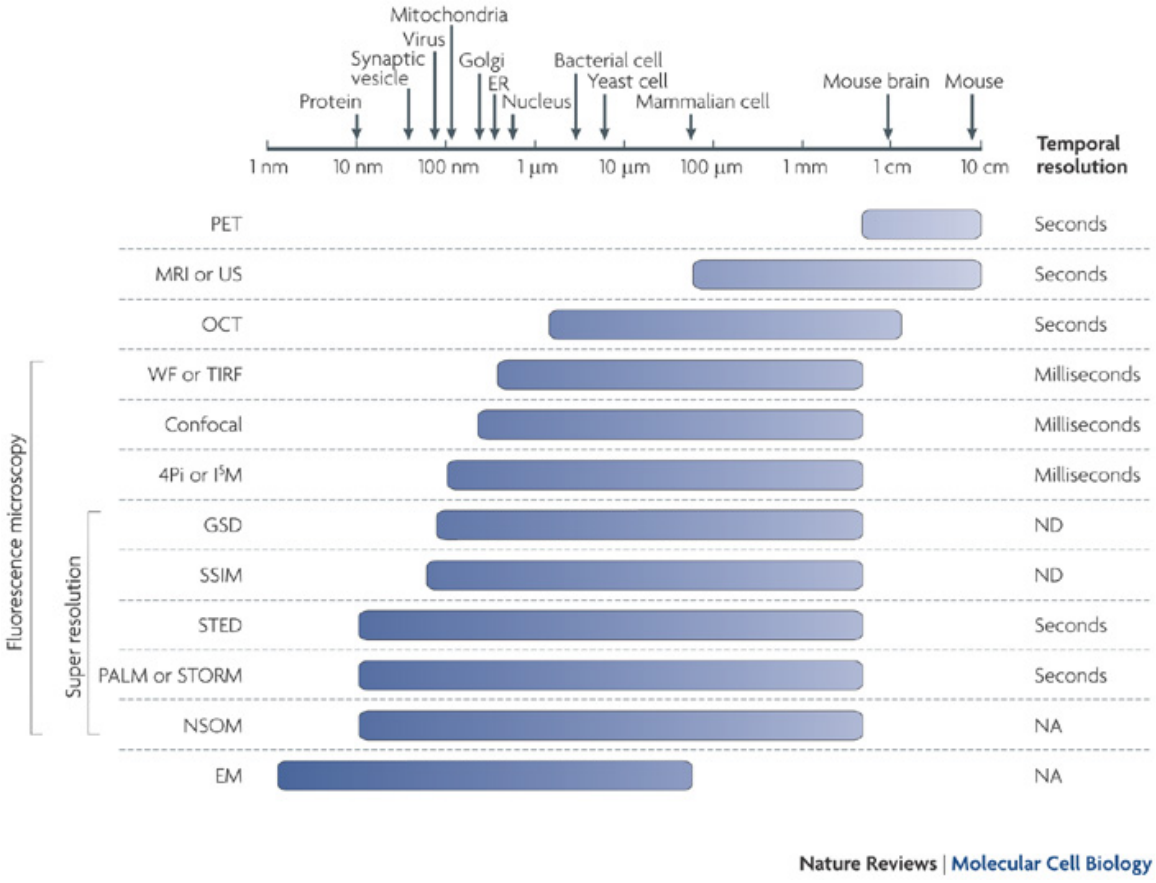

Figure 1-1 Comparison of different biomedical/biological imaging modalities. Adapted from [4].

Fluorescence microscopy was first reported by Heimstadt (1911) [5] and Lehman (1913)[6]. Several techniques can be used to label the required organelle of a cell with fluorophores, such as Immunocytochemistry/Immunohistochemistry, transfection, and direct binding. Since the fluorophores are attached only to the specific part, by their excitation and filtering of the excitation light, the specific part can be distinguished from the rest of the structure. This has made Fluorescence microscopy an essential tool for biologist to study many fine structures in cells, or other biological molecules, as well as

studying events inside living organism, tissues, and animals. Another advantage of light microscopy over EM is its harmless nature and compatibility with living organisms.

Nonetheless, light microscopy's resolution is limited to about 200 nm. In the late 19^{th} century Ernst Abbe performed several experiments with diffraction patterns. He showed that by passing a limited number of diffraction orders, the resolving power would be limited. He described this limit –known as the diffraction limit- and demonstrated the minimum possible distance resolvable is the wavelength of light divided by the Numerical Aperture of the optical system [7, 8]. Later Helmholtz performed similar experiments and derived the equation for the diffraction limit [9]. The diffraction limit will be discussed in detail in section 1.2.3 later in this chapter.

However there are many structures and events in cells that require finer resolving power to become visible, such as the tracking of synaptic vesicles and intersection of chromosomes [10]. Several techniques have been developed in the past two decades to overcome the diffraction limit. These approaches can be placed in two main categories: Near-field, and Far-field super-resolution techniques. Near-field microscopy unlike far-field uses probes to collect light from an object. We divide Far-field methods into three main categories. First category is methods that try to narrow down the size of PSF and by scanning the sample an image is created. Stimulated Emission Depletion (STED)[11], and Ground State Depletion (GSD)[12] fall into this category. The second category are the methods that enlarge the Optical Transfer Function (OTF) [13] to improve spatial bandwidth of the optical system, these methods include the Lukosz's microscope, Structured Illumination Microscopy (SIM) [14] and its saturated version. The last category – and the focus of this dissertation - is the Single Molecule Localization

Microscopy (SML) which relies on the principle of single fluorophores blinking. The blinking lets individual fluorophore be isolated from their ensemble and accurately localized provided that enough photon are collected and PSF is intact. These methods include Photo-activable Localization Microscopy (PALM)[15], f-PALM[16], Stochastic Optical Reconstruction Microscopy (STORM)[17] and d-STORM [18].

In this chapter we first present our objectives. An introduction to super-resolution microscopy comes afterwards. It is followed by introduction to Adaptive Optics methods.

1.1. Objectives

The aim of this dissertation is to show enhancement of resolution for Single Molecule Localization microscopy (SML) by two approaches, using quantum dots as fluorescent probes, and implementation of Adaptive Optics (AO) for imaging deeper inside a tissue. The minimum resolvable distance (resolution) of SML imaging is directly dependent on the width of the Point Spread Function (PSF), and inversely dependent on the Number of collected photons. Quantum Dots produce more photons than organic dyes, hence improving the resolution [19]. Adaptive Optics helps improving the optical aberrations induced by biological samples, and enable imaging further inside a tissue [20].

1.2. Introduction to super-resolution methods

In this section we first introduce fluorescence microscopy, and then discuss the limits of resolution. This is followed by the techniques which enable resolutions beyond the diffraction limit. We first introduce the first super-resolution technique introduced by Lukosz, and then discuss the STED, SIM and SML techniques.

1.2.1. Properties of an optical microscope

For better understanding of the properties of a microscope we like to introduce the concept of Point Spread Function (PSF) and Optical Transfer Function (OTF) for a 4f optical system. Configuration of a 4f imaging system is shown in Figure 1-2. PSF is the impulse response of the optical system.

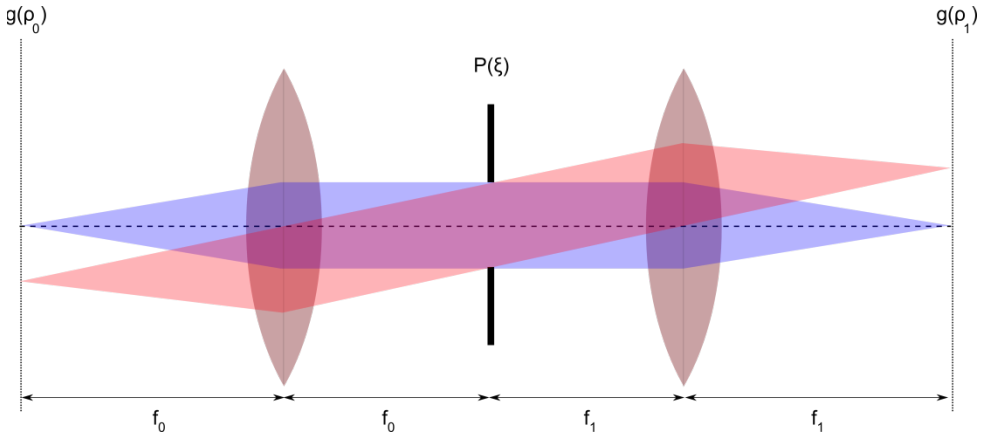

Figure 1-2 - Diagram of a 4f imaging system.

The image can be related to the object by convolving the PSF and the object:

$$g_2(\rho_2) = h(\rho) \otimes g_1(\rho_1) \tag{1.1}$$

where h is the PSF. The PSF of a coherent (h) and an incoherent (h_i) system can be found:

$$\begin{aligned} h(\vec{\rho};\vec{\xi}) &= \int P\left(\vec{\xi}\right) e^{i2\pi\frac{\kappa}{f_0}\vec{\rho}.\vec{\xi}} d^2\vec{\xi} \\ h_i(\vec{\rho};\vec{\xi}) &= \left|h(\vec{\rho};\vec{\xi})\right|^2 \end{aligned} \tag{1.2}$$

where κ is the wave number n/λ, P is the pupil function, and f is the focal length. The OTF is given by:

$$\widetilde{H}(\xi) = \mathcal{F}\{h_i\} \tag{1.3}$$

1.2.2. Fluorescence Microscopy

The self-luminous nature of fluorophores helped scientist over a century ago to develop a new microscopy modality which allowed specific biological structures to be selectively imaged. Unlike absorption light microscopy, in fluorescence microscopy the illumination light is filtered and only the emitted light from the sample is observed. As shown in Figure 1-3 the light emitted from the source is transmitted through an excitation filter, which selectively passes the part of light spectrum suitable for excitation of the fluorophore under study. Then the light emitted from the fluorophore (inside the biological sample) is reflected on the surface of the dichroic mirror and transmitted through the emission filter. This way only the light emitted from specific fluorophore will be detected and the rest of the spectrum is blocked.

Fluorescence microscopy as developed by Heimstadt and Lehman [5, 6] used a high powered arc lamp to generate UV, along with a modified Wood's filter (nitrosodimethylaniline solution with copper sulphate) as excitation filter and a Uviol emission filter, on a dark field setup. The aim of the study was to observe autofluorescence from bacteria, protozoa, plant and animal tissues, and bio-organic substances.

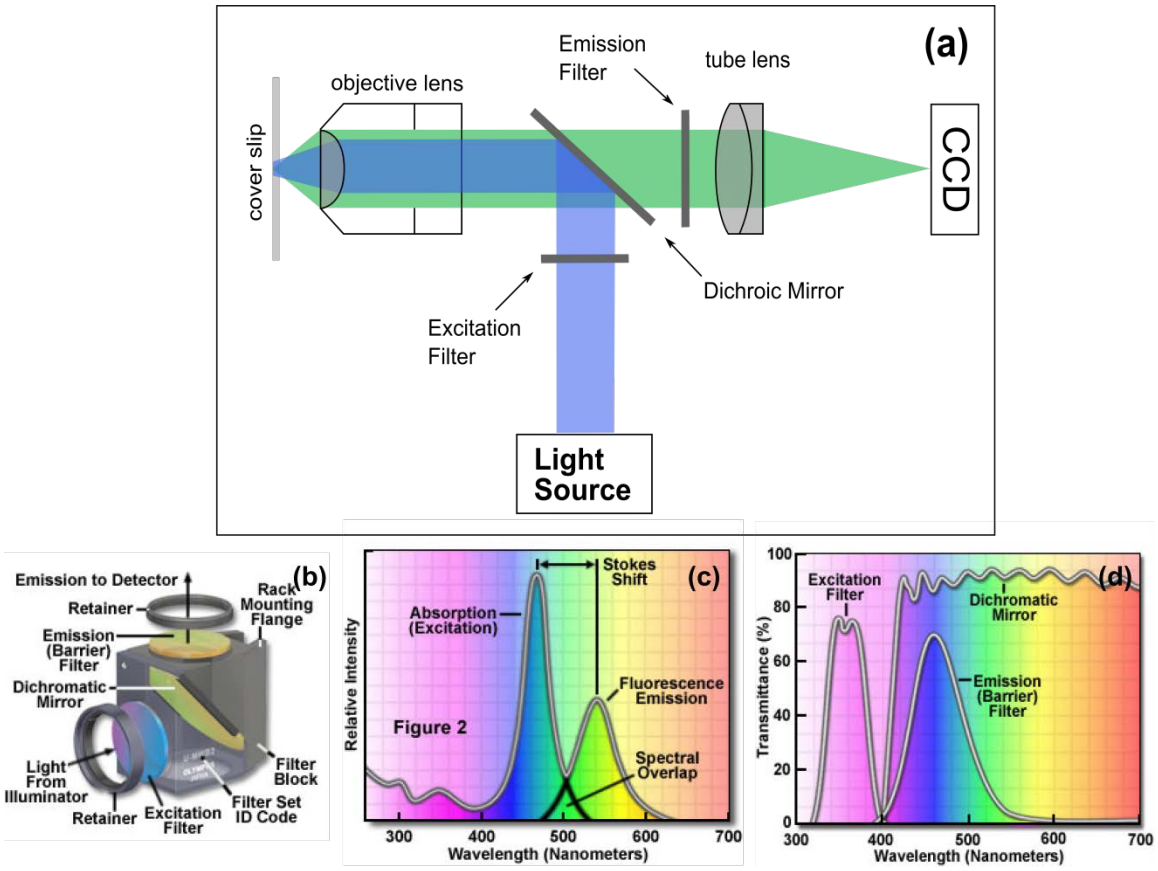

Figure 1-3 – A diagram of fluorescence microscope is shown in (a). The actual filter cube that is usually used in microscopes is shown in (b). A typical Excitation and emission spectral diagram of a fluorochrome is shown in (c). Pass-bands of a typical fluorescent cube including excitation and emission filters, and the dichroic mirror are illustrated in (d). Credit for (b-d): Olympus microscopy.

Since then, this technology has developed significantly in many directions. Introduction of Laser and LED illumination as well as improvements in filter/dichroic technologies have enhanced Fluorescence microscopy. Many different dyes with high brightness have been introduced to illuminate specific parts of cells. In general, two classes of probes are used for super-resolution imaging: fluorescent proteins (FPs) and non-genetically encoded probes, such as organic small-molecule fluorophores and quantum dots. Techniques such as Fluorescent life time imaging (FLIM) and Forster resonant energy transfer (FRET) have also introduced to study interaction between

molecules [21]. Binding mechanism of fluorophores have also progressed; direct binding, transfection, and immuno-hystochemistry/cytochemistry are among the methods.

However all of these techniques have the same limitation of resolution as other light microscopy techniques, the diffraction limit. In the next section we discuss the diffraction limit.

1.2.3. Diffraction limit

What is known as the diffraction limit was first observed and formulated by Ernst Abbe in 1873 [8], later Lord Rayleigh [22] and Sparrow [23] also formulated the same phenomenon.

Abbe observed that light gets blurred when it is focused to a spot. He realized that the size the spot is what is limiting the resolving power of an imaging system. The spot is called the Point Spread Function (PSF). He showed that the size of the spot and thus the lower bound of resolution is:

$$\Delta x = \frac{\lambda}{NA} \tag{1.4}$$

$$NA = n \times \sin\theta \tag{1.5}$$

where Δx is the minimum distance measurable laterally, λ is the wavelength of light, and NA is the numerical aperture where n is the refractive index of the surrounding media, and θ is the maximum angle of incidence. Since most of modern optical objective lenses have NAs of less than 1.5, and the wavelength of light has to be longer than UV (>400nm) to be non-destructive to biological samples; the minimum

size of PSF is about 250nm. As shown in Figure 1-4 due to diffraction when the two structures are in close proximity (less than the diffraction-limit) of each other, it would be impossible to recognize them individually; rather an ensemble of them would be observed. Some biological entities with their approximate sizes are compared to diffraction limit in Figure 1-5.

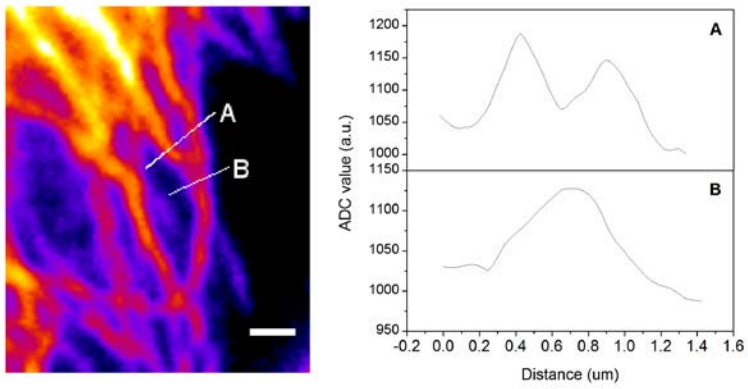

Figure 1-4 – Microtubules of a cell are shown in the left panel. As the two microtubules merge the imaging system becomes unable to distinguish between the two. Cross-sections of A and B are shown in the right panel. Scale bar is 1 µm.

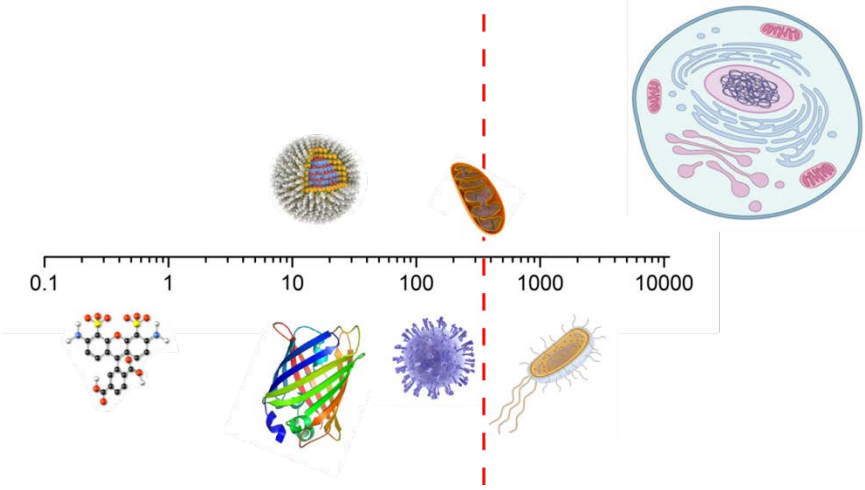

Figure 1-5 Size comparison of some typical biological imaging entities with the diffraction limit. From left to right: an Alexa Fluor 488 molecule, a fluorescent protein, a Quantum Dot, Influenza virus, Mitochondrion, bacterial cell, mammalian cell. The axis is in nano meter.

We mentioned earlier that electrons can produce sub-nano-meter wavelengths. Therefore EM can achieve virtually unlimited resolution, since the minimum resolvable distance is a function of wavelength. However, performing EM on living organisms is non-trivial. Also EM cannot achieve the high contrast of fluorescence microscopy due to self-luminescence of fluorescent probes.

1.2.4. Near Field Scanning Optical Microscopy

The first super-resolved image of a biological sample was obtained in 1992 in Bell Labs [24, 25]. The concept of Near-field scanning optical microscopy (NSOM or SNOM) was originally proposed in 1928 by Synge[26]. But it wasn't until 1984 that visible light NSOM was practically demonstrated [27, 28]. Unlike far-field techniques NSOM uses a sub-wavelength fiber optic with all its sides blocked for light propagation, as shown in Figure 1-6. In a typical NSOM setup, the tip of an optical fiber is narrowed and coated with aluminum to collect only the light from a small region of the sample to propagate in the fiber. Since there is no diffracting element in the setup, such as a lens, the resolution of this method is determined by the size of the aperture. Typical resolutions of 20-120nm have been reported. NSOM has been used to study nanoscale organization of several membrane proteins [29, 30].

Although the method has effectively surpassed the diffraction limit, its inability to image internal structures is a big drawback. Also it requires constant feedback to maintain distance from the surface of the sample, which makes the imaging process very slow for irregularly shaped samples.

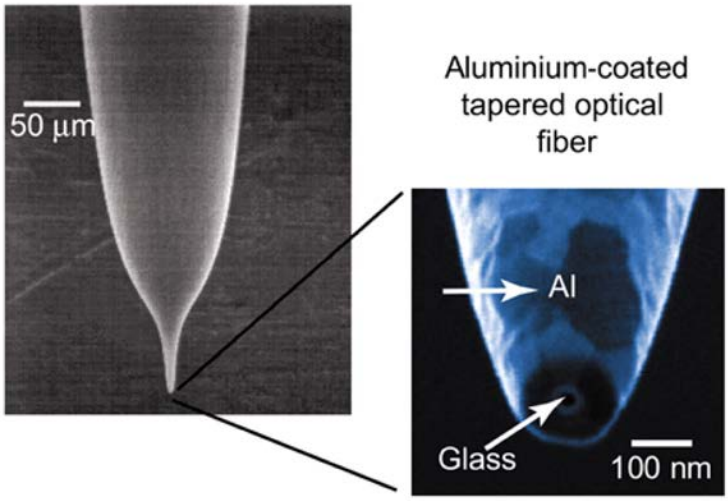

Figure 1-6 - The near-field optical probe. The tip of fiber optic is modified to a final diameter of 20-120 nm. It is coated with aluminum to confine the light to the tip region. The size of the tip determines the resolution of imaging. The surface of the sample is scanned to produce an image. Adapted from [29].

1.2.5. Optical sectioning methods

All the near field and far field techniques that we are presenting here suffer from poor axial resolution. Several approaches have been made to overcome this problem, including scanning methods (i.e. confocal [31-34]), Interferometric two or more objective imaging such as I^nM [35] and 4Pi microscopy [36], and non-linear approaches, e.g. two-photon microscopy. In this section we briefly present these methods, since they are sometimes combined with super-resolution techniques to improve their axial resolution. A comparison diagram of axial and lateral OTFs and PSFs of different microscopy methods is shown in Figure 1-7. We can see that the poor axial and lateral resolution of wide-field microscopy has improved using the techniques that we will discuss here.

1.2.5.1. Confocal microscopy

Confocal is a method of scanning fluorescence microscopy that was developed in the late 1970s and early 1980s [37]. There are several configurations used for confocal

microscopy[32], but in general the technique focuses the excitation light to a point on the object – in contrast to wide field where a large part of the object is illuminated. The emitted light from the sample is then detected through a pinhole. The pinhole then rejects most of the out of focus light and renders an image with sharper details. This way axial resolution is improved and optical sectioning becomes possible. Confocal also promises to improve the lateral resolution, given the pinhole size is equal or smaller than the diffraction limit, by a factor of 1.4 (or 2 with image processing)[38-40].

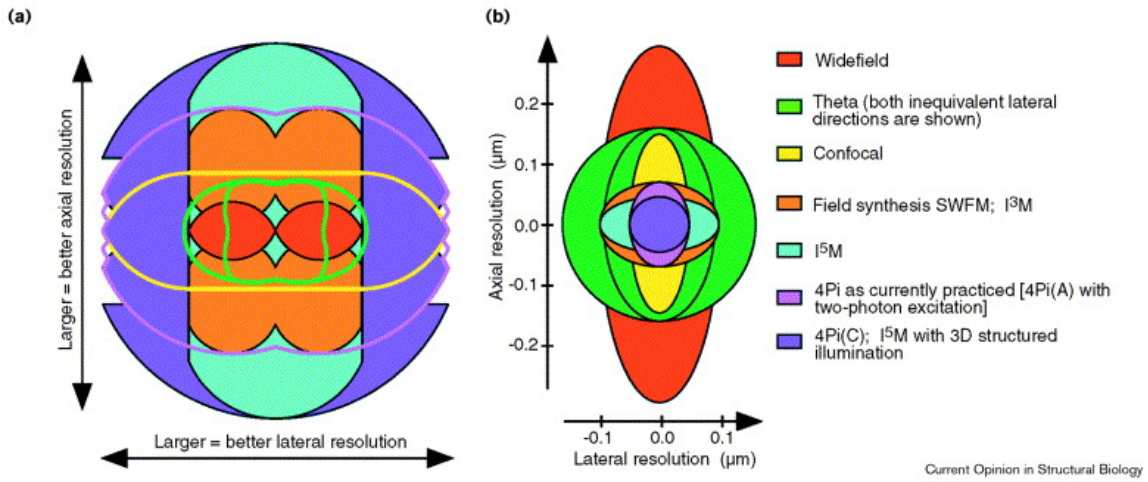

Figure 1-7 – Comparison of OTF (a) and PSF (b) of different microscopy techniques. Adapted from [41]

1.2.5.2. Imaging using two objective lenses

Another concept in improving the resolution is by collecting of light from larger angles [41]. In other words by increasing NA, the resolution will improve. But NA is limited to maximum of 1.4, due to the index of refraction of glass. One way to overcome

this problem is by collecting light from multiple directions. I^nM microscopy uses two objectives in opposing direction [42, 43].

The term I^nM is collectively given to three techniques, Image Interference Microscopy (I^2M), Incoherent Interference Illumination Microscopy (I^3M), and the combination of these two is called I^5M. Although I^2M improves the angles of light collection, by applying interference illumination I^3M takes advantage of standing wave illumination to improve its axial resolution as can be seen in Figure 1-8. The figure also illustrates how I^5M takes advantage of both methods and improves its axial resolution even further.

4pi microscopy is a scanning method of I^nM [36]. 4pi (A), (B), and (C) are scanning equivalents of I^3M, I^2M, and I^5M. Application of scanning improves both the axial and lateral resolutions, as shown in figure Figure 1-7.

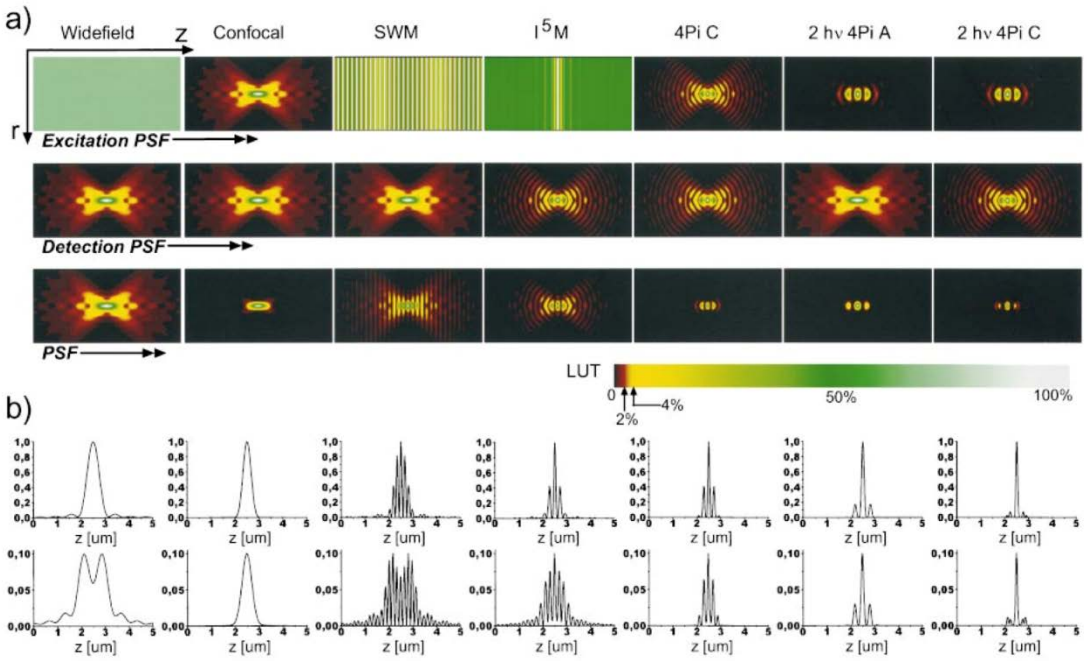

Figure 1-8 – Excitation, detection and effective point spread functions of several microscopy modalities are compared in upper, middle and lower panels of (a) respectively. In (b) axial profiles of the effective PSFs are shown. The upper row shows the profile along the optical axis and the lower row shows the profile at an offset point with 10% of intensity found in geometric focal point. Adapted from [44]

1.2.5.3. Two-photon microscopy

The next method we are discussing here takes advantage of non-linear transition behavior of fluorophores, and scanning techniques. Two-photon microscopy [45-47] is based on the idea of multi-photon absorption that has been used for many years in spectroscopy [48-52] in second and third harmonic generation (SHG, THG), and CARS microcopy techniques. SHG works on the principle of producing twice the frequency by simultaneous absorption of two photons at the original frequency. The concept was first described by Franken et al. in 1961 and experimented in a quartz crystal using a ruby laser [53]. It was later used for microscopic imaging in 1970s by Sheppard and his team [54, 55]. Both SHG [56-58] and THG are also applied to biological imaging [59-61].

Two-photon microscopy however is a fluorescence microscopy technique that uses near-simultaneous absorption of two photons of a wavelength to excite fluorescent molecules that absorb at half of that wavelength (double the frequency as in SHG). The first two-photon fluorescence excitation was done in 1961 by Kaiser and Garret [62]. The advantage of this method is that by using longer wavelength there would be less scattering and hence deeper tissue penetration can be achieved. In fact the excitation from two-photons makes the final PSF a product of the two PSFs Considering the Gaussian profile of the PSFs, the product has half the width of a single PSF. The squared PSF reduces most of the excitation PSF's side-lobes and hence the out-plane illumination is reduced, as shown in Figure 1-8. This helps improving the axial resolution, enables optical sectioning, and reduces photo-bleaching of out-of-plane fluorophores. Lateral resolution improvement is not as plausible due to longer wavelength the original PSF which makes it double in size, and the factor of two improvements makes it equal to excitation with the shorter wavelength – even though the reduction in side lobes improves resolution [63, 64].

1.2.6. Lukosz OTF expansion mode

Lukosz proposed the concept of expansion of OTF in late 1960s [65, 66]. The principle of the optical arrangement giving increased resolution is sketched in Figure 1-9. Two gratings with optically equivalent grating constants are placed in the conjugate planes at M and M', which means that the ratio of the gratings constants should be equal to the lateral magnification between M and M'. The grating at M split the spherical beam from the object plane into two diffraction orders P^{-1} and P^{+1}. The two spherical waves imaged at the image plane as P'^{-1} and P'^{+1}. The two beams are split again at M'. By

slightly rotating the grating and masking the unwanted diffraction orders, the system effectively transfers double spatial bandwidth in x direction (kx) as a normal optical system can pass. Although this technique can be expanded to y direction, due to technical limitations of the time did not gain popularity, until 1990's when Structured illumination technique used a similar approach to increase the resolution.

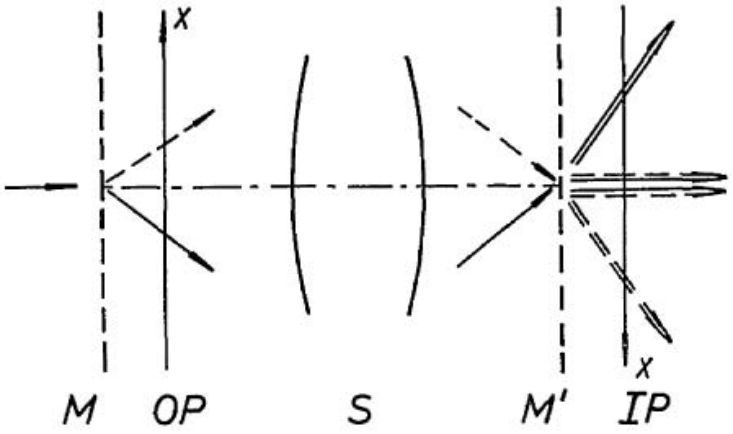

Figure 1-9 – Diagram of Lukosz's optically resolving system. Two gratings M and M' that each produce two diffraction orders are placed into optically conjugate planes of object and image space. OP and IP are object and image planes. Adapted from [65]

1.2.7. Stimulated Emission Depletion Microscopy (STED)

To go beyond the diffraction limit STED techniques takes advantage of another non-linear molecular transition behavior. STED illumination consists of two beams, a Gaussian excitation beam and a hollow doughnut beam with the same or slightly red-shifted wavelength –called STED beam [12, 67]. The role of the STED beam is to take the excited fluorophores back to ground state, or by an inter-system crossing to triplet state as used in Ground state depletion (GSD) technique. The STED beam is modified such that its center has zero intensity, although both beams are diffraction limited. Therefore the fluorophores excited at the center of the beam are unaffected, but the surrounding ones are put to a non-radiative state, narrowing the effective excitation PSF.

The two beams are shown in Figure 1-9. The beam is then scanned through the object and an image is reconstructed. The application of STED to biological imaging was the first far-field super-resolution microscopy technique reported [68]. STED microscopy achieved 100 nm resolution with single objective [69] but its combination with 4pi concept made it to 20 nm resolution in the focal plane [70, 71] and 45 nm resolution in all three dimensions [72]. The resolution of STED is estimated by [73]:

$$\Delta x \approx \frac{\lambda}{2NA\sqrt{1+\frac{I_{\max}}{I_{sat}}}} \tag{1.6}$$

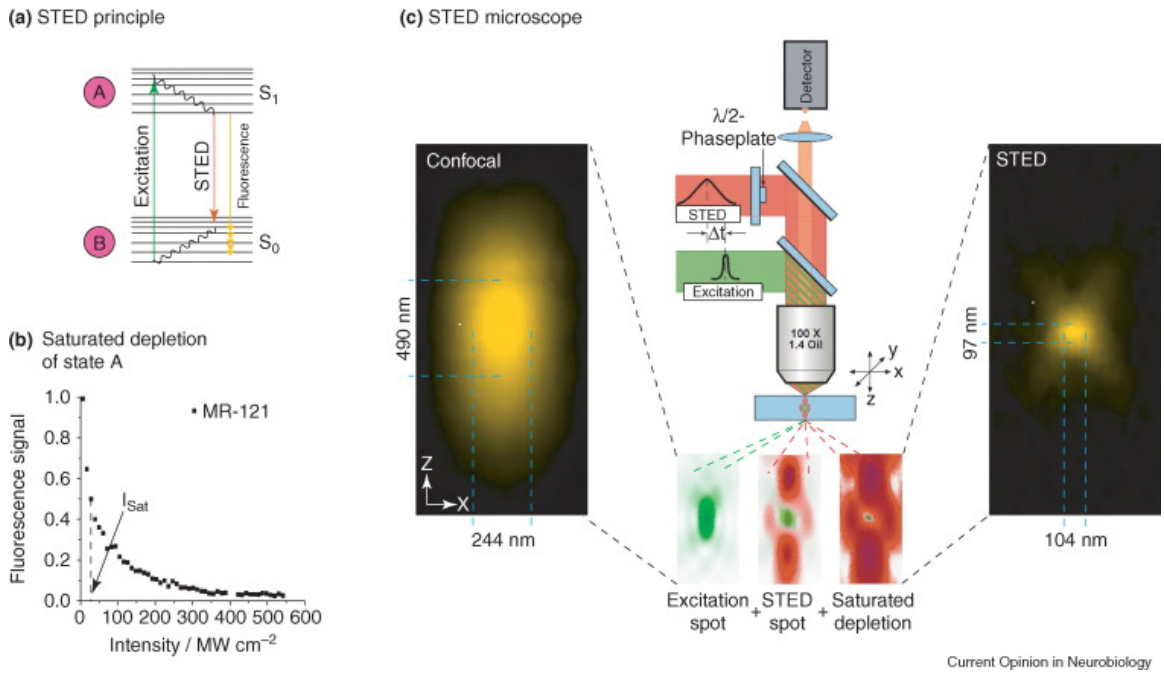

Figure 1-10 – Principle of STED. Energy transitions are shown in (a). A fluorophore is excited by the main beam, and depleted by the STED beam. (b) shows non-linear effect of intensity to the fluorescence of signal. (c) illustrates a typical STED microscope, where the conventional PSF is made smaller using the STED beam. Adapted from [74]

where I_{max} and I_{sat} are the maximum intensity of the STED beam, and the saturation intensity of the fluorescence transitions. In fact the equation shows that the

classical limit of resolution can theoretically be improved by $\sqrt{1 + I_{max}/I_{sat}}$ even with a small I_{max}. As I_{max} approaches infinity ∂x goes toward zero.

STED has later been improved by taking advantage of inter-system crossing and taking them back to radiating state. The fluorescence mechanism of the technique called Ground State Depletion is sketched in Figure 1-10. In the original STED only the transition from ground state to the first singlet state was depleted to narrow the excitation beam. In Ground State Depletion (GSD) the transition from the first singlet state to the first Triplet state is also engaged to improve the resolution.

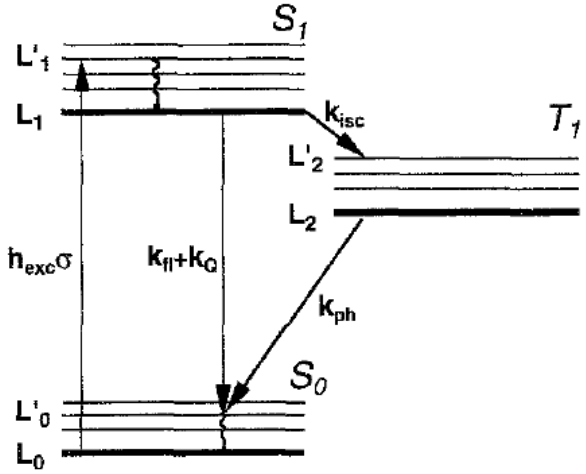

Figure 1-11 – Jablonski diagram of energy states of a typical fluorophores. S0, S1, and T1 are the ground, singlet, and Triplet states. $L_{0\text{-}2}$ show their respective relaxed vibrational level, where $L'_{0\text{-}2}$ are higher vibrational level with relaxations in order of picosecond. Adapted from [12]

The Jablonsky diagram of Figure 1-11 shows the energy states of a typical fluorescent molecule. Due to the low laser power used, only vibrational relaxed levels of ground, singlet and triplet states L0, L1, and L2 are populated enough to be considered for this purpose. Like STED the fluorophores at the point of interest are excited to L1, where the surrounding molecules are depleted using the STED beam. When the STED

beam is turned off, most molecules are relaxed from L1 and return to L0. However for a short period of time, a fraction of the molecules are still trapped in L2. Since the population density at L2 is much lower than L1, GSD can achieve an improved resolution over the classical STED.

1.2.8. Structured Illumination Microscopy (SIM)

SIM is a method of breaking the diffraction limit by spreading the extents of the OTF. It was first proposed in 1999 and then experimentally proven in 2000 [14, 75]. One way to explain this effect is by Moiré patterns. When two patterns of certain spatial frequencies overlap (or multiplied), a new pattern with new frequencies in k_x and k_y directions are produced. The phenomenon can be used with a known pattern projected onto an unknown object. Knowing the product, and the original pattern the object can be reconstructed.

In optical terms, the expansion of the OTF limits can be explained by the convolution in the frequency domain of the illumination pattern and the system's OTF. OTF extents of a typical optical system are shown in Figure 1-12 (a), with the radius of $2NA/\lambda$. A stripe pattern has frequency components as shown with dots in part (c). Having these two patterns at the back pupil plane, produces a convolution of the two as shown in part (c), which has extended the OTF to twice the frequency support as it could get conventionally, in one direction. Now by rotating the pattern more frequencies can be covered Figure 1-12 (d).

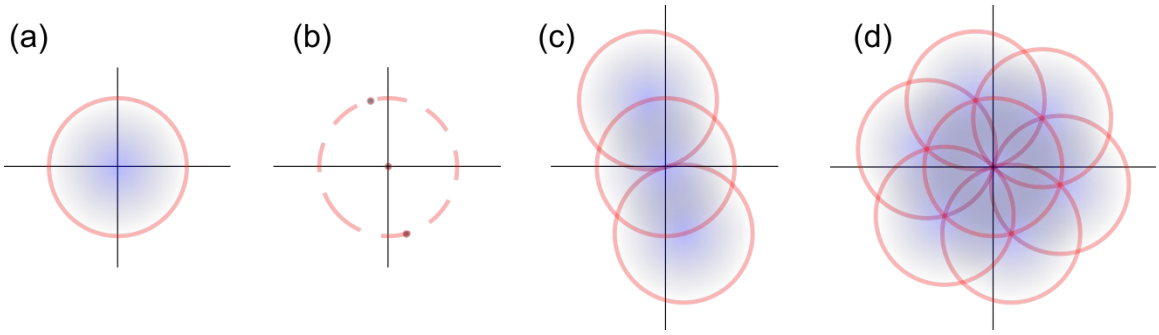

Figure 1-12 – Concept of OTF expansion by structured illumination. (b) shows limits of a classical diffraction limited OTF. Support amplitude is shown in blue. The dots in (b) are showing the non-zero frequency contents of a stripe pattern. The convolution of the Original OTF and the stripe pattern's frequencies is shown in (c). By rotating the pattern more frequencies can be covered.

This concept can be extended to 3D, by generating patterns with frequency components in k_z direction. Usually three beams are used to create 3D interference patterns. Such patterns with non-zero frequency components in kz direction, can fill the OTF support in 3D. One problem that can be addressed is the 'missing cone'. By extending the OTF the missing cone is filled, and therefore the axial resolution can be improved and enables optical sectioning [76].

With images taken at different directions, frequency information needs to be extracted from their Fourier transforms. One way to differentiate between the images taken at one direction (for 2D SIM) is to take 3 images with different phases. The frequency components can then be separated from each other mathematically. By cross-correlating the overlapping parts of the frequency domain information, they can be reconstructed to a larger OTF as shown in Figure 1-12(d). Now inverse Fourier transforming the OTF would return an image with double the resolution of conventional method. Experimental examples of SIM are shown in Figure 1-13.

Non-linear or saturated SIM (SSIM) is another method that takes advantage of fluorescence non-linearity [77]. In SSIM, saturation of the fluorophores helps with generation of more harmonics. By having more frequency components covered, resolution down to 50nm has been achieved. Figure 1-13 (i-o) shows the experiment of non-linear SIM on 50nm fluorescent beads.

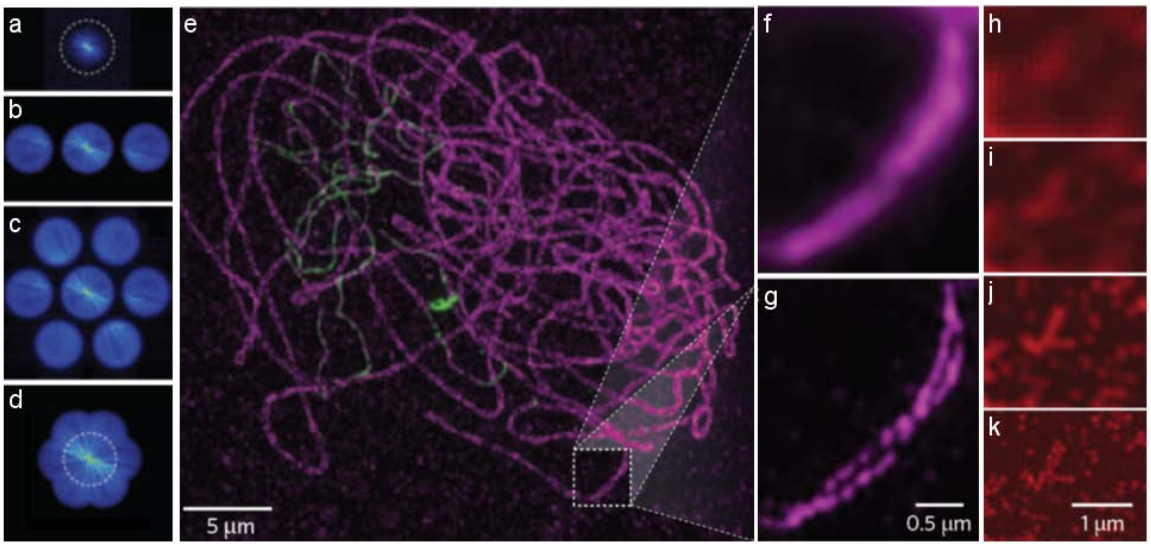

Figure 1-13 – SIM explained by examples. (a) shows Fourier transform of a conventional widefield image. The diffraction limit is highlighted with a dashed circle. Different orders of information are acquired in (b,c), to make the extended OTF shown in (d). (e-g) show an example of 3D SIM. (h-k) are non-linear SIM images of 50 nm fluorescent beads. (a-d), (e-g), and (h-k) are adapted from [78],[76], and [77] respectively.

1.2.9. Single Molecule Localization microscopy techniques (SML)

Unlike other techniques mentioned, SML does not require special beam shaping to improve the resolution. It is based on a very simple principle; finding position of each fluorophores by isolating them from their ensemble [15-17]. If only one molecule is emitting photons in a PSF volume then its center can be estimated by applying fitting. By repeating this process and acquiring information from all the dyes in one PSF volume, sub-diffraction-limit resolution can be achieved. Therefore most dyes must stay in dark

state and only a sparse subset of them can be in on state. When most of the dyes are localized, by putting these points together, a super-resolution image can be reconstructed. This process is shown in Figure 1-14.

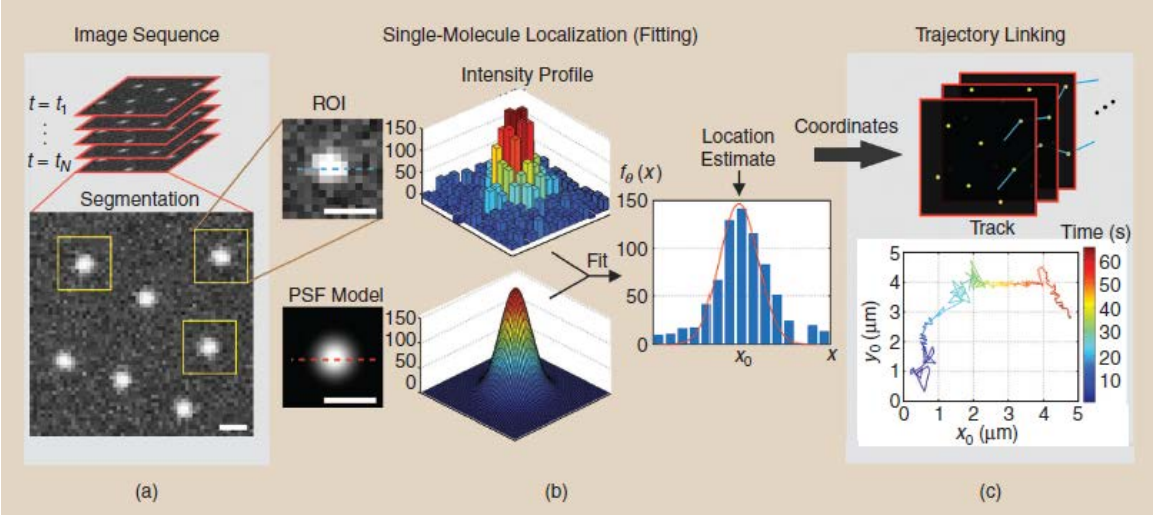

Figure 1-14 – Process of SML. Data acquisition (a) is done by imaging the blinking events for several thousand frames. Fitting is applied to the PSFs and their center is estimated (b). And finally a high-resolution image is constructed (c). Adapted from [79].

Several techniques have been developed in the past decade to induce blinking of different fluorophores, such as Photo-Activatable Localization Microscopy (PALM) [15], and fluorescent PALM (fPALM) [16], that exploit fluorescent proteins, Stochastic Optical Reconstruction Microscopy (STORM) [17] that takes advantage of FRET from a pair of dyes to induce photo-switching, and direct STORM which uses the non-linear characteristic of molecular transitions explained for GSD to achieve blinking. Points Accumulation for Imaging in Nanoscale Topography (PAINT) [80-83] is another single method that takes advantage of changes in emission spectrum of a fluorophore (Nile Red) upon its binding to an intracellular hydrophobic membrane. Super-resolution optical fluctuation imaging (SOFI) [84] is another technique that reconstructs higher resolution images by fluctuations in the intensity of the fluorophores. SMACKM [83] is also an

acronym given to the whole technique which stands for single-molecule active control microscopy.

Detection of a single molecule within a dense volume of dyes was first done in 1989 by the Nobel laureate W.E. Moerner [85]. His result at the time was revolutionary not only because single molecule was detected, but because it was done by measurement of fluorescent absorption rather than emission. Measurement of emission was later done to improve the signal to noise ratio [86] by Orrit. The method was further applied to single fluorophore detection in a liquid medium at room temperature [87, 88]. To reduce the background confocal [89] and TIRF [90] were also exploited. These finding paved the road for many single molecule spectroscopic and microscopic experiments, even though it wasn't until 2006 that this technique could be applied to densely labelled biological sample. Betzig in 1995 published a paper [91] proposing the idea of SML for biological imaging. In 1997, Moerner observed a phenomenon while performing experiments on green fluorescent proteins (GFP). When the GFP molecules were excited with 488 nm laser, they produced several cycles of intermittent fluorescent emission. And after a few cycles of blinking they went to an steady state off. However, the proteins could be re-excited and brought back to on state upon illumination with 405nm laser [92].

The principle of GFP photo-switching is shown in Figure 1-15. GFP in state A can undergo a radiative transition to A* and relaxation afterwards. While it is excited in A, process P1 may populated state I which is non-fluorescent. Now, spontaneous transition from I to A* makes blinking occur. At the same time process P2 populates another dark state N – which caused the stable dark state. Here excitation with 405 nm

laser causes populating N* and by process P3 returning to A and A* states, which is essentially re-generating fluorescence.

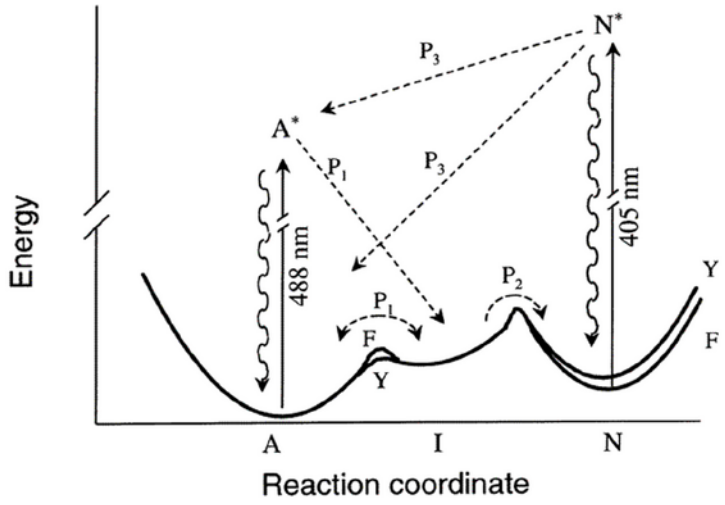

Figure 1-15 – Energy states of Green Fluorescent Protein. Adapted from [92].

In 2002 the first Photo-switchable GFP variant was engineered [93]. It was designed such that by illumination of 413 nm light it could be activated. And excitation with 488 nm light leads to fluorescence. Intense illumination at 488nm would however make it irreversibly photo-bleached. This process was used by Betzig [15] in 2006 and later by Hess [16] to be the first of its kind on a densely labelled biological sample.

The same principle but by using a pair of organic dyes in close proximity of each other, such that resonant energy transfer, was used by Zhuang [17]. STORM method was improved in 2008 by Sauer and colleagues, and they called their method direct STORM or dSTORM [18]. In this method in contrast to tandem dyes of STORM, only single organic dyes are used. The dye is excited to the first single mode, but after the excitation some part of the fluorophores relax to the first Triplet state. From the triplet state by some photo-chemistry that will be explained in the next chapter, it can return to the singlet state

and emit photons again. Yet the inter-system crossing that occurs is a forbidden transition with relaxation time 3 orders of magnitude larger that singlet state relaxation. This difference helps having only a small fraction of dyes in fluorescing at a single time.

SML methods have been applied to multi-color [94, 95], whole cell and 3D [96-100], and interferometric [101] and live [102] imaging. Sample images of STORM are shown in Figure 1-16.

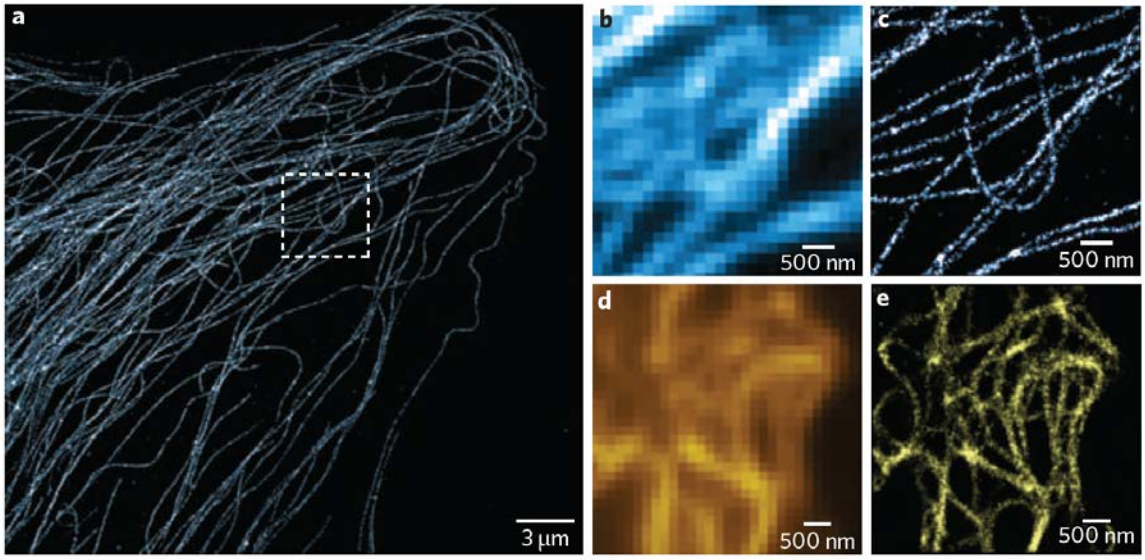

Figure 1-16 – Examples of STORM imaging of cells with photo-switchable dyes and fluorescent proteins. An STORM image of Microtubules in a BS-C-1 cell stained with photo-switchable Alexa Fluor 647 is shown in (a). The zoomed widefield and STORM images of boxed region are shown in (b,c) respectively. In (d,e) widefield and STORM images of vimentin filaments of a BS-C-1 cell -- labelled with a photo-switchable fluorescent protein mEos2 -- are shown. Adapted from [103].

The resolution of SML is a function of several factors such as standard deviation of PSF s, the number of collected photons N, pixel size a, and background noise b [104], most importantly s and N:

$$\Delta_{x,y} = \sqrt{\frac{s^2 + \frac{a^2}{12}}{N} + \frac{8\pi s^4 b^2}{a^2 N^2}} \approx \frac{s}{\sqrt{N}} \tag{1.7}$$

Given s and N are the most important parameters of the technique's resolution, two main approaches can be taken for enhancement. Adaptive Optics (AO) can be used to improve s. We will discuss it in the next section. The other approach is to improve the photon emission efficiency. Photo-chemistry has been addressed by many scientist to produce buffers that help generation of more photon, as well as facilitation of inter-system crossing [105, 106]. Another way to use Quantum Dots (QD) which naturally emit more photons than organic dyes [107, 108].

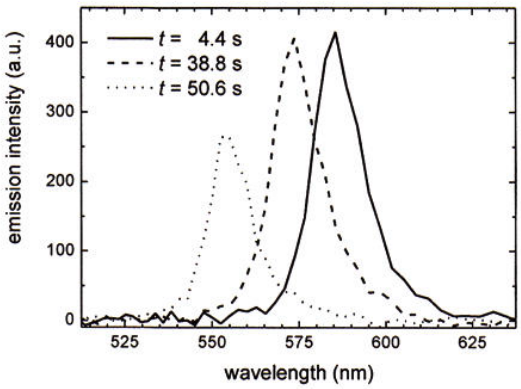

Figure 1-17 - Blueing phenomenon. Upon irradiation on the Quantum Dots their wavelength shifts toward blue. Adapted from [109]

QDs have many advantages over organic dyes such as wide absorption spectrum, narrow emission, and more importantly their size-dependent wavelength [110]. Although QDs have been used with the same concept of blinking as in dSTORM [111], their higher fluorescence cross section, causes higher duty cycle (ratio of on to off state) which is not desirable as it increases the probability of having more than one dye in on state in a PSF volume at a single time. Therefore Hell in 2010 used a phenomenon called QD blueing that was explained in 2001 [109] to overcome this problem. Blueing phenomenon takes advantage of the size dependent wavelength of QD and size reduction due to photo-oxidation to blue shift their emission spectrum. This idea can be employed for SML, by

using a narrow-band-pass filter on the spectral path of the QD towards blue, to individualize a fraction of QDs at a time, due to their Asynchronous blueing [108]. We will present implementation of two color blueing in chapter 3.

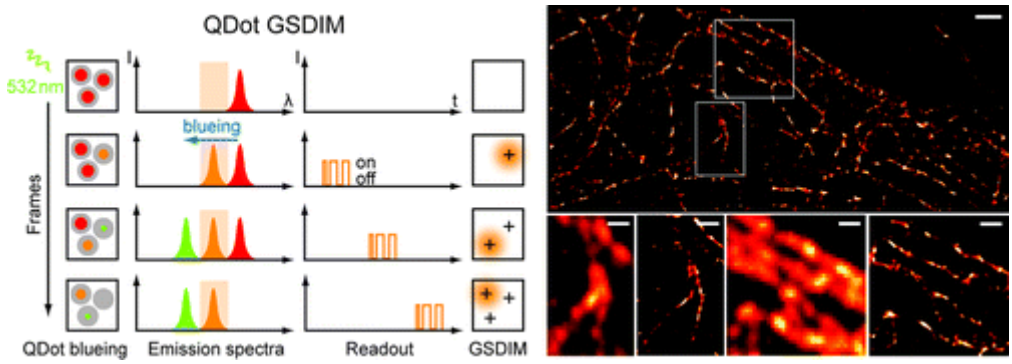

Figure 1-18 – Exploiting Blueing phenomenon for SML imaging. Left panel shows the place of the narrow band pass filter relative to the spectral path of QD toward blue. The right panel shows an example of super-resolution achieved by this technique. Adapted from [108].

1.3. Adaptive Optics (AO)

In this section we discuss the effects of distortions to imaging and ways to compensate for them. This field was first explored by astronomers in 1940's and 50's [112-114]. Performance of ground-based telescope without correcting elements has been limited by the turbulence in the Earth's atmosphere due to wind and rapid changes in refractive index of the atmosphere [115]. The field perturbation after passing through layers of turbulence induced aberration can be modelled by

$$u\left(\vec{x}\right) = W\left(\vec{x}\right)\exp\left(\chi\left(\vec{x}\right) + j\psi\left(\vec{x}\right)\right) \tag{1.8}$$

where $W(\vec{x})$ is the telescope aperture function, $\chi(\vec{x})$ accounts for the logarithm of amplitude fluctuations, and $\psi\left(\vec{x}\right)$ accounts for fluctuations in the phase of the wave. The equation shows how phase variations can exponentially distort the field. There are harsh

claims that resolution of the two 10m Keck telescopes in Hawaii could not be better than an 8 inch backyard telescope without AO. Turbulence spreads out the light from a star, making it twinkle and appears as a fuzzy blob when viewed through a telescope. An example is shown in Figure 1-19.

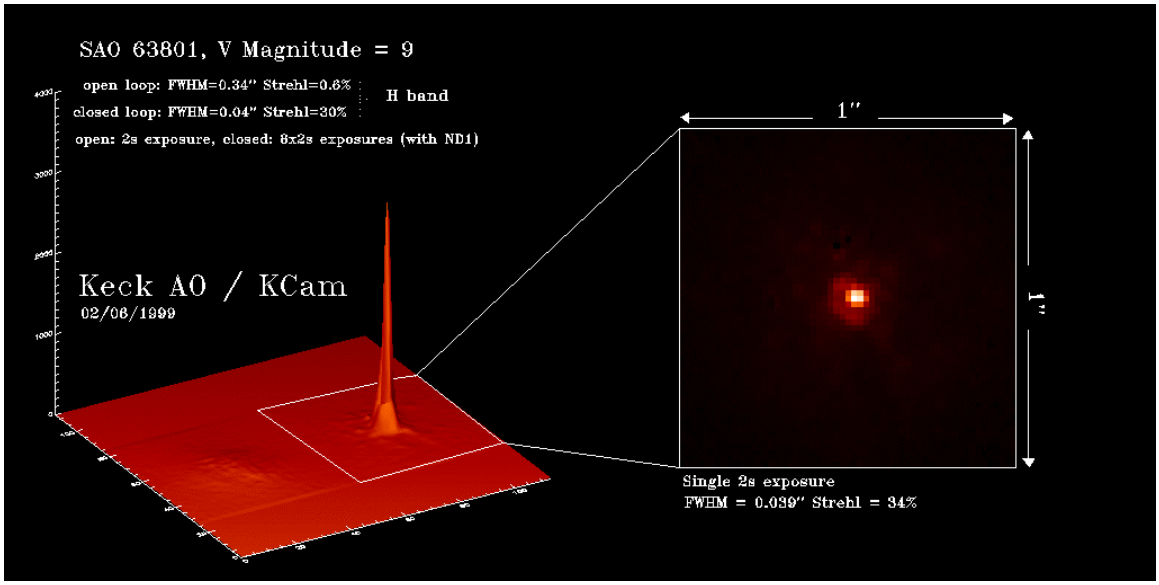

Figure 1-19 - Image of a star with and without correction. Credit University of California Santa Cruz Center for Adaptive Optics.

Babcock was one of the first to suggest implementation of a correcting element for turbulences caused by atmosphere [114]. At the time simple mechanisms were suggested and applied to correct lateral movement of stars (tip/tilt), such as photo-electric guiding [112], and rotating knife-edge [113]. But it wasn't until late 1960's and early 1970's that Wavefront shaping by Deformable Mirror (DM) was practically realized first for military applications and then applied to astronomy [116]. In 1990's AO was an established technology in astronomy. An example is the images shown in Figure 1-20 by ground-based Keck telescope. We can see that AO correction revealed more information than it could conventionally be measured. There are many scientists and research groups

working on improvement of the accuracy and speed of Wavefront sensing, reconstruction, and algorithms to predict and optimize the Wavefront more efficiently.

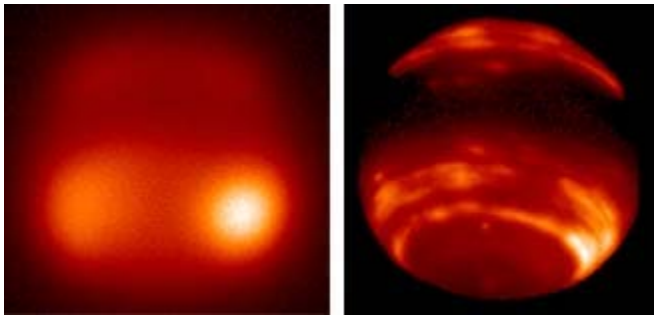

Figure 1-20 - Image of Neptune by Keck observatory without (left) and with (right) AO. Images were taken at different dates and times. Credit University of California Santa Cruz Center for Adaptive Optics.

The problem of optical aberrations also occurs in Microscopy. This time not from the travelling channel (slightly) but (principally) from the object under the study. The biological tissues are made of many layers varying refractive indices, and non-geometrical shapes that causes light to be refracted in predictable and unpredictable patterns [117]. Predictable aberrations are the ones that have been modelled mathematically, such as Zernike polynomials [118]. The main aberrations of such are Defocus, Astigmatism, Coma, and Spherical which correspond to lower order Zernike modes. There has been works on compensation of unpredictable aberrations (scattering media) that can be applied to biological imaging [119].

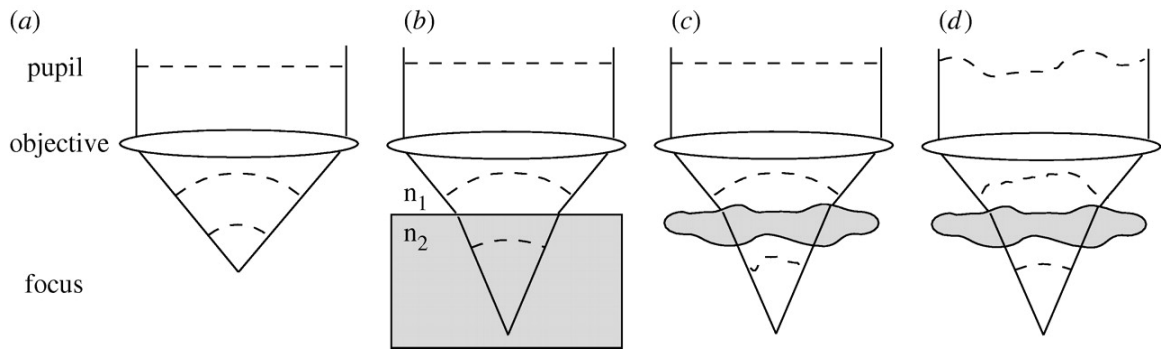

Figure 1-21 – Effects of aberration on imaging using high NA objective. (a) shows an ideal system where a planar Wavefront is converted to convergent spherical wavefront. In (b) effects of spherical aberration can be seen where the refractive index mismatch causes change in the shape of wavefront. (c) shows effect of a complex shaped object to the Wavefront. And in (d) the AO system has produced such wavefront that by passing through the object it will have a corrected convergent Wavefront at the focal plane. Adapted from [120].

(a) Schematic of focusing by a high-NA objective lens. Planar wavefronts in the pupil are converted into convergent spherical wavefronts in the focus. (b) The effects of focusing through a refractive index mismatch, where refraction at the interface d

Initially AO for microscopy was aimed to correct spherical aberrations caused by high NA objective lenses [121]. Oil immersion lenses produce a refractive index mismatch at the boundary of oil and the biological sample with refractive index close to water. It causes expansion of focal plane and ultimately curving the Wavefront. This problem worsens as the focal plane penetrates into the sample, as shown in Figure 1-21. Scientists have shown that even at depth of about 90 µm there are substantial amount of aberrations that distort PSF laterally and elongate it axially [122, 123].

The first implementation of AO in microscopy was on confocal microscopy in 1999. Since the confocal configuration used was not in epi mode (same path for illumination and imaging), by scanning deep inside a tissue, the nominal focal plane (NFP) may not match the actual focal plane [117]. It has to be noted that in the epi mode tip and tilt are auto-correcting. Later AO was applied to confocal for correcting the main aberrations [124]. Since then, AO has been applied to wide-field [125, 126], two-photon

[127, 128], STED [129], light sheet, SIM [130], and SML microscopy [131-134]. AO has also been used for enhancement of microscopy, such as improving the depth of field [135], and providing Astigmatism to 3D SML imaging [131].

1.4. Outline

In chapter 2 we will present SML theoretically and experimentally. Fluorescent techniques employed for this techniques as well as chemical buffers that induce blinking, will be discussed. Multi-color SML imaging will be shown. Methods to expand SML to 3 dimensions will be discussed. And experimental examples of each method will be shown.

In Chapter 3, the application of Quantum Dots (QD) for SML imaging is presented. First the molecular transitions, structure, and photo-stability of QDs are discussed and compared with other dyes. Then the Blueing method for localizing QDs is presented. It is followed by a discussion of the resolution of this method, the effect of mounting media on blueing, and finally our novel two-color QD blueing imaging method. A discussion of cross-talk between channels, correction of chromatic aberration, and 3D imaging follows.

Chapter 4 is about Adaptive Optics methods. Modelling of aberrations induced by the instrument and biological samples is discussed. A discussion of direct and indirect wavefront sensing follows. Then correction methods and algorithms are shown.

In chapter 5 we demonstrate our implementation of machine learning algorithms for Wavefront sensor-less AO correction of SML imaging. The Genetic Algorithm (GA) and Particle Swarm Optimization (PSO) are introduced. We further introduce an Intensity-independent metric for the estimation of the image quality. Simulations of both

algorithms are shown followed by their implementation on thin and thick biological samples.

Finally chapter 6 is the discussion and conclusion of this dissertation.

2. SINGLE MOLECULE LOCALIZATION MICROSCOPY

Fluorescence microscopy has many advantages over label-free imaging methods, such as specificity of biological organelle, and ability to implement super-resolution methods such as STED, SSIM, and SML. In this chapter we will focus on the theory behind SML. Some experimental results are also presented to illustrate the concepts.

We mentioned in chapter 1 that light microscopy is limited by effects of diffraction. In other words when two particles are placed very close to each other, the limited-bandwidth light microscopy image cannot distinguish them. The spatial band-width of the optical system plays a key role here. In a linear system, when an impulse (containing all frequencies) is inserted into the input of the system, the output reveals the system frequency response. An optical system is in fact a linear system. Therefore by imaging a tiny particle (sub-diffraction limit < ~200nm) the spatial frequency response of the system can be measured. A limited-bandwidth or diffraction limited system causes the image of the tiny particle to be larger than the particle itself. An image of a Yellow-Green (YG) fluorescent bead is shown in Figure 2-1(a), the red dot shows the actual size of the bead. Therefore two particles that are closer than the diffraction limit are not resolvable, as shown in Figure 2-1(b). The minimum distance resolvable in a light microscope is λ/NA (Abbe [8] or $0.61\lambda/NA$ Rayleigh criterion [22]). In a modern light microscope, the NA can be as high as 1.4 so that the minimum resolvable distance is about 200nm.

In SML microscopy, resolution beyond the diffraction-limit is achieved by imaging individual fluorophores in an ensemble, separately. Because we are dealing with overlapping PSFs of very small molecules (much smaller than the diffraction limit); using photoswitching characteristics of fluorescent molecules, “blinking” can be induced in several ways. At the right rate of blinking we would be able to image only one fluorescing dye in any PSF area. This helps us isolate the molecule from their assembly. By imaging single molecules, their centers of emission can be calculated and tabulated. We can therefore plot the measured centers together in a high resolution reconstructed image [15-18]. Figure 2-1(c) shows the process of SML; the diffraction limited wide-field image on top is super-resolved to the bottom image by capturing a couple of thousand images, where only a fraction of fluorophores are emitting photons in each frame. In this example 15,000 frames were imaged at 50 frames per second (fps). The sample is a hepG2 cell with its microtubules stained with 565nm QD. A part on the wide-field image is compared with its super-resolved version in Figure 2-1(d) and (e) respectively. Many details which were not visible in the wide-field image are revealed.

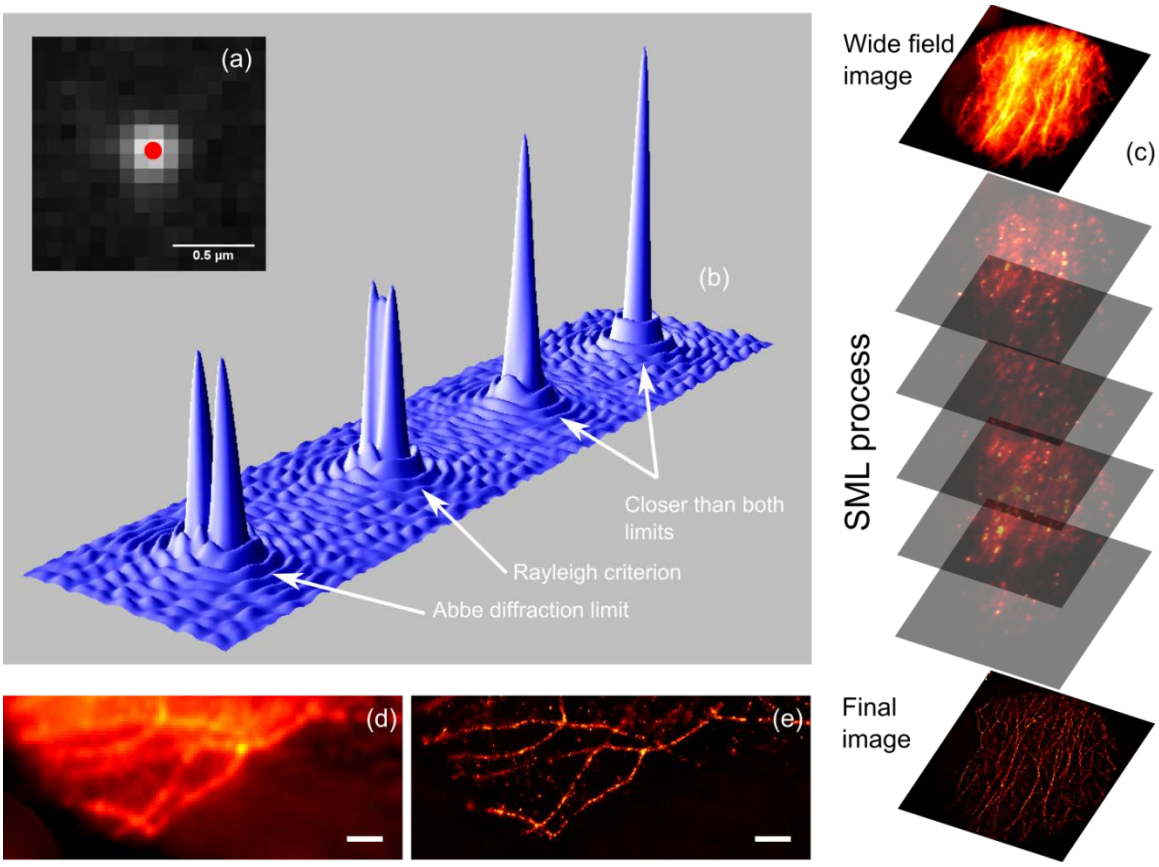

Figure 2-1 - Effect of diffraction limit on (a) a yellow-green fluorescent bead with 100nm radius – the red dot shows the actual size of the dot – and (b) two adjacent particle getting close to each other. (c) shows the process of SML to go from the wide-field image on top to the super-resolved image at the bottom. 15,000 frames were imaged at 50 fps. The sample is microtubules of a hepG2 cell stained with 565nm Quantum Dot. (d) and (e) are corresponding parts of a wide-field and a SML image. Many details that are not visible in conventional widefield image appear in the super-resolved image. Scale bars are 1µm.

Before we go into theory of the technique we will talk about the methods of binding fluorescent molecules to the specific organelle under study. Then we discuss the mechanism of blinking fluorescence for each strategy of SML. Nyquist sampling theorem and effect of blinking rate on resolution are explained afterwards. It is followed by accuracy of detection, and image reconstruction methods. And finally practical implementations of SML for multi-color, and 3-dimensional imaging are discussed.

2.1. Staining methods

As we discussed in section 1.2.2, Fluorescence Microscopy takes advantage of the Stokes shift between the absorption and emission spectra of the fluorescent molecules. Fluorescent molecules attached to specific structures inside a cell or tissue absorb light at one wavelength and generally emit at another wavelength slightly longer. There are many ways of adhering fluorescent molecules to cellular structures in studies of cells (cytology) and tissues (histology). Many Fluorescent dyes have been engineered to bind to specific organelles (e.g. the endoplasmic reticulum, golgi apparatus, endosomes, lysosomes, nucleus, plasma membrane, mitochondria, peroxisome and centromeres) [136]. DAPI [137] is an example of fluorescent stain that attaches to A-T rich regions of nucleic acids and is therefore suitable for visualizing the nucleus of cells. Another example is the binding of dyes using phallotoxins to actin filaments (F-actin) [138], which is a more efficient way than using anti-actin antibodies. In Figure 2-2 (a) staining of Hela cells' Actin filaments and nuclei are shown with phalloidin Alexa647 conjugate and DAPI respectively.

Another very commonly used method of fluorescent staining is immunofluorescence, which uses immunology antibodies to locate the desired proteins. Antibodies interact and bind to either antigens, directly to proteins or, to a target antibody. The technique has two sub categories based on the class of antibody used; direct and indirect binding. In direct binding the antibody is linked to the fluorophore, and binds to a specific region called the epitope. In indirect immunofluorescence, two antibodies are used. A primary antibody is used that binds to the cellular structure; and a secondary antibody that carries the fluorophore and attaches to the primary anti body.

Since more than one secondary antibody can attach to one primary, this method can help with signal amplification.

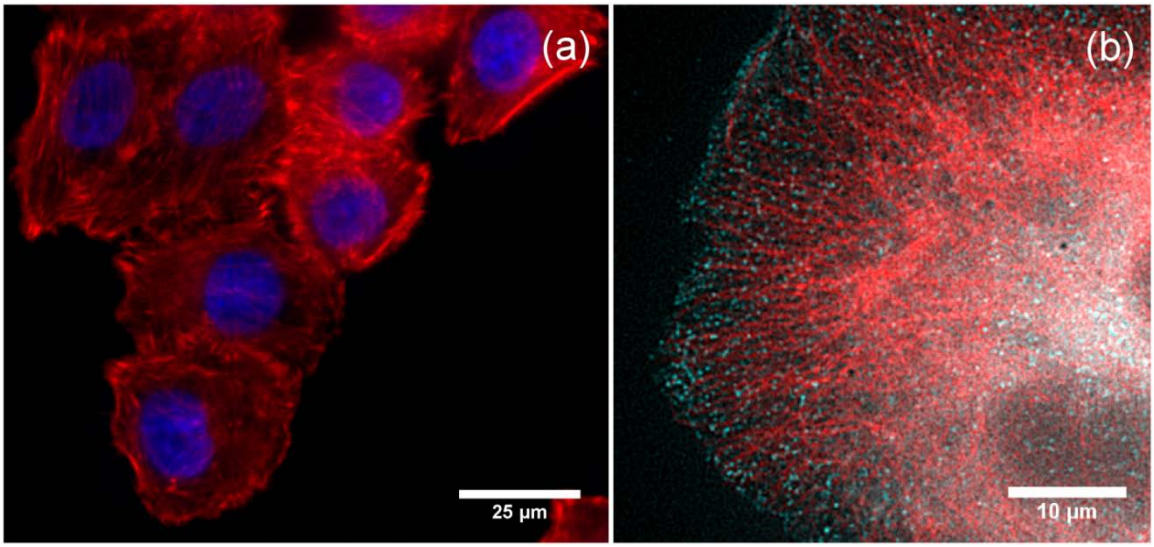

Figure 2-2 - Examples of fluorescent staining. In (a) actin fillaments of Hela cells are stained with Alexa647 dye (red) using Phalloidin. They are co-stained with DAPI which shows their nuclei (blue). (b) shows microtubules and clatherin coated pits of a Hela cell stained with Alexa647 and Alexa488 respectively.

Fluorescent proteins (FPs) are another extremely powerful tool for labeling of specific proteins. FP tagging can be used to detect proteins that are very difficult to isolate. It can also be used to distinguish between two proteins with similar antigenicity [136]. The expression of the FP in the sample can be done through Transduction [139], Transfection [140], or transformation [141]. An example of Fluorescent Protein expression is shown in Figure 2-3. Neuro-peptide F (NPF)-Gal4 neurons - expressed with Red Fluorescent Protein (RFP) – are in synaptic connection with Tdc2-Gal4 - expressed by GFP.

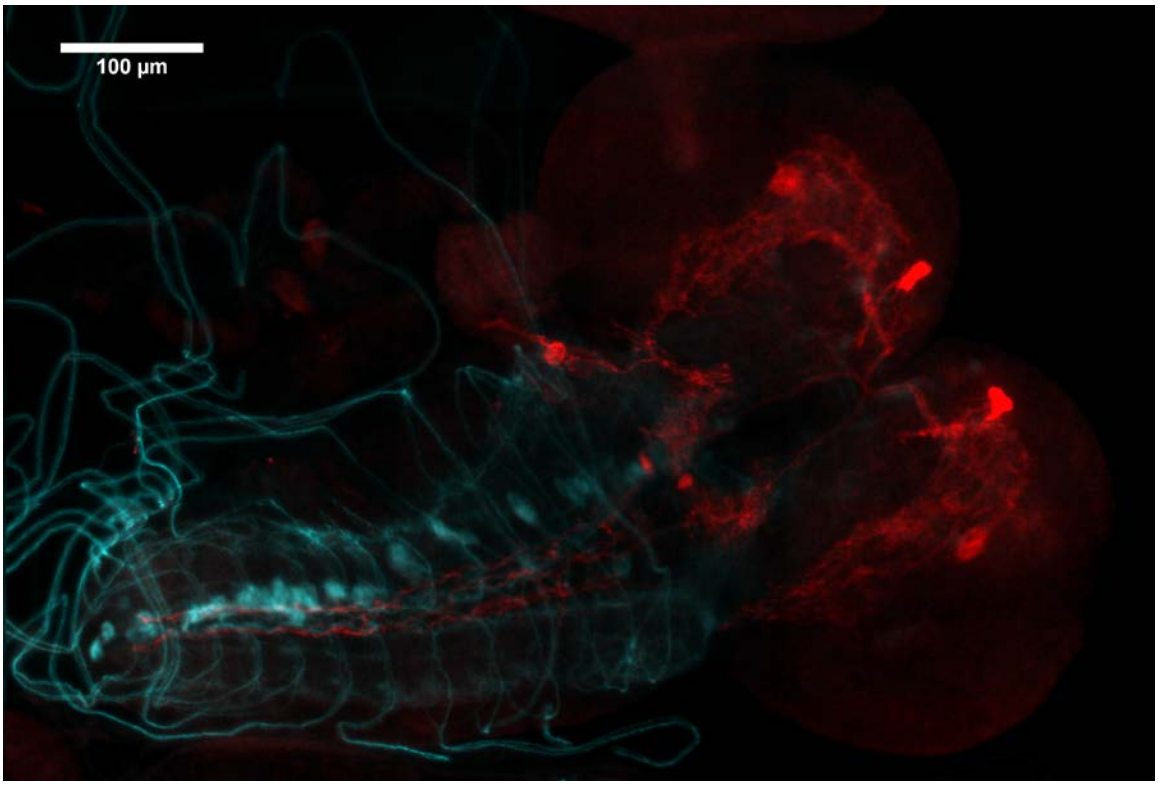

Figure 2-3 - Expression of Green and Red fluorescent proteins in Central Nervous system of Drosophila larvae. Neuro-peptide F (NPF)-Gal4 neurons - expressed with Red Fluorescent Protein (RFP) – are in synaptic connection with Tdc2-Gal4 - expressed by GFP.

2.2. Mechanism of Fluorescence

In this section we talk about how to make fluorophores blink. An ideal fluorescent molecule for SML, should have a non-radiative lifetime much longer than its fluorescent life time. Lower rate of blinking or duty cycle improves the resolving power of SML (we will discuss this in section 2.3). The very first paper [15] that was published on SML (PALM method) uses photo-activable fluorescent proteins to induce blinking and individualize fluorophores from their ensemble. Later STORM method used a pair of dyes that can be switched on and off using Förster resonance energy transfer. QDs are other fluorescing particles that have been used for SML. They are of special interest to us

due to their high photon yield which can increase the resolution of SML Microscopy. QD blueing method however will be discussed in more details in the next chapter. This section will continue by discussing principle of blinking of a conventional organic dye.

2.2.1. Stokes shift

A two-level Jablonski diagram of the energy state of a typical fluorophore is shown in Figure 2-10 (a). The fluorophores have several vibrational levels at each of their electronic energy levels. Figure 2-6 (a) depicts singlet ground and first singlet levels as S0 and S1, of two fluorophores. For fluorescence to occur from a single fluorophore; once external energy is applied –excitation light here- some electrons move from their orbital with the same spin as in the ground state to a possible excited state. At this point the electrons can relax to the lowest vibrational level by 'internal conversion' in a time scale of 10^{-12} seconds. The relaxation from the lowest vibrational level to the ground state would cause some stimulated and some spontaneous emission of photons, as well as some non-radiative decay, quenching and thermal loss [142]. We know that energy of a photon is determined by $E = hc/\lambda$, therefore due to the energy difference between the excitation energy and the emission energy; the wavelength of the emission is red-shifted. This is known as 'Stokes shift'.

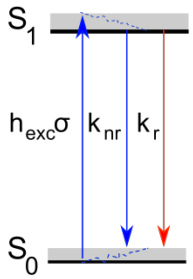

Figure 2-4 – Two level fluorescence energy diagram.

2.2.2. Fluorescent proteins – PALM/fPALM

Photon emission dynamics from fluorescent proteins (FP) are complex. They have several radiative and non-radiative states which result in blinking [16, 92, 93, 143-148]. The blinking mechanism is different among various mutant of FPs. Some are switching between a dark state and an emitting state, while some others shift wavelength from one emitting state to a lower energy state with a correspondingly longer emission wavelength. FPs can generally be placed in three categories; Irreversible photo-activable (PA) FPs (e.g. PA-GFP [93, 149, 150] and PA-RFP1-1 [149, 151, 152] with molar extinction coefficients of 17,400 and 10,000 respectively), photo-shiftable (PS) FP such as Kaede (60,400 molar absorption coefficient and ~400 emission photons) [153], KiKGR (32,600 molar absorption coefficient) [154] and Monomeric Eos (37,000 molar absorption coefficient and ~490 emission photons) [155], and finally reversible photo-activable FPs such as Dronpa (95,000 molar absorption coefficient and 120 emission photons) [145]. The reversible PA FPs works on a similar principle to PS-FPs, in that, instead of switching to another fluorescing state, they go to a dark state.

The energy states and dynamics of a typical FP is drawn in Figure 2-5. Although at room temperature the mechanism of emission in FPs is very complex; nonetheless scientists have characterized absorption and emission spectra of several FPs at cryo temperatures (1.6 K) [143], to remove the effects of thermally induced conversions. In cryo temperatures the spectrum becomes more structured. Figure 2-4 illustrates the general principal of photoswitching in FPs.

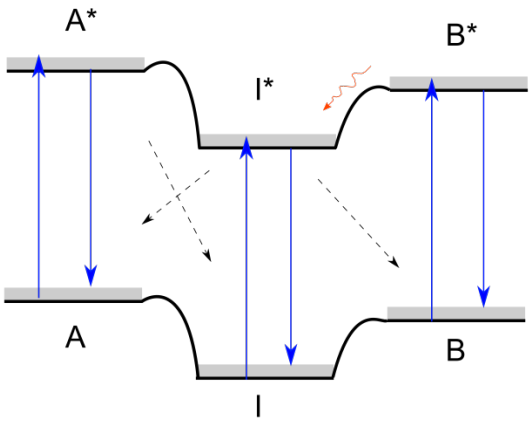

Figure 2-5 – Energy-level diagram of a Photo-activable Green Fluorescent Protein. A, I, B are different states of the protein, radiative, intermediate, and non-radiative respectively.

Based on the model from [16, 156], there are three general states, a bright state A, an intermediate dark state I, and a bleached state B. At first, we can assume the molecule is in the ground state, A. The molecule can be activated by absorbing a photon,to exciting state A*, with activation excitation rate k_A, spontaneous excitation rate k_0, and activation quantum yield ϕ_A. At this point, due to thermal activation and other spontaneous energy transitions, some electron can move from A* to I* with rate $k_{BC,}$ while the rest relax to A and emit photons. This move back and forth from state A to state I, causes the desired blinking. Although up to this point this process seems ideal for induction of blinking to molecules, nevertheless after some cycles between active and inactive states, the molecules perform another transition to a permanent dark state known as the "bleached" state, with a rate and quantum yield of k_x and ϕ_B. After this point the FP cannot be recovered. This process is formulated by three coupled linear ordinary differential equations (ODE), where each letter represent the number of electrons in their corresponding state [16] and $A + I + B = constant$:

$$\begin{cases} \dfrac{\partial I}{dt} = -I(k_A \Phi_A + k_0) + k_{BC} A \\ \dfrac{\partial A}{dt} = -A k_x \Phi_B + I(k_A \Phi_A + k_0) - k_{BC} A \\ \dfrac{\partial B}{dt} = A k_x \Phi_B \end{cases} \quad (2.1)$$

To make sure that the FP has low duty cycle so that the PSFs do not overlap, we require $k_{BC} \gg k_A \Phi_A$. While FPs show some of the desired characteristics of a dye for SML imaging, their low photon emission, or high duty cycle in some species, made researchers to look for other solutions to the problem of blinking. In the next section use of resonant energy transfer for making an optical switch is presented.

2.2.3. FRET – STORM

To use many advantages of cyanine or xanthene based organic dyes – such as higher photon emission, and lower duty cycle- for SML, first a photo-switching mechanism had to be developed. Scientist employed the concept of Fluorescent (or Förster) Resonant Energy Transfer (FRET) to activate and deactivate what they called an optical switch [157-159]. FRET is the process with which a fluorophore excited to S_1 relaxes by transferring its energy to another fluorophore in close proximity (1-10nm) non-radiatively [160].

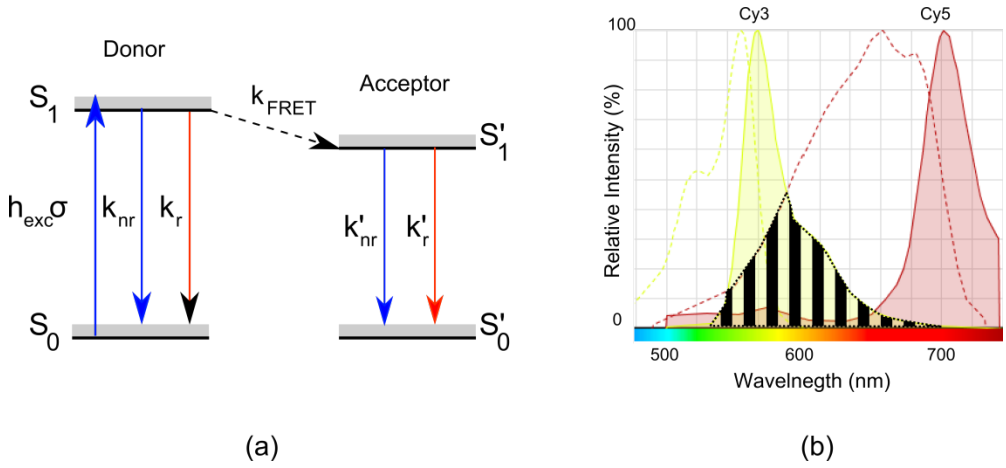

Figure 2-6 - Energy level diagram of two fluorescent molecule in close proximity of each other (1-10 nm) is shown in (a). In (b) we can see the excitation and emission spectra of Cy3 and Cy5 fluorophores. R_0 depends on the amount of overlap between the Donor's emission and the acceptor's excitation spectra.

In FRET the energy from S_1 resonantly transfers to the close by fluorophore, pulling it to their excited state S'_1. The energy transfer occurs at a rate determined by k_{FRET}

$$k_{FRET} = \frac{1}{\tau_e}\left(\frac{R_0}{R}\right)^6 \tag{2.2}$$

where τ_e is the decay rate, R is the distance between the two molecules, and R0 is the measure of overlap between the donor's emission and acceptor's excitation spectra. The overlap is depicted in Figure 2-6 (b) by the stripe pattern. At steady state the quantum efficiency of FRET can be calculated using the following equation.

$$q_{FRET} = \frac{k_{FRET}}{k_r + k_{nr} + k_{FRET}} \tag{2.3}$$

While FRET has been used in studies of conformational bio-molecule interactions [161-164]; its implementation as an optical switch [157-159] laid the ground work for SML imaging using organic dyes. The Zhuang group tested an optical switch made of a

Cy3 donor, and a Cy5 acceptor dye attached to each other using opposite strands of a double stranded DNA. They showed that by exciting both the donor and the acceptor at the same time. the photo-switch can be activated. Emitted light is therefore from direct excitation of the acceptor, and not FRET. Now by only exciting the acceptor while the donor is relaxed, it will go to a non-bleached non-radiative state. The photo-switch can therefore be reverted by simulation excitation of both dyes. This photo-switching effect was later used to perform SML imaging [17]. They coined the method STORM. This method has been extended to multi-color [94], whole-cell [96], and neuro imaging [95]. However it requires non-trivial process of producing the tandem dyes, which made some other scientists to come up with another method to make conventional dyes blink; direct STORM.

2.2.4. Electronic transitions and dark state transitions – dSTORM

Organic dyes such as carbocyanine dyes, or the family of Alexa dyes have the advantage of emitting more photons than other types of dyes [165]. In this section we discuss the theory of blinking for organic dyes. This method was suggested [166] and first used for SML as an alternative to complex tandem dyes of STORM, hence called direct STORM [18] (dSTORM).

The diagram of two-level fluorescence we showed in Figure 2-4 does not express quenching of the singlet excited state to the first triplet state. As we mentioned earlier, in singlet excitation one electron from a ground state orbital (two electrons exist in one orbital with opposite spin) would move to higher energy level upon excitation with the same spin. To excite (or quench to) Triplet state, the electron must undergo a splin-flip, giving it the same spin as the other electron in its ground state orbital. This results in a

"forbidden" transition to the ground state, therefore the transition takes at least 3 orders of magnitude longer to occur. This process is called inter-system crossing, inferring that the electron in its new spin is in a new different state. As shown in Figure 2-7 the rate at which the electrons travel between S_1 and T_1 is k_{isc}. If a radiative relaxation from the Triplet excited to Triplet ground state happens it would be phosphorescence which is not subject of our study. Effects of radical anionic and cationic cis-trans isomerization on blinking have also been also studied in the literature [167-169].

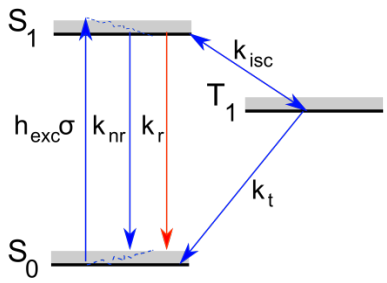

Figure 2-7 – Three level Energy diagram of a typical organic dye.

The two-level system can be modelled by the following first order ODE [21, 142]

$$\frac{\partial n_0}{dt} = -\frac{\partial n_1}{dt} = -h_{exc}\sigma n_0 + (k_r + k_{nr})n_1 \tag{2.4}$$

where n_0 and n_1 represent population of electrons in S_0 and S_1 respectively. k_r is the radiative relaxation and k_{nr} is the non-radiative decay. The molecule is excited by $h_{exc}\sigma$. At steady state the quantum efficiency of the molecule can be given by:

$$q = \frac{k_r}{k_r + k_{nr}} \tag{2.5}$$

For the three-level system, another term has to be added to the equation of the population of S_1, accounting for the quenching by a transition to T_1 with rate k_{isc}. In the following set of coupled ODEs, the relations between all levels are modelled [21, 142]

$$\begin{cases} \frac{\partial n_0}{dt} = -h_{exc}\sigma n_0 + (k_r + k_{nr})n_1 + k_t n_2 \\ \frac{\partial n_1}{dt} = h_{exc}\sigma n_0 - (k_r + k_{nr} + k_{isc})n_1 \\ \frac{\partial n_2}{dt} = k_{isc} n_1 + k_t n_2 \end{cases} \tag{2.6}$$

where n_2 is the population of T_1, and k_t is non-radiative decay rate of T_1. It has to be noted that since a certain number of electrons have entered the system, the sum of all populations stays constant, $n_0 + n_1 + n_2 = cnst$. The radiative quantum efficiency is given by:

$$q = \frac{k_r}{k_r + k_{nr} + k_{isc}} \tag{2.7}$$

Since the triplet state is essentially a dark state, and we are only collecting light from the singlet excited state, we can find the rate at which the molecule would blink, by finding the ratio of populations of n_1 to $n_0 + n_2$ at steady state.

$$R_{\max} = \frac{k_r}{2 + \frac{k_{isc}}{k_t}} \tag{2.8}$$

Because we require only one molecule to be in bright state in any PSF volume; using this equation and Nyquist criterion we can calculate an upper bound on the resolution determined by Rmax, as will be shown in later sections. Since the rate of blinking has a direct effect on the resolution, several methods have been suggested in the

literature to improve it [105, 106, 170]. Discussion of mounting media is followed in section 2.4. An example of dSTORM SML imaging on microtubules of a hepG2 cell is shown in Figure 2-8. The Full Width at Half Maximum (FWHM) of a microtubule in Figure 2-8(b,c), we measured was 37 nm. Figure 2-9 shows dSTORM SML imaging of mitochondria in hepG2 cells stained with Alexa Fluor 488.

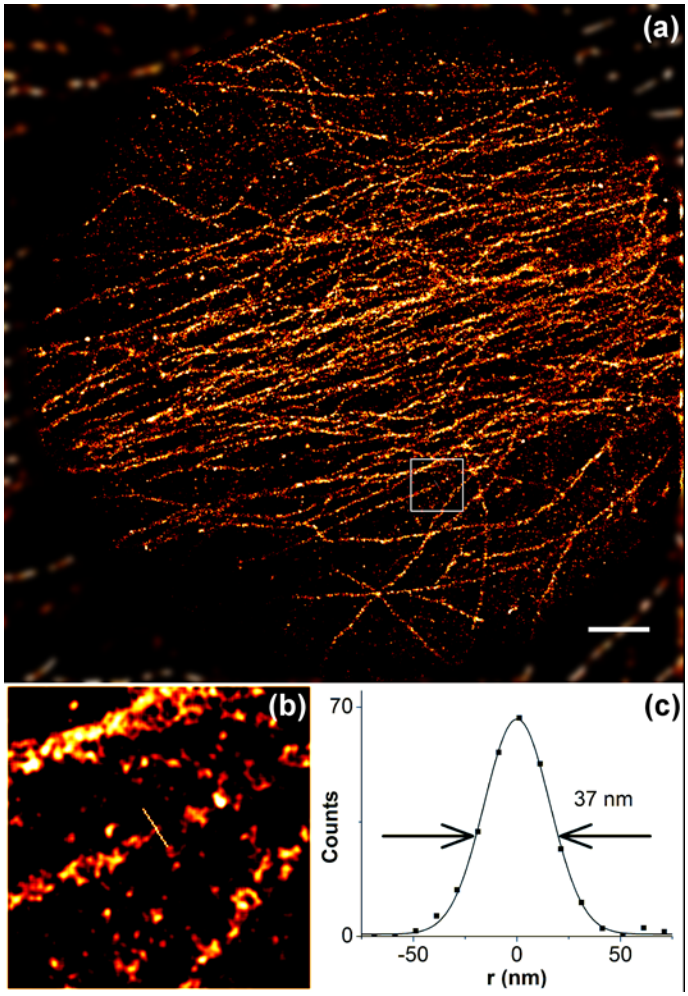

Figure 2-8 - SML imaging of microtubules of hepG2 cell stained with Alexa fluor 647 dye. The full field of view is shown in (a). A zoomed in section and the profile of a microtubule are shown respectively in (b) and (c). Scale bar is 2 µm.

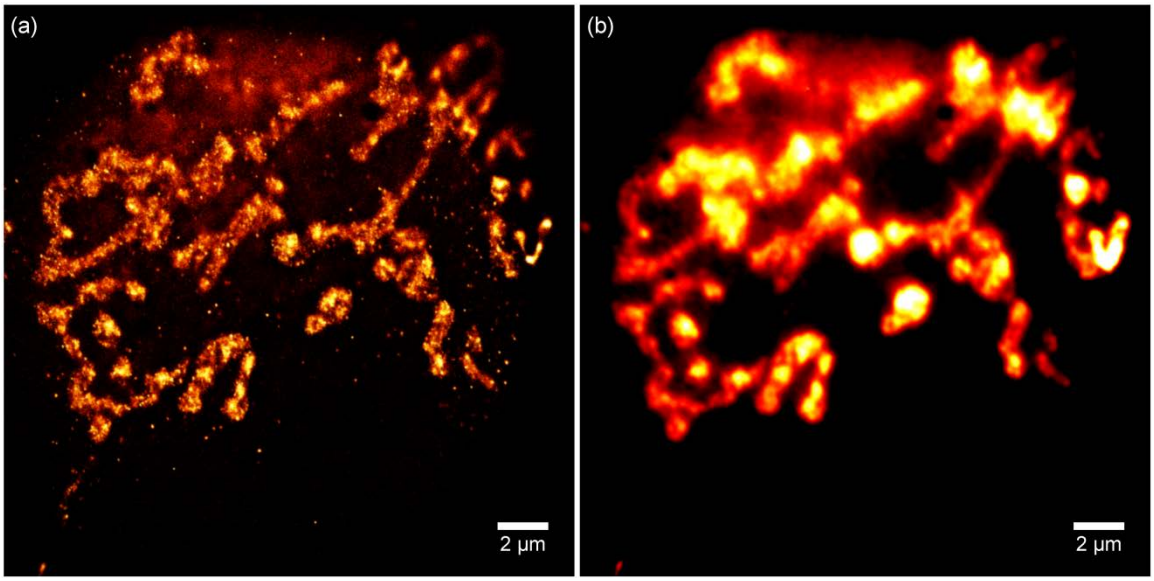

Figure 2-9 - Mitochondria in HepG2. labeled with Alexa488. (a) STORM image. (b) Widefield image.

2.2.4. Quantum Dot

Quantum Dots (QDs) are more stable, and more resistant to photobleaching than organic fluorophores and because they also emit more photon; they show great promise for SML. In this section we introduce QDs, but their implementation in SML imaging would be followed on in chapter 3.

Quantum Dots (QD) are tiny semiconductor crystals, and, unlike organic dyes or fluorescent proteins, their excitation and emission are functions of particle size, surface chemistry; dangling bonds on the surface favor non-radiative deactivation [171]. The core of a QD is composed of semiconductors of group II-VI (CdSe, CdS, CdTe), group IV-VI (PbS, PbSe, PbTe, SnTe), and group III-V (InP). The most common QD for biological studies is CdSe [172]. Due to their several advantages over organic dyes, they have gathered a lot of attention since they were first proposed for biological imaging [173-177]. Properties such as a higher absorbance cross section (approximately an order of

magnitude higher than that of typical fluorescent dyes, e.g., ~20x10-16 cm2 for CdSe QDs [178] vs. ~1x10-16 cm2 for Kaede fluorescent protein [179]), have made them desirable for many super-resolution imaging techniques [179-181]. Due to their higher resistance to photobleaching [173], they are able to emit photons for a longer time, which is another excellent characteristic for SML imaging. Although many QDs that are made with organic methods have lower stability in aqueous solutions, Micelle encapsulation [182] has made a larger family of QDs applicable to biological imaging.

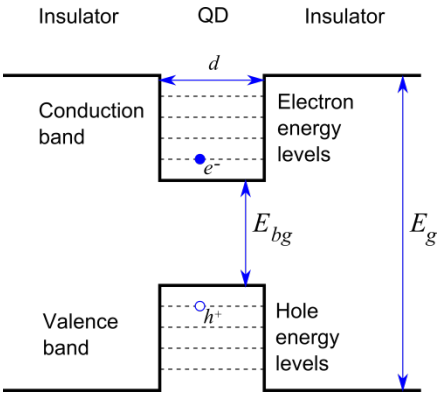

Figure 2-10 - Simple model for direct gap semiconductor.

A 1D basic energy diagram of a QD is shown in Figure 2-10. The figure shows a simplified model of a cubic QD with insulators on each side, which corresponds to core-shell structure of a QD in 3D. QD nanocrystals have unique characteristics due to their tiny size. A phenomenon that occurs in QDs is quantum confinement effect, which occurs when the size of the matter is smaller than the de Broglie wavelength, which is $\lambda_{db} = h/p$, where h is the plank's constant and p is the momentum of an electron. An electron or an electron-hole pair with discrete energy eigenvalues can be created when light is absorbed by an electron. The confinement of the wavefunctions of an electron or electron-hole in the material restricts the discrete energy eigenvalues. E_{bg} in equation 2.9, comes from

energy difference between the atomic-like occupied and unoccupied orbital. The energy gap (E_g) becomes larger than E_{bg} due to these confinement effects. The energies – shown in the second part equation 2.9 – labelled with quantum numbers are identical to kinetic energy of free particles [183]. The last term of the equation 2.9 is due to attraction of electron-hole pair. A photon that has energy greater than the band gap can excite the QD, which is the reason of wide excitation spectrum. Emission however occurs when an electron loses its energy. The energy of an excited electron in a QD is given by the following equation:

$$E_g = \frac{hc}{\lambda} = E_{bg} + \frac{h^2}{8d^2}\left(\frac{n_{e1}^2 + n_{e2}^2 + n_{e3}^2}{m_e} + \frac{n_{h1}^2 + n_{h2}^2 + n_{h3}^2}{m_h}\right) - \frac{e^2}{8r\pi\varepsilon} \qquad (2.9)$$

where n is quantum number, m is mass, d is the width of the well. As can be seen in the equation, the electron energy has a reciprocal relation with the length of QD region. In fact it can be extended to spherical shape, with QD core and insulator shell. Therefore the emitted wavelength ($\lambda_{em} = hc/E$, where c is the speed of light) of the QD is proportional to its diameter.

2.2.4.1. Blueing technique

Blinking of QDs had been observed even before they were introduced to biological imaging [184]. Blinking or fluorescence intermittency of CdSe QDs is suggested that occurs due to Auger ionization [185]. Since the natural blinking of QDs has high duty cycle techniques such as Independent Component Analysis (ICA) [111], or Super-resolution Optical Fluctuation Imaging (SOFI) [186, 187] have been developed to exploit this phenomenon and enhance spatial resolution. In the technique quantum dot

blinking with three-dimensional imaging (QDB3), 3D super-resolution imaging with blinking QDs is achieved by extracting the PSF of individual QDs by subtracting subsequent frames, again exploiting the stochastic blinking of the QDs [188]. However, their high duty cycle of blinking reduces the resolving power of SML dramatically. There has also been attempts to make photo-switchable QDs [189]. The diameter-dependent wavelength comes to rescue to this problem. Photo-oxidation of the core of the QD reduces its diameter stochastically and hence blue-shifts the wavelength. This phenomenon is called ‘blueing’ [109, 190]. By placing a narrow band-pass filter on its spectral path toward blue, a fraction of the QD can be separated from their ensemble [108]. This process is illustrated in Figure 2-11. Blueing was originally only applied to single color SML using QDs. We extended this concept to 2 colors [19, 191], which we will present more in depth in chapter 3.

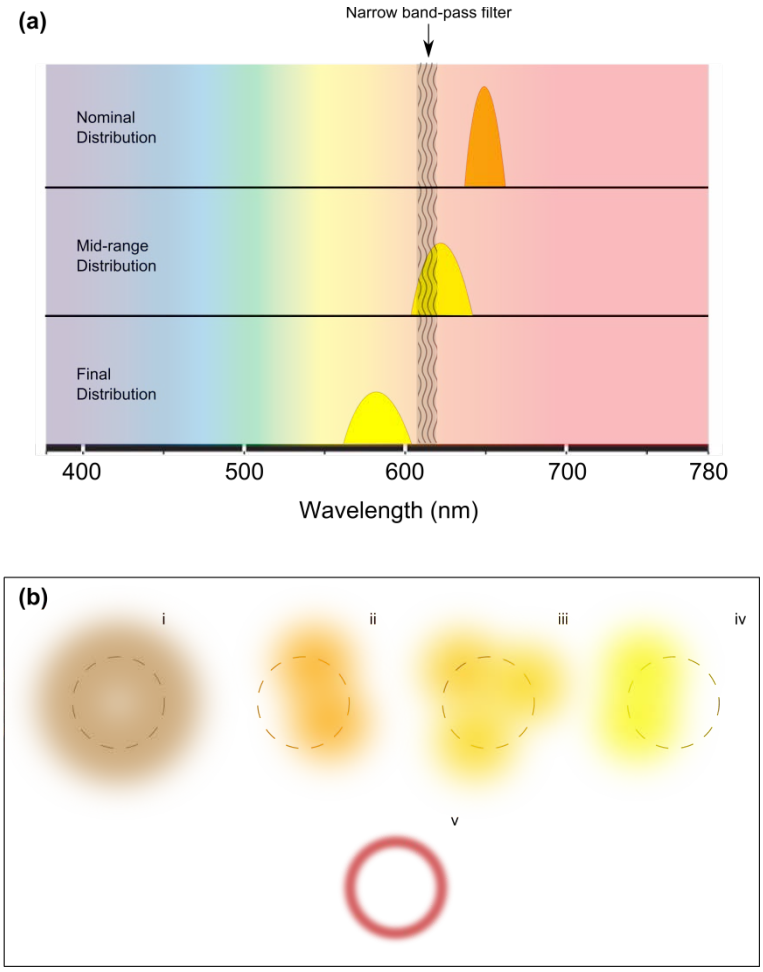

Figure 2-11 - Blueing process is shown in (a). A fraction of QDs emit photons in each sequence i-iv in (b). Using reconstruction mehods high resolution image v can be created.

2.3. The Nyquist Sampling Theorem and the rate of blinking

To be able to measure a signal, the Nyquist theorem requires that the frequency of the sampling be at least twice the highest frequency present in the signal to avoid aliasing. Aliasing means that the measurement algorithm mistakenly assumes a different frequency to a signal due to lack of enough samples. This theorem was originally applied to signals in time but can be directly applied to spatial frequencies and image processing. Therefore if we want to achieve 10 nm resolution, we need the fluorophores to label the sample every 5 nm.

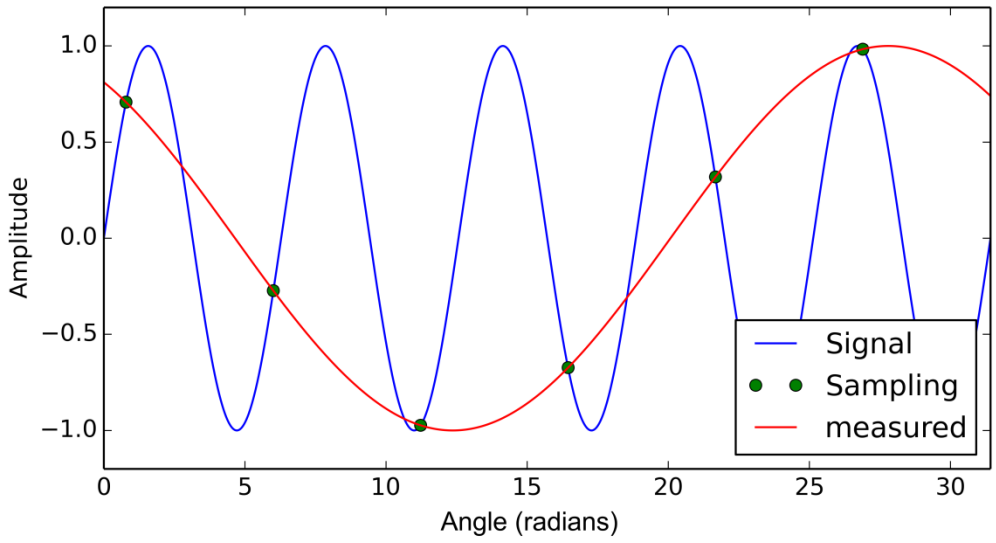

Figure 2-12 - Aliasing can cause huge errors in measurement of a signal. In this example the sampling frequency is only 1.5 times the frequency of the original signal.

We also require only one fluorophore to be emitting in a PSF area - for 2D or volume for 3D – in a given frame, in order to calculate its center of emission. The PSF area is $\sim\pi(\lambda/2NA)^2$. From the Nyquist theorem, the area per fluorophore is Δx^2 for a resolution of 2dx. Therefore the duty cycle (the ratio of on time to off time) or the rate of blinking, has to be smaller than the ratio of these two areas. We can therefore write the lower bound of resolution based on the rate of blinking in the following form:

$$\Delta x = \sqrt{\pi\left(\frac{\lambda}{2NA}\right)^2 R_{\max}} \tag{2.10}$$

Since the rate of blinking is an important issue for the resolution of SML, many chemical buffers have been developed and tested to make the dyes blink at a lower rate for a longer time [105, 106, 170, 192].

2.4. Effect of mounting media on duty cycle and photon count

Since the photo-bleaching is generally linked with photo-oxidation, to keep the molecules blinking an oxygen scavenger system [193-196] is usually used to remove the oxygen. Thiol based buffers such as mercaptoethylamine (MEA) or β-Mercaptoethanol [197] can be added to quench the triplet state. Adding Glucose Oxidase (GLOX) can be added to remove oxygen and has been shown to improve blinking [166, 198, 199]. To quench the triplet or the radical states and return a bleached molecule to bright state exposure of ultraviolet and violet light can help [200-202]. For further removal of oxygen, cyclooctatetraene (COT) can be added to the thiol based buffer in the presence of GLOX [106]. Anti-fading buffers such as Vectashield have also been shown to improve the blinking [170]. Sodium borohydride (NaBH4) is a reducing agent that can be used to convert the fluorophore to a long-lived 'caged' dark state. Upon UV illumination of the molecules, they can be photo-activated. Other successful methods have been to use inert gas such as argon or nitrogen [203], or vacuum [204] which are not biologically friendly.

Table 2-1- Comparison of different organic dyes used for SML imaging. Information about photon emission and Duty cycle are adapted from [105].

	Number of collected photons per localization event		Duty cycle at equilibrium		Lower bound of resolution (nm)		Accuracy of localization (nm)	
Dye ▼ | Buffer ►	**MEA**	**βME**	**MEA**	**βME**	**MEA**	**βME**	**MEA**	**βME**
Atto 488	1,341	1,110	0.00065	0.0022	9.23	16.98	11.18	12.28
Alexa Fluor 488	1,193	427	0.00055	0.0017	8.42	14.81	11.76	19.66
Alexa Fluor 647	3,823	5,202	0.0005	0.0012	10.29	15.94	8.41	7.21
Atto 647	1,526	944	0.0021	0.0016	21.22	18.52	13.39	17.03
Atto 647N	3,254	4,433	0.0012	0.0035	16.04	27.40	9.17	7.86

The Zhuang group has done extensive evaluation of many carbo-cyanine dyes that can properly be used for SML imaging [105]. The dyes were examined for their duty cycle, photon emission, sensitivity to uv re-energizing, and GLOX in presence of either thiol. We use their evaluation to calculate the upper bound of resolution found using equation 2.11.

Alexa Fluor 647 is the dye that emits the most photons. However, although Alexa Fluor 488 has a slightly higher duty cycle than Alexa Fluor 647 (in the presence of MEA), its upper bound on resolution is lower due to the shorter wavelength of emission. We have also calculated the accuracy of localization for each dye based on the photon emission and Considering the wavelength of emission, the number of photons, and the pixel size of our apparatus (89 nm), using equation 2.13. Considering all these factors, Alexa Fluor 488 and 647 show good performance for SML imaging under MEA buffer. According to [105] all the mentioned dyes have moderate to high sensitivity to both GLOX quenching, and UV reenergizing. The same analysis for QDs is presented in chapter 3.

2.5. Accuracy and resolution

The accuracy of SML particle tracking and imaging has widely been investigated in literature [104, 205-208]. The main factors are the sharpness of the PSF and the number of collected photons from the blinking event. Several other factors also add to make the error of localization larger; pixel size and background noise are among them. Another important factor that worsens the resolution and makes the images blurry is the mechanical stability of the apparatus. Due to high resolution of imaging, even nano-scale movements of the imaging stage add to the error of the imaging. In this section we review

the calculation of the error of localization, measurement of our system's mechanical stability, and two practical resolution approximation methods.

2.5.1. Error in estimation of the center of emission

Using propagation of uncertainty we can derive the error of the Gaussian profile of a PSF, Δx using the following equation:

$$\left\langle (\Delta x)^2 \right\rangle = \frac{s^2}{N} \tag{2.11}$$

where *s* is the width of the PSF, and *N* is the number of photons. This equation essentially calculates the error of the mean. Now to add the effect of pixilation to the error term, we can calculate the variance of the top-hat statistics [104], which is $a^2/12$. We can now add it directly to the error term (eq. 2.12), and yield:

$$\left\langle (\Delta x)^2 \right\rangle = \frac{s^2 + a^2/12}{N} \tag{2.12}$$

We used equation 2.13 and calculated the accuracy of localization in absence of noise for different fluorophores. The results are shown in Table 2-1, and the related discussion is in section 2.4. The variance of the localization error based on the noise due to shot noise, out of focus light, CCD read noise, dark current, and other factors is given by:

$$\left\langle (\Delta x)^2 \right\rangle = \frac{4\sqrt{\pi} s^3 b^2}{a N^2} \tag{2.13}$$

where b is the standard deviation of the background noise of the system. We can now add 2.13 and 2.14 to get a general term for the accuracy of localization:

$$\left\langle (\Delta x)^2 \right\rangle = \frac{s^2 + a^2/12}{N} + \frac{4\sqrt{\pi} s^3 b^2}{aN^2} \tag{2.14}$$

We can see from the equation that to get an acceptable resolution, we require smaller *s*, and higher *N*. The pixel size also plays an important role, which has to be in an acceptable range. The background noise is a very important factor and can dramatically reduce the localization accuracy.

2.5.2. Mechanical stability of the apparatus

Typically the data acquisition of SML takes tens of minutes. During this process, nanometer movements of the imaging stage can cause error in localization and make the reconstructed image blurry. Several methods have been suggested in the literature to reduce the drift. Mechanical isolation of the sample chamber from the rest of the system with temperature chambers [209], uncoupled sample holders [200], or feedback control loop [210, 211] have been implemented. More common approaches have been by post-treatment of the acquired datasets. Correlation of the acquired images with either widefield [212] or localization data [97, 213, 214], as well as anti-correlated analysis [215] of changes in the PSF for interferometric 3D SML are all approaches to tackle this problem. Applying fiducial markers to the sample, and tracking them over the period of imaging is also a method that has been used in many classical SML papers [15, 17, 216] to correct for stage drift.

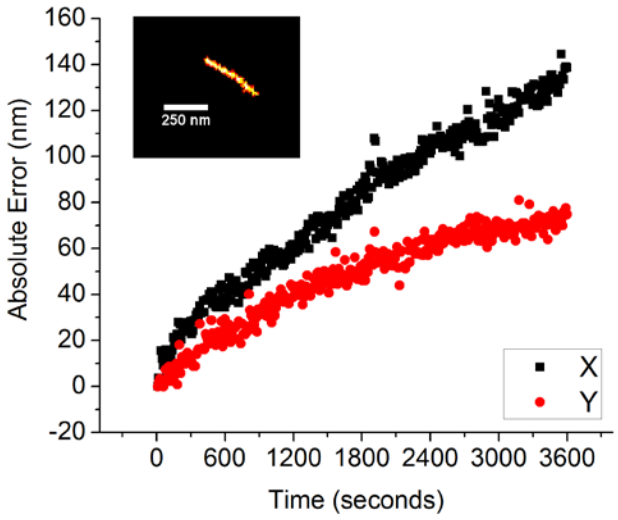

Figure 2-13 - Test of drift on a fluorescent Yellow-Green bead. Absolute error of the molecule position from the original position is shown in x and y direction.

We measured the drift of our stage, by image a fluorescent YG bead for a period of one hour, with 20-second intervals. An image of the localization and the absolute movement from the initial point are illustrated in Figure 2-13. The standard deviation of the drift in x and y directions are 70.3 nm and 40.12 nm respectively. Although the amount of drift seems very significant, however, we optimized our QD imaging – that will be presented in the next chapter – to acquire images in a time-scale of 3-6 minutes, which accounts for 3.5-7 nm in x direction, and 2-4 nm in y direction error. Based on our findings shown in Table 2-1, we assume these errors are negligible.

2.5.3. Practical measurements of resolution

With a-priori knowledge of wavelength and number of emitted photons, the accuracy of localization can be estimated using equation 2.15. However there are several factors, such as aberrations, that can corrupt the resolution of imaging that cannot be estimated using that model. Or in fact, measurement of those factors may not be

available. Image based resolution calculation techniques have been developed to estimate the resolution based on the acquired image datasets. Fourier Ring Correlation (FRC) [217], and Practical Localization Accuracy Measure (PLAM) [79] have been used for SML microscopy.

FRC was first developed to analyze EM microscopy images [218]. The FRC technique first divides the whole dataset into smaller stacks. The stacks are then reconstructed to get reconstructed sections of the image dataset. Next part of a structure is taken as reference and correlated with different reconstructed sections in the Fourier space. The correlation process produces rings in the Fourier space, corresponding to their spatial frequency. The more scattered the localization are, the more space the ring would cover. Thicker ring provides lower minimum spatial frequency threshold. This threshold is then assumed as the resolving frequency.

2.6. Localization and image reconstruction

The mostly commonly used algorithm for reconstruction of STORM images is least squares fitting of a 2D Gaussian function to a PSF that is isolated from the rest of an image by a thresholding method. The PSF has Gaussian profile (equation 2.15) which we can directly apply a fitting, by inversing the equation. However the accuracy of a direct fitting would be under scrutiny, due to large error that can be caused by presence of bias and noise. Other approach is by using iterative least squares error fitting, that iteratively reduce the error to an acceptable point.

$$I = \frac{I_{\max}}{2\pi\sqrt{\sigma_x \sigma_y}} \exp\left(-\frac{\left(x - x_0\right)^2}{2\sigma_x^2} - \frac{\left(y - y_0\right)^2}{2\sigma_x^2} \right) \tag{2.15}$$

By applying the fitting the standard deviation of the Gaussian profile in the horizontal and vertical directions can be recovered. This is particularly important in reconstruction of 3D datasets. More detail on 3D imaging will be presented in section 2.7. Many codes and software have been developed for this purpose [103, 219-222]. The most notable ones are RapidSTORM [222] and QuickPalm [221]. We have used RapidSTORM versions 2.21 and 3.2 for 2D and 3D image reconstruction in this dissertation respectively.

Other approaches such as wavelet base filtering and thresholding have also been reported [223]. In this method, by applying a threshold, the mass of a PSF is isolated, and a binary mask is made. Then the center of mass is found by averaging over the masked area. This method is developed to avoid iterative error minimizing, making reconstruction faster.

2.7. Multi-Color SML

Extension of dSTORM to multi-color is a trivial task. Non-spectrally-overlapping fluorescent molecule with stochastic blinking characteristic can be used with separate excitation and emission spectra to perform high resolution imaging. However, multi-color QSTORM has been a challenge due to the spectral shift of the QDs. In chapter 3 we present our solution to this problem.

SML imaging of mitochondria and microtubules has been previously reported with a number of different probes [96, 224, 225]. In Huang et al.[96], TOM20 in the mitochondria outer membrane was labeled with a photoswitchable probe consisting of A405 linked to Cy5. In Shim et al.[224], Mitotracker dyes are used to label the

mitochondria inner membrane. In van de Linde et al.[225], F_0F_1-ATPsynthase and cytochrome c oxidase are stained with Alexa 647. The antibody MTC02 recognizes a 60 kDa non-glycosylated protein component of mitochondria found in human cells, and has been used for mitochondrial content determination or mitochondria imaging in a variety of previous studies [226-228].

2.8. 3D technique

Several approaches have been used to achieve three-dimensional (3D) SML microscopy. A classical approach is by using a 4Pi setup to achieve interferometric [215, 229] optical sectioning and SML imaging with higher axial resolution. Biplane is another method that uses information acquired from two axially separate planes imaged simultaneously to calculate the location of particles [230, 231]. Wavefront coding to make PSFs that change in shape axially is another method. Double-helix PSF has been applied to SML imaging [100]. Although it makes very good axial resolution, however due to its non-trivial method it has not been commonly used. The next technique to achieve 3D SML imaging is by exploiting the shape of 3D PSF. The 3D shape of PSF can be used to estimate the axial position of a fluorophore. However because an unaberrated PSF has symmetry across the focal plane the direction of the displacement cannot be estimated. Therefore if two point have the same distance from the focal plane in opposing directions, they will be assume in the same position. To address this problem, a known amount of astigmatism can be applied to the system [97, 131]. Astigmatism causes an optical system to have a shift in focal plane between the x and y directions. In an astigmatic PSF, the width of the PSF in the x and y directions change independently as the imaging plane moves from the horizontal to the vertical focal plane. By applying

fitting to the astigmatic PSF, its width in x and y direction at a range of z position can be measured to produce a calibration curve. The calibration curve can then be used during image reconstruction to reveal information on the axial position of the fluorescent molecules.

We use our AO system to induce astigmatism in the optical path for 3D SML. Using the AO system, we applied 0.8 radians rms of astigmatism to the emission PSF. Figure 2-14 shows the calibration for 3D STORM using a 100nm fluorescent microsphere. Figure 2-11 (a)-(c) show the shape of the PSF at three positions, +400nm, 0, and -400nm with respect to the focal plane. We applied 2D Gaussian fitting to the PSF to determine the sigmas of the fit in the x and y directions as shown in Fig. 2-11(d). The two curves are used to find the Z position of the molecules. To test the accuracy of the system, we imaged a single fluorescent microsphere for 10,000 frames. The resulting localization data shows standard deviations of 7.7nm, 7.0nm, and 11.7nm in the x, y, and z directions respectively.

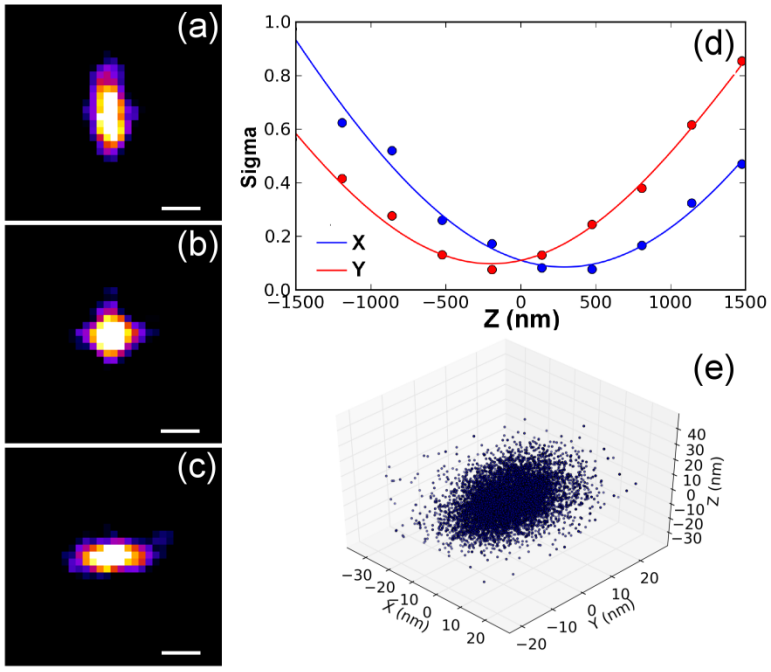

Figure 2-14 - Calibration of astigmatism. (a)-(c) Images of a 100nm fluorescent bead 400nm above focus, in focus, and 400nm below the focal plane with 0.8 radians of astigmatism added to the PSF with the deformable mirror. (d) Calibration of the astigmatism for three-dimensional STORM. (e) 10,000 localizations of a 100 nm fluorescent bead at 100 fps. The localizations have a standard deviation of 7.7nm in the x direction, 7.0nm in the y direction, and 11.7nm in the z (axial) direction.

We performed 3D dSTORM SML on *E.coli* bacteria. An example is shown in Figure 2-15. The bacterium's membrane is stained with Atto 647N dyes using mCLING technique [232]. 0.8 radian astigmatism was applied. Using MEA buffer the dyes were blinking for more than 30,000 frames at 110 frames per second. The image is reconstructed from 10,000 frames. More examples of 3D imaging using QSTORM technique is followed in section 3.11.

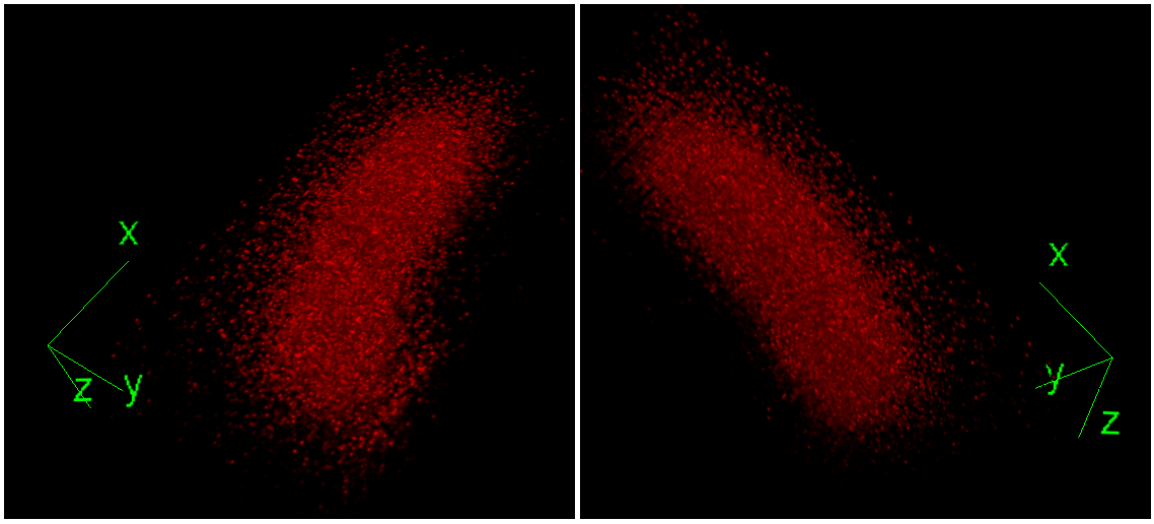

Figure 2-15 – Three dimensional imaging of an *Escherichia coli* bacterium. The cell's membrane is stained with Atto 647N dyes using mcling binding technique.

2.9. Conclusion

In conclusion we discussed the mechanisms for blinking for different fluorescent systems. Energy states of Fluorescent proteins, FRET on tandem dyes, and blinking of organic fluorophores were discussed. Quantum Dots were briefly introduced. Their application to SML is discussed further in chapter 3.

The effect of mounting media on blinking was presented. Based on information from the literature on the number of photons emitted and the blinking duty cycle we calculated the upper bound of resolution and accuracy of localization for several dyes in prepared in the two main SML imaging buffers. The measurement of drift and practical methods of calculating resolution were introduced. The FRC method is used in chapter 5 for estimation of resolution after correction of aberrations. Image reconstruction and 3D SML imaging were introduced. In chapter 3 we use Astigmatism to acquire 3D multi-color super-resolution images.

3. TWO-COLOR SML USING QUANTUM DOT BLUEING [1,2]

In the previous chapter we mentioned that QDs are brighter than organic dyes. It makes them a better choice for SML imaging than organic dyes, since the accuracy of localization is inversely proportional to the square root of the number of collected photons. One challenge in the past has been efficient methods to make QDs blink.

The blueing technique has helped to address this problem [108]. Blueing has many advantages over photo-switching of organic dyes. Organic dyes typically require undergoing a process of quenching of the excited state, and they need special buffers to return to fluorescing state. Some times a second laser should also be used to re-excite them. QDs do not need to be quenched, only a single laser is required for excitation of multiple emission wavelength QDs, and no external chemicals are needed. Additionally, for conventional switchable dyes, each dye molecule can photoactivate multiple times which, on one hand, can enhance the signal, but on the other hand, also allows each probe molecule to sample different locations of the structure in different camera frames and to contribute multiple independent localizations which may result in a potential motion blurring [224]. QD blueing will only localize each molecule once, and, because QDs are

[1] Reproduced in part with permission from J. Xu, K. F. Tehrani, and P. Kner, "Multicolor 3D Super-resolution Imaging by Quantum Dot Stochastic Optical Reconstruction Microscopy," ACS Nano 9, 2917-2925 (2015). Copyright (2015) American Chemical Society. The material is available online at: http://dx.doi.org/10.1021/nn506952g

[2] Reproduced in part with permission from "Multi-color quantum dot stochastic optical reconstruction microscopy (qSTORM)," Proc. SPIE 9331, Single Molecule Spectroscopy and Superresolution Imaging VIII, 93310C (2015). Copyright 2015 Society of Photo-Optical Instrumentation Engineers. http://dx.doi.org/10.1117/12.2077293

intensely bright, can still provide enough photons for accurate localization and homogenous image reconstruction. We refer to this technique as Q-STORM.

Multi-color imaging is an essential tool in biological studies for observation of the structure and interaction between different proteins. While SML microscopy with fluorescent proteins and organic dyes has been easily extended to multi-color imaging [233-236], a similar approach with the QD blueing technique had not been tried. In this chapter we present the extension of QD blueing to two-color imaging. We demonstrate multi-color QSTORM using 565 nm and 705 nm emitting QDs to image microtubules and mitochondria in Eukaryotic cells. We show that the QDs exhibit up to a 80nm blue shift (longer than previously reported [237]). We optimized the rate of blueing, which helps reduce the fraction of QDs in the bandpass window – the equivalent of the duty cycle with organic dyes - to improve the lower bound of resolution. Finally, astigmatism was applied to image the two blueing channels in 3D.

3.1. The principle of two-color blueing

Although single color blueing has been done before, its extension to two-color imaging has been a challenge. Since the QDs undergo a spectral shift of emission the choice of parameters becomes important. Parameters such as the spectral overlap, rate and amount of blueing, play key roles in choosing the dye as well as the filters. In fact since the QDs have broad excitation spectrum, they have to be imaged simultaneously. The first challenge for two-color QSTORM is to choose QDs that have distinct emission spectra, but which are still close enough to fit inside the wavelength range of the CCD. We started our experiments by using 545 nm and 655 nm QDs. We later switched from 545nm QDs to 565 nm due to commercial availability, and then we switched from 655nm

QDs to 705 nm to minimize their emission spectral overlap. The emission spectrum of 655nm QD is shown in Figure 3-1, in relation to 565nm QD and a 605/15 narrow-band-pass filter. The emission overlap from the QD 565nm channel is non-negligible. Therefore we also changed the filter to 625/15 nm in addition to switching to QD 705nm.

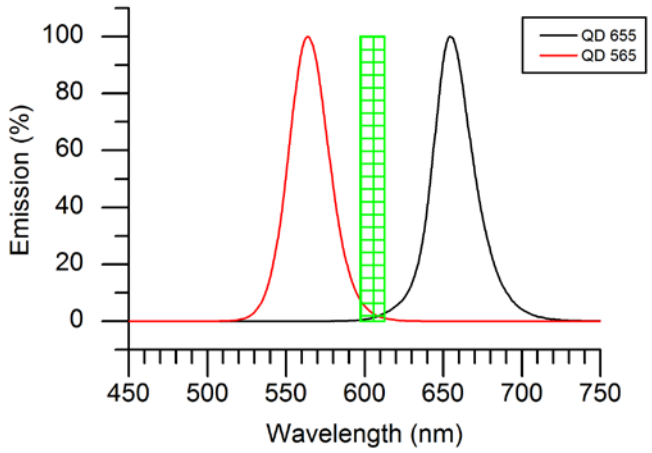

Figure 3-1 - Emission and absorption of QD 565 nm and QD 655 nm. The hashed area shows a 605/15 nm band-pass filter used initially for blueing.

Measurements of emission and excitation spectra of the QDs used in this research are shown in Figure 3-2. The excitation spectra were acquired by measuring the emission at the nominal wavelength of the QD. The emission spectra of the QDs were measured while excited using 488nm light. The excitation spectrum of the 705nm QD shows a peak at 355nm. Measurement of emission using 355nm excitation light, indicate that two sizes of QDs were in the solution, with average wavelengths of 680nm and 704nm. However when excited with 488nm the QDs with average wavelength of 680nm dominated the emission.

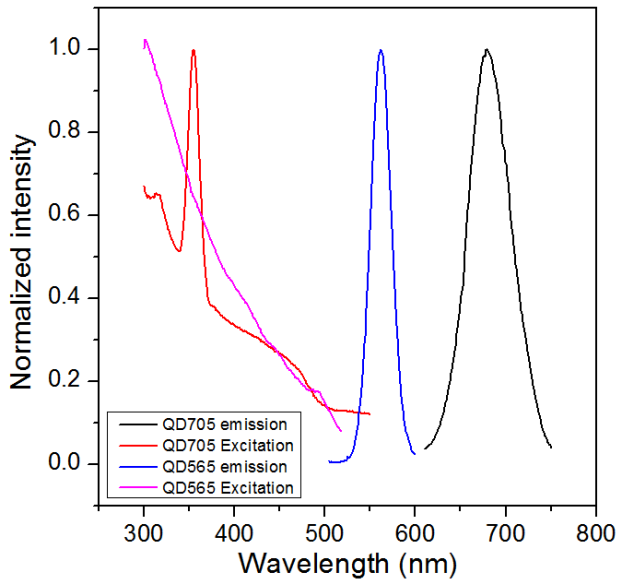

Figure 3-2 - Excitation and emission spectra of antibody conjugated quantum dots.

Figure 3-3 demonstrates the principle of two-color QSTORM. The emission spectra of QDs vary with particle size due to quantum confinement. For core/shell CdSe/ZnS quantum dots, under continuous illumination, the size of the CdSe core shrinks due to the photo-induced oxidation which results in the shift of the fluorescence emission to shorter wavelengths [108] as described in section 2.2.4.1. This effect is referred to as "blueing". As shown in Figure 3-3, two sizes of CdSe QDs (QD 705 nm and QD 565 nm) are chosen as the probes, and two narrow bandpass filters (625nm center/15nm width and 504nm center/12nm width) are used to collect the emission from the two QDs respectively. Due to the asynchronous blueing of the QDs, it is unlikely that multiple QDs within a diffraction-limited area will blue at the same speed and emit in the pass band simultaneously. Therefore individual QDs will be detected and localized.

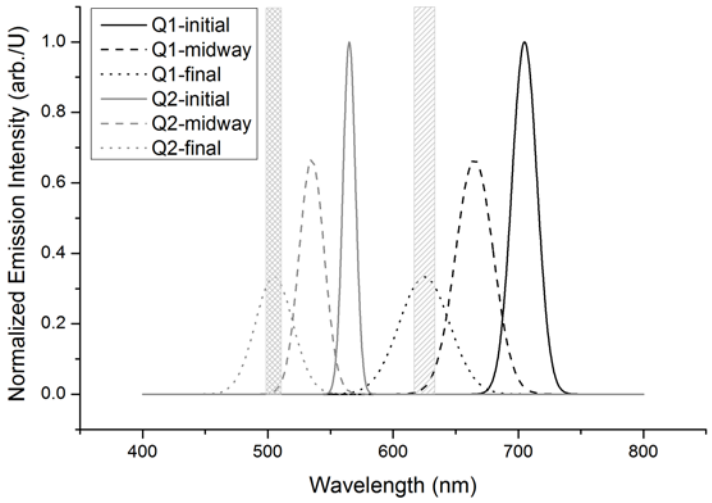

Figure 3-3 – Schematic presentation of the blueing process for 565nm and 705nm QDs. Solid lines show the initial emission spectra of the QDs. Long and short dashed lines show the shifted emission spectra after a few thousand exposure cycles. The single and double hashed areas show the respective filters for the NIR and the visible wavelength QDs.

3.2. Optical apparatus

The optical system is shown in Figure 3-4. The microscope contains a deformable mirror (DM) at a conjugate plane to the back pupil plane of the objective. The DM is used to maintain a Strehl ratio of greater than 0.80. It is also used to induce Astigmatism for 3D imaging. For simultaneous imaging of the two channels a home-built optical splitter is placed to separate the two channels using a dichroic mirror. The emitted light from each channel is send to their corresponding narrow-bandpass filters (F_1 and F_2). Detailed drawing and pictures of the splitter are shown in appendix B. A neutral density filter was also used to attenuate the signal from the red channel, so that higher electron multiplying (EM) gain can be applied to the green channel, without saturating the red channel.

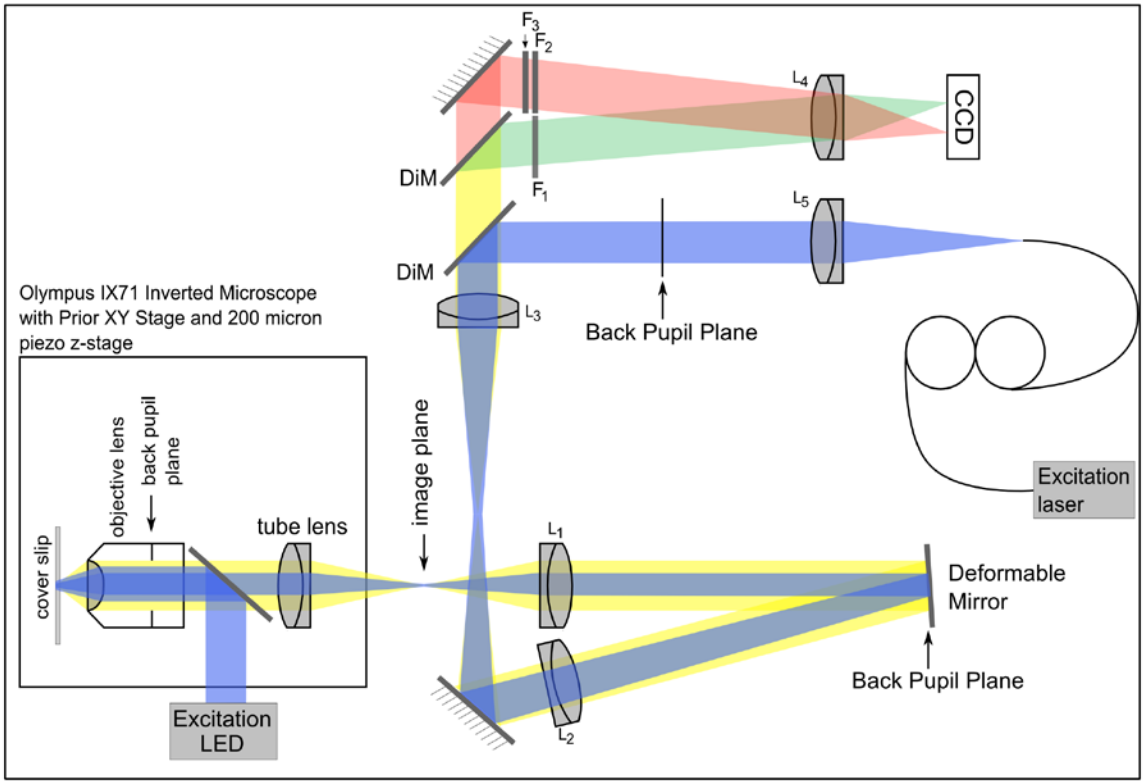

Figure 3-4 - Schematic of the optical setup. L1 and L2 are 350mm efl achromats. L3 is a 100mm efl achromat. L4 is a 300mm efl achromat, and L5 is a 7.86mm asphere

3.3. Single color Q-STORM sample

In Figure 3-5, we show single-color STORM images of microtubules stained with 565nm and 705nm QDs. These images show that 565nm and 705nm QDs perform equally well as labels for STORM. In Figure 3-5 (c-d), two individual microtubules are clearly separated which cannot be resolved in the widefield image. From measurements of individual QDs, we determine the lateral resolution to be 24nm.

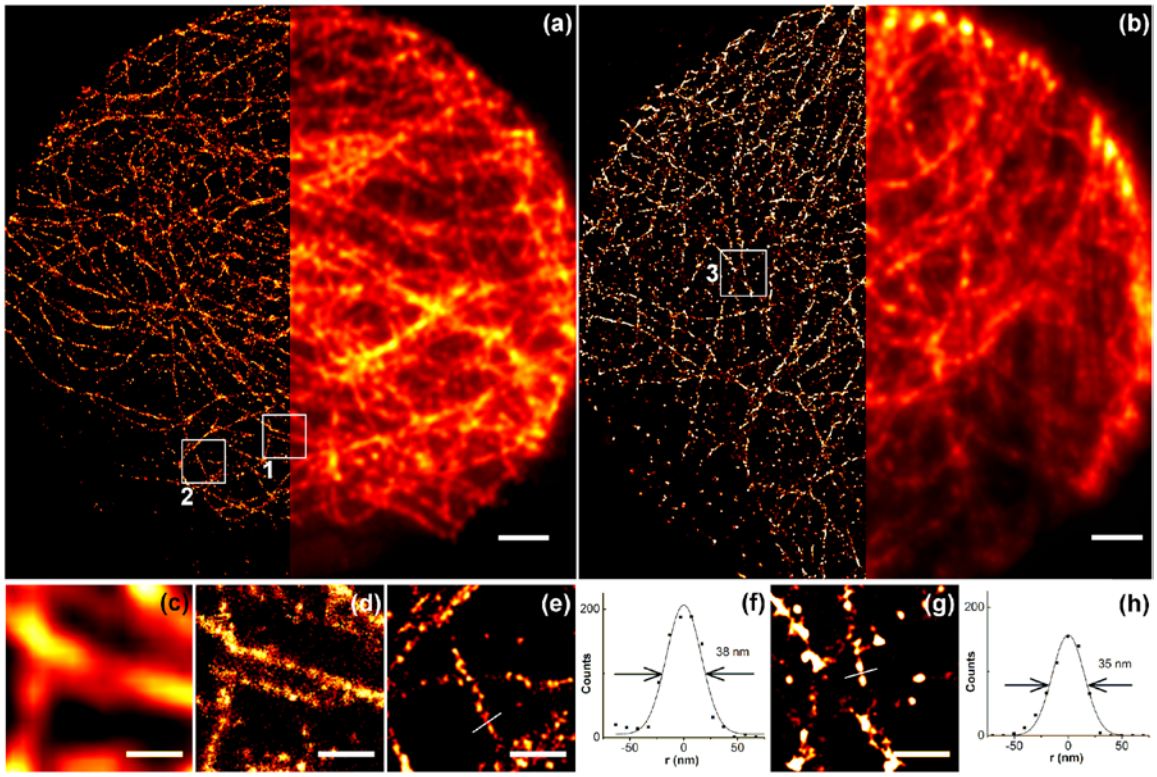

Figure 3-5 - (a-b) STORM (left) and widefield (right) images of microtubules in HepG2 cells labeled with 565nm and 705nm QDs respectively. Scale bar is 2µm. (c-d) Widefield and STORM images of box 1 in (a). Scale bar is 500nm. (e) STORM image of box 2 in (a). Scale bar is 500nm. A cross section of a microtubule is shown in (f). The full-width half maximum is 38nm. (g) STORM image of box 3 in (b). Scale bar is 500nm. A cross section of a microtubule is shown in (h). The full-width half maximum is 35nm.

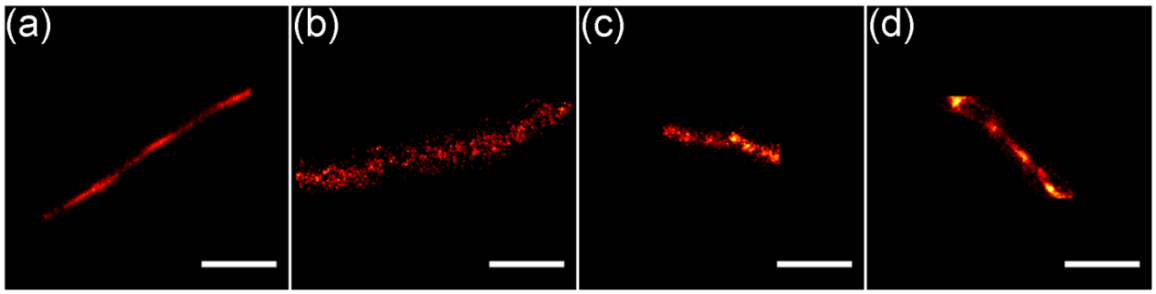

Figure 3-6 - A Gallery of microtubule image sections labeled with (a) Alexa 488, (b) Alexa 647, (c) 565nm QDs, and (d) 705nm QDs. Scale bars are 500nm.

A criticism of QD labeling is that the larger size of QDs will limit the achievable resolution due to the Nyquist sampling criteria [238]. We measure an average microtubule FWHM of 60±12nm from QSTORM images by performing Gaussian fits to the cross-section of 12 microtubules averaged over ~500 nm of length as shown in Figure 3-6. The best images produce a width of 46nm. This is slightly larger than previous measurements of the microtubule width from STORM imaging [108, 239] indicating that the QD size increases the effective width by ~10nm. The microtubule diameter is 25nm determined by transmission electron microscopy.[240] The size of quantum dots is only a few nanometers, but coatings for biocompatibility and functionalization are usually required for biology applications, which will increase the final labelling size to ~20nm, and the size of a typical IgG antibody is about 7 nm [241] Considering the size of primary antibodies and QD labeled secondary antibodies on either side of the microtubule, our measurements match the size of the labeled microtubule. By labeling microtubules using nanobodies, the diameter of microtubule has been measured as 26.9±3.7nm with single-molecule nanoscopy [242].

3.4. Comparison with Organic dyes

Compared to organic dyes, QDs show remarkable photostability and brightness. Even though the intensity decreases during the blueing process, they still emit a large number of photons before being bleached. We compared QSTORM to STORM with Alexa 647, which is considered one of the most efficient cyanine dye labels for STORM imaging [243]. The cyanine dyes can be turned on and off reliably for hundreds of cycles before photobleaching, and the size of the dye molecule is very small, allowing high resolution STORM imaging [244, 245]. For QD blueing, each QD is detected only once,

but due to the high quantum yield, many photons can still be collected. Figure 3-7 shows the histograms of photon counts for the two QDs and Alexa 647. Comparing histograms of the Alexa 647 with the 565nm and 705nm QDs, we can see that there are more photons emitted from the QDs. We tested this by acquiring STORM images on microtubules of hepG2 cells stained with Alexa 647, 565nm QDs, and 705nm QDs. The average photon counts were 1414, 3753, and 7023 for Alexa 647, 565nm QDs, and 705nm QDs, respectively. Accurate localizations by the large photon number is a major advantage of QSTORM imaging over other stochastic approaches using organic dyes or fluorescent proteins. The large photon count is even more important for obtaining high resolution in the presence of background fluorescence (from auto fluorescence or out-of-focus fluorescence in thick samples). As we mentioned in section 2.5.1 large background reduces the accuracy of the localization, and hence worsens the resolution. We calculated the accuracy of localization for the QDs used in this study, as shown in Table 3-1. QDs provide at least a factor of two better accuracy of localization compared to comparable organic dyes.

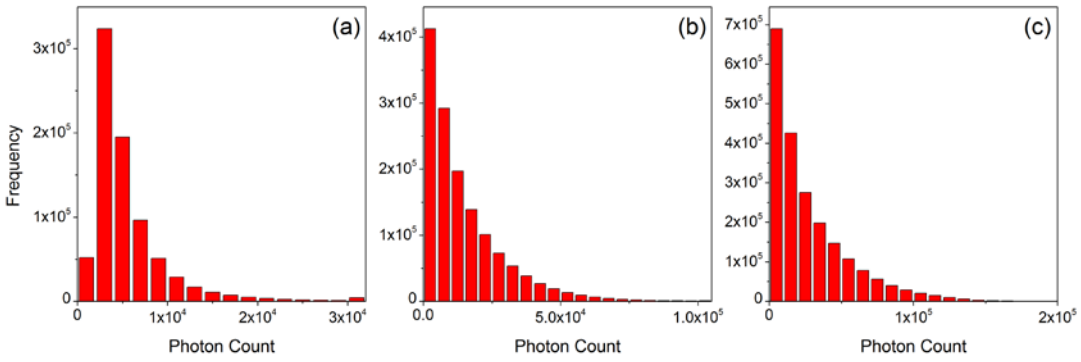

Figure 3-7 - Histograms of photon counts per switching event for (a) Alexa Fluor 647, (b) QD 565nm (c) QD 705nm.

3.5. Blueing Speed optimization

An important aspect of the blueing process for single molecule localization is the speed of the photooxidation. If the molecules blue too quickly, then too many QDs will emit in the passband in each exposure, so the likelihood of detecting single QDs in a diffraction-limited area will be too low and all the QDs will photooxidize too quickly resulting in too few localizations per raw frame. If the QDs blue too slowly, too few single QD emissions will be captured per frame. Then, the experiment will take too long resulting in too much mechanical drift during the measurements. The resolution of STORM imaging depends on both the photons collected from each QD and the number of localizations [238]. By controlling the blueing rate both can be improved.

Here we show that the blueing speed can be optimized by optimizing the laser intensity and the mounting medium. The blueing behavior of QDs mounted in different concentrations of glycerol (0%, 10%, and 20% v/v) in PBS was characterized. With more glycerol, there is less Oxygen available for the photo-oxidation, and the QDs will blue more slowly.

In Figure 3-8, we show STORM images obtained under different conditions. In Figure 3-8 (a)-(c), STORM images of microtubules labeled with 565nm QDs in different concentrations of glycerol are shown. With no glycerol in the mounting medium, there are an insufficient number of localizations (2,290 μm^{-2}). The filamentous structure of the microtubules can be seen but the fidelity of the image is not good and many of the microtubules are discontinuous. The number of localizations is increased by adding 10% glycerol to the mounting medium (4,474 μm^{-2}), and the intact microtubules network can be seen in Figure 3-8 (b). Increasing the concentration of glycerol to 20% did not change

the microtubule structure significantly. However, for the images of mitochondria which were labeled with 705nm QDs, the STORM image quality taken with 10% glycerol, Figure 3-8 (h), is not good enough to resolve the intact morphology of mitochondria even though it is a significant improvement over the sample mounted in PBS only, Figure 3-8 (g). There are 553 μm^{-2} localizations with 10% glycerol compared to 289 μm^{-2} localizations for PBS only. High resolution images of mitochondria were obtained with samples mounted in 20% glycerol, Figure 3-8 (i), with 1,658 μm^{-2} localizations. Increasing the glycerol concentration above 20% did not improve the imaging. With a 50% glycerol concentration, the QDs were still blueing after 50,000 frames at 50 frames per second with many QDs still not having reached the passband. In Figure 3-8 (d)-(f) and (j)-(l), we show the average number of photons per localization against frame number for the STORM images in Figure 3-8 (a)-(c) and (g)-(i) respectively. With increasing amounts of glycerol the curve peaks later and spreads out indicating a slower blueing rate and more localizations at later times. Based on these results, the two color imaging discussed below was performed on samples mounted in 20% glycerol.

Table 3-1 – Lower bound of resolution and accuracy of localization for 565 nm and 705 nm QDs.

	Wavelength of center of passband (nm)	Number of collected photons	Lower bound of resolution (nm) for different concentration of glycerol			Accuracy of localization (nm)
			0 %	10 %	20 %	
QD 565	504	3753	5.5	4.2	3.1	6.44
QD 705	625	7023	16.8	10.4	6.6	5.83

We further analyzed the QD blueing by calculating the ratio of localized QDs per frame to the total number of localizations, Figure 3-8 (m) and (n). This ratio represents an upper bound on the duty cycle — the number of emitting QDs to the total number of QDs. Along with photon emission and labeling density, the duty cycle, r, affects the possible resolution. The labeling density must be adjusted to avoid simultaneous emissions within a diffraction limited area. For higher values of *r,* the labeling density must be lower [246]. We calculate a lower bound on the resolution using equation 2.11 by using the maximum emitting fraction over the course of the measurement as r_{max}.

Using the data in Figure 3-8 (m) and (n), we calculate a lower bound on the resolution of both QDs for 0%, 10% and 20% concentrations of glycerol in PBS respectively. The localization software rejects all fluorescent spots which are too large or asymmetric, so the data represents to a high probability only single QD emissions. As demonstrated in Table 3-1 there is a considerable improvement in the resolution by increasing the glycerol concentration. Increase in the total number of localizations by decreasing the oxygen content of the mounting media is shown in Figure 3-8 (o).

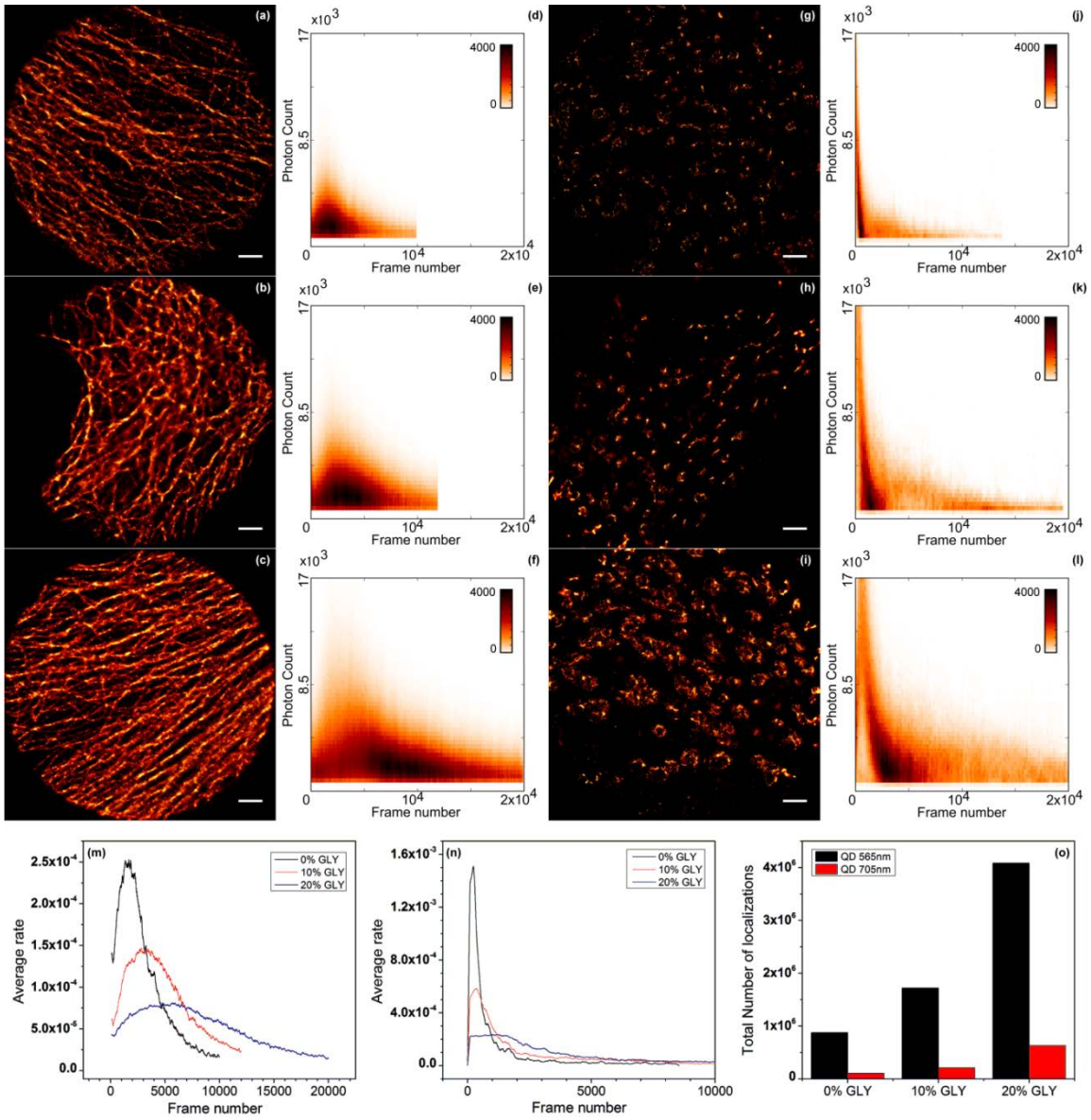

Figure 3-8 - STORM images of microtubules labeled with 565nm QDs and mitochondria labeled with 705nm QDs in HepG2 cells in PBS mounting media with 0%, 10% and 20% concentrations of glycerol. (a-c) Images of microtubules in 0%, 10%, and 20% concentrations of glycerol respectively. (d-f) Plots of average photons per localization (averaged over 100 frames) vs. frame corresponding to (a-c). Color indicates number of localizations (g-i) images of mitochondria in 0%, 10%, and 20% concentrations of glycerol respectively. (j-l) Plots of average photons per localization vs. frame corresponding to (g-i). The colorbar indicates the number of localizations. At least 10,000 frames were collected in total for each experiment at a laser intensity of 3.65 kW/cm2. Scale bars are 2µm. (m-n) Average fraction of total localizations per frame. (o) Total number of localizations for different percentages of glycerol.

3.6. Efficiency of Blueing

To measure the percentage of QDs that undergo blueing, a layer of 565nm IgG conjugated QDs were dried on a glass coverslip and mounted in a 20% glycerol / 80% deionized water solution. The QDs were imaged at 50 frames per second under continuous exposure to 10mW of 488nm excitation. A measurement consisting of 4 cycles of blueing followed by a measurement at the original emission wavelength was performed. 5000 frames were measured with a 504nm/12nm filter followed by 500 frames measured with a 580nm/60nm filter to detect remaining QDs. These measurements demonstrate that 95% of the QDs are blued in 5000 frames. The rate of blueing may be somewhat slower in cells as compared to directly exposed to the buffer.

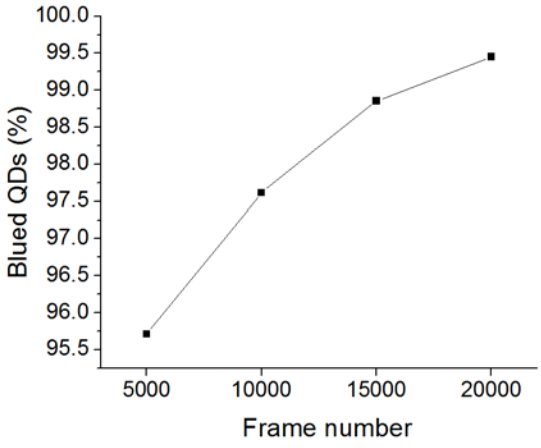

Figure 3-9. Percentage of blued QDs with emission between 550nm and 610nm (emission measured with a 580/60 nm emission filter) *vs.* the number of frames measured at 50fps. The QDs were continuously exposed to 10mW of 488nm excitation.

3.7. Practical calculation of resolution

We measured the resolution of our localization from the fitting parameters by calculating the standard deviation of the uncertainty in the fit to a Gaussian for several single QDs in single color STORM images shown in Figure 3-10 (a) and (b). This method has also been used by Hoyer *et al.*[108] to find the resolution. The resolution of our imaging was found to be 24 nm laterally and 37 nm axially.

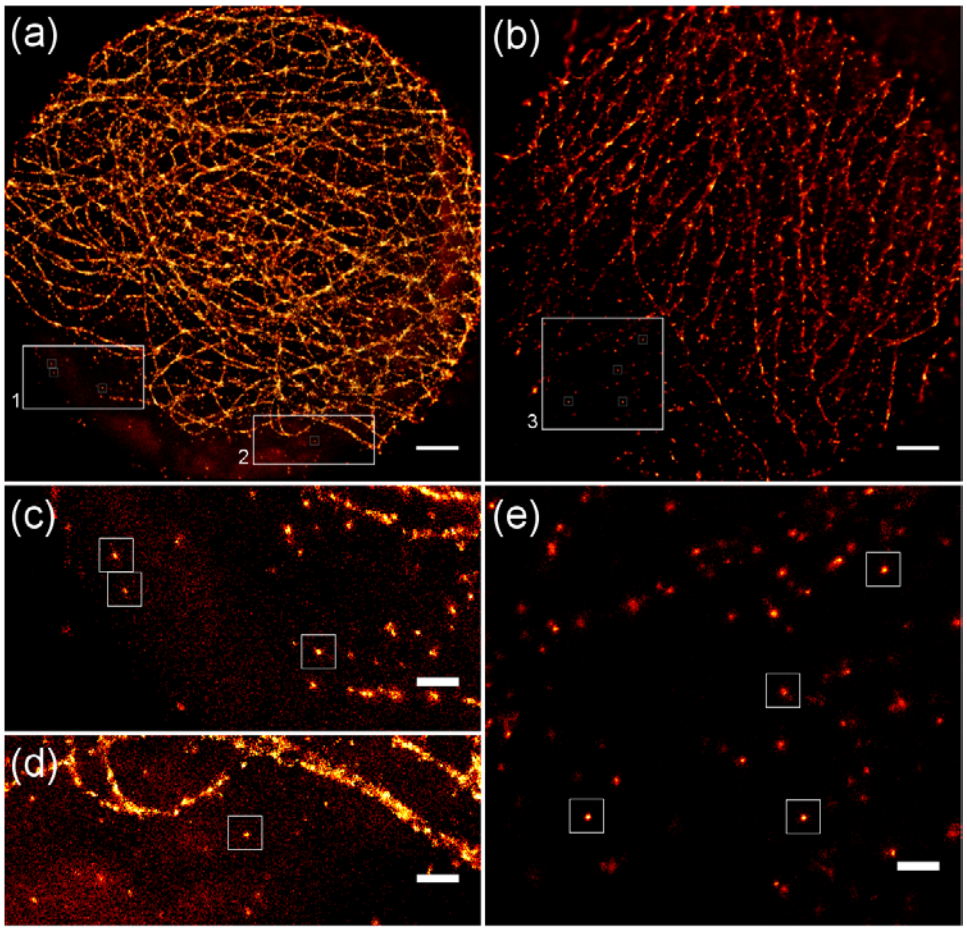

Figure 3-10 - Shows a few single QDs used for the calculation of resolution. (a) and (b) show the samples stained with 565nm QD and 705nm QD respectively. The scale bars are 2 µm. (c-e) are the magnified images of 1-3. Scale bars are 500nm.

3.8. Chromatic Calibration

200 nm TetraSpec™ fluorescent microspheres (Invitrogen) were diluted 1:100 to get a distribution of about 20 beads in an area of $380\mu m^2$ (excitation spot diameter 22μm). The solution was dried on a No. 1.5 cover slip and mounted on a microscope slide using glycerol. The microspheres' emission wavelengths include 515 nm and 680 nm, allowing both channels to pass through the blueing filters. Both channels were excited using the 488nm laser, and the emission intensity of the channels was equalized by a neutral density (ND10) filter in the Green channel. To increase the signal to noise ratio, each location was imaged 100 times (at 33 frames per second) and averaged. 121 locations on the slide (on an 11x11 grid) were imaged resulting in 1,928 microsphere localizations. In each image the microspheres were localized by Gaussian fitting. The difference in red channel and green channel location as a function of microsphere location (green channel) was then fit to a 2^{nd} order polynomial as shown in Figure 3-11 (a). For calibration of 3D imaging, astigmatism (0.8 radians RMS) was applied to the wavefront and the same procedure was repeated on 2,968 microsphere localizations, Figure 3-11 (b). The chromatic correction is demonstrated on microtubules doubly labeled with 565nm and 705nm QDs, Figure 3-11 (c-e).

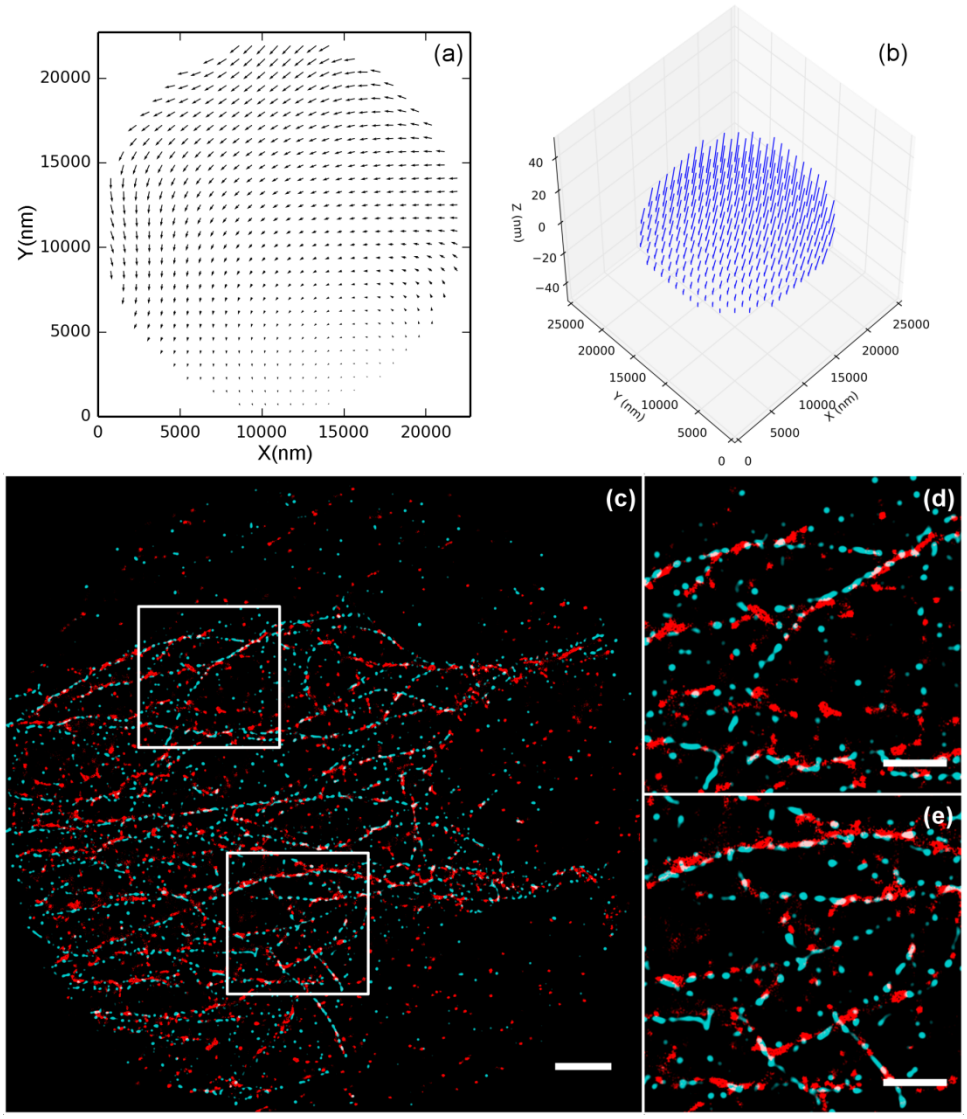

Figure 3-11 - Chromatic correction of two-color STORM. (a) Two-dimensional chromatic correction calculated from a multicolor image of tetraspeck beads. (b) Three-dimensional chromatic correction. (c) Corrected images of microtubules labeled with 565nm QDs (blue) and 705nm QDs (green). Scale bar is 2μm. (d) Image of upper boxed region in (c). (e) Image of lower boxed region in (c). Scale bars in (c) and (e) are 1μm.

3.9. Cross talk

Figure 3-12 shows measurements of single-color STORM measured with both the green filter and the red filter, indicating that very few localizations are detected in the wrong channel. 705nm QDs are completely oxidized before the emission wavelength of the blueing QDs reaches the 504nm bandpass filter used to detect the blueing 565nm

QDs. The number of false positives in the blue channel from the 705nm QDs is less than 0.3% (Table 3-2). The number of false positives is higher for the 565nm QDs in the red channel (1.35%) due to the tail of the unoxidized QDs overlapping the red filter. The majority of these false positives as shown in Figure 3-13 occur within the first 800 frames so the false positive rate can be reduced by dropping the first frames or simply waiting to start the measurement.

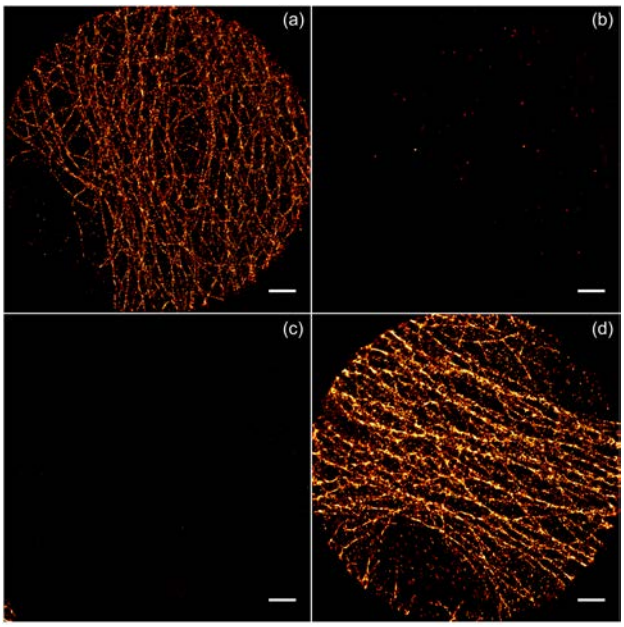

Figure 3-12. Determination of crosstalk between the two channels. (a)-(b) STORM measurement of 565nm QD labeled microtubules in HepG2 cells. (a) Measurement in the blue-channel (504nm center, 12nm bandwidth). (b) Measurement in the red channel (625nm center, 15nm bandwidth). (c)-(d) STORM measurement of 705nm QD labeled microtubules in HepG2 cells. (c) Measurement in the blue channel. Almost no events are detected. (d) Measurement in the red channel. Scale bars are 2 μm.

Table 3-2 – Analysis of cross talk between the two blueing channels.

QD type	Number of localizations		Ratio (unwanted to wanted)
	G Channel	R Channel	
565	812,227	11,075	0.013635
705	4,836	1,807,726	0.002675

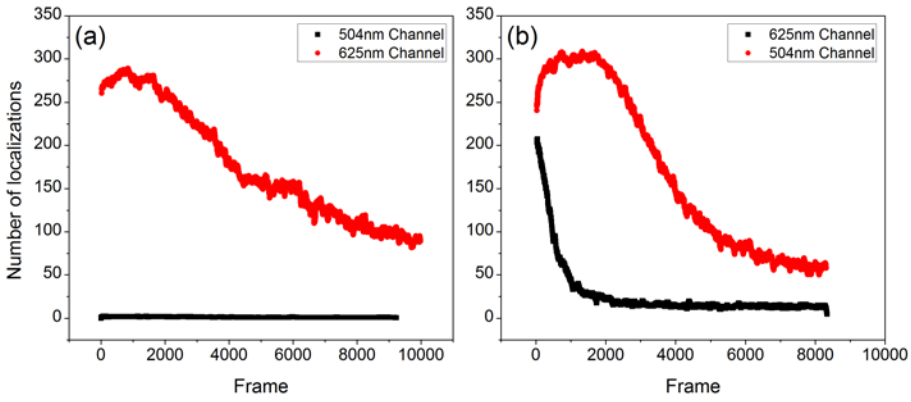

Figure 3-13 - Measurement of Crosstalk. The number of localizations for red and green channels are shown for microtubules of hepG2 cells stained with QD 705nm in (a) and with QD 565nm in (b).

3.10. Multi-Color QSTORM Imaging.

Here we use MTC02 antibody (as explained in section 2.7) for QSTORM SML imaging to demonstrate the morphology of mitochondria as well as their relationship with microtubules. Figure 3-14 shows multicolor widefield and STORM images presented at different scales. Compared to the widefield image, the STORM image provides more detail of the structures of the microtubules and the mitochondria as well as their relationship. The distribution and morphology of the mitochondria are also demonstrated in the STORM images. As can be seen in Figure 3-14, the mitochondrial distribution is heterogeneous, much denser near the nucleus where the energy requirement is higher [247]. Furthermore, heterogeneous mitochondrial morphologies — elongated, tubular and short, globular — are observed. Most of the mitochondria, but not all, are in contact with and aligned along the microtubules, consistent with the fact that mitochondria are predominantly transported along the microtubule network in mammalian cells [248, 249]. The tubular mitochondria are often aligned along the microtubules (Figure 3-14 (d)), but it has also been reported that sometimes such connections between the mitochondria and

microtubule are noncontiguous, and such inchworm-like contact is considered to aid transport [236, 248]. Mitochondria are highly dynamic organelles that often change morphology; fusion and fission of mitochondria have been imaged over time by live confocal microscopy [250], as well as live STORM imaging [224]. In our work, we also observed that two mitochondrial compartments could be connected by a thin, extended tubular structure (Figure 3-14 (f)). Such tubular intermediates are not clearly resolved in the widefield images.

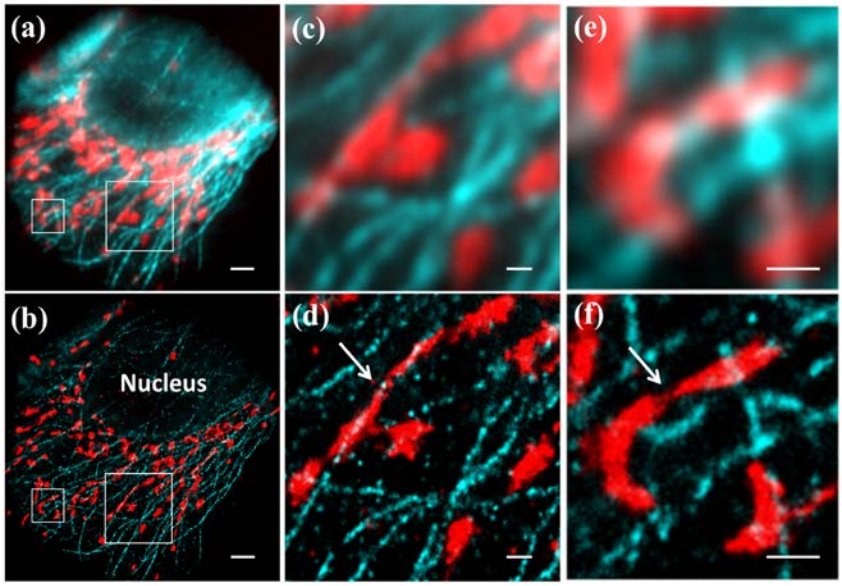

Figure 3-14 - Two-color STORM images of QD565-microtubules (blue) and QD705-mitochondria (red). (a) and (b) are widefield and STORM images respectively. Scale bars are 2μm. (c)-(d) Magnified images of the boxed region on the right in (a) and (b). Scale bars are 500 nm. (e)-(f) Magnified images of the boxed region on the left in (a) and (b). Scale bars are 500nm.

3.11. Multi-Color 3D QSTORM Imaging by Astigmatism.

We have also extended two-color QSTORM to three-dimensional imaging by applying astigmatism to the deformable mirror to create an astigmatic PSF [97, 131], as discussed in section 2.7. The results are shown in Figure 3-15. These images clearly show the three-dimensional arrangement of the microtubules and mitochondria although the

number of localizations is reduced compared to 2D STORM because of the larger astigmatic PSF. The 3D images give more details of the spatial relationship between the mitochondria and microtubules, which can be obscured in conventional or 2D STORM images. It can be clearly seen in the 3D images that the microtubule and mitochondrial networks are strongly interwoven with each other, and the mitochondria can be tightly wrapped around the microtubules rather than just attached to them. The interwoven structure between mitochondria and microtubules has also been observed by 4Pi microscopy using QD staining [251].

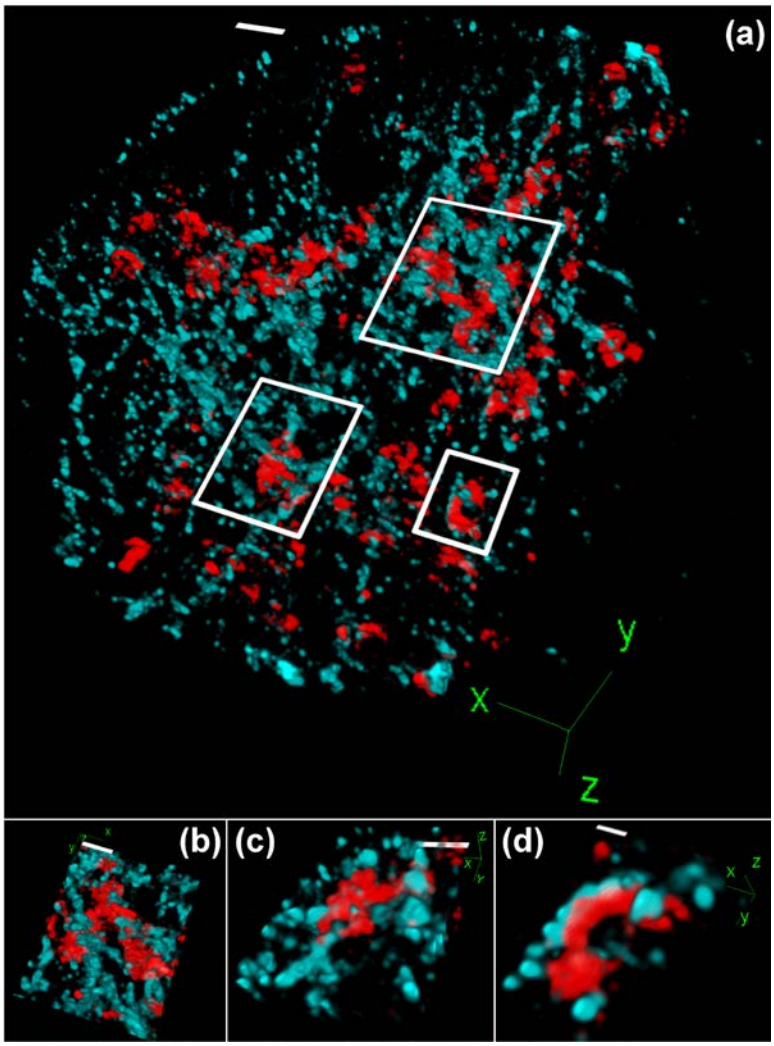

Figure 3-15 - Three-dimensional STORM images of microtubules (blue) and mitochondria (red) in HepG2 cells. (a) large field of view. Scale bar is 2μm. (b)-(d) close-up images of the boxed regions in (a). Scale bars are 500nm.

3.12. Conclusion

In conclusion, we have demonstrated that super-resolution imaging with quantum dots can be extended to multiple colors without sacrificing resolution. We demonstrate that the quantum dot blueing process can be controlled to maximize the number of achievable localizations, and we report on careful measurements of the microtubule width

measured with QSTORM and demonstrate that indeed higher photon counts can be achieved with quantum dots.

Here we have demonstrated multicolor QSTORM using two QDs that are far apart in initial wavelength allowing us to completely separate the blueing emission into separate channels.

4. ADAPTIVE OPTICS FOR MICROSCOPY

All of the SML experiments demonstrated in the previous chapters were done on very thin biological samples with the plane of interest very close to the surface of cover glass. As the plane of interest goes further inside the biological sample, the PSF shape is deformed and the PSF peak intensity drops. This is because a biological sample is made of many different materials with different indices of refraction. The light that propagates through such media will be refracted and scattered. Luckily, using technology adapted from astronomy — Adaptive Optics (AO) — we are now able to compensate for these variations in refractive index. AO is now applied to many microscopy techniques. Several variations of correcting elements, wavefront sensing elements and techniques, as well as wavefront sensor-less approaches have been developed. In this chapter we first discuss more in depth the sources of aberrations. The discussion of correcting elements then follows. A discussion of direct and indirect wavefront measurement comes afterwards. And finally correcting algorithms will be discussed.

4.1. Aberrations: Sources and models

For a plane beam of light travelling in space, all continuous points with the same phase make a wavefront. Therefore, planes of the same phase are separated by intervals of the wavelength. A complex pupil function P defines the beam in the pupil by its amplitude A, and phase Ψ [252]:

$$P(r,\theta) = A(r,\theta)\exp\left(j\left[\Psi_0 + \Psi(r,\theta)\right]\right) \tag{4.1}$$

where Ψ_0 is an arbitrary offset of the wavefront, and $\Psi(r,\theta)$ represents the deviations of phase due to aberrations. In an ideal infinity-corrected imaging system, a spherical wavefront made by a point source makes a flat plane-wave after being collimated by the objective. However, imperfections in the optical elements, misalignments, and changes in the indices of refraction of the biological sample cause non-uniform delays in the phase, such that each point on the wavefront becomes the sum of all the phase delays on its path [120, 253, 254]. The wavefront takes an irregular shape due to all the phase delays. With the irregular shape of wavefront, there is no guarantee that all the rays of light converge to a single point. The result is an aberrated PSF; the standard deviation *s* is increased and the intensity peak of the PSF *N*, decreased. We know from chapter 2 (section 2.5) that the resolution of SML is proportional to $s/\sqrt{N}$. Therefore the aberrated wavefront directly affects the resolution.

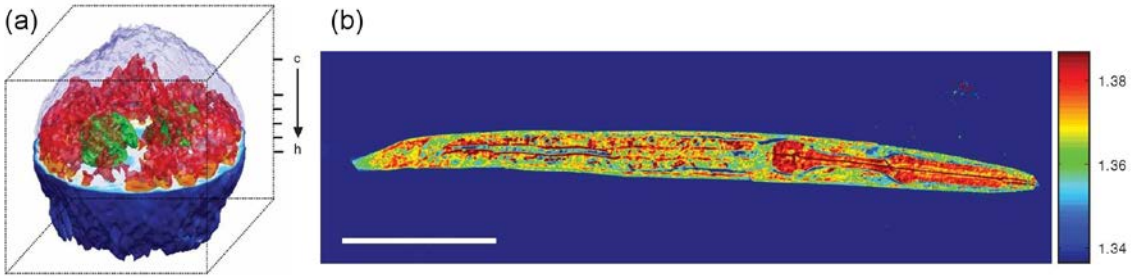

Figure 4-1 - Tomography reveals the variations of refractive index in throughout (a) a Hela cell and (b) a *C.elegans* worm. Adapted from [255].

4.1.1. Optical aberrations

Imperfection in the optical elements and their misalignment cause some of the very common optical aberrations: defocus, astigmatism, coma, and spherical aberration, as shown in Figure 4-2. Tip and tilt corrections which are the main issues in astronomy

are not generally considered aberrations in microscopy. Now let's define the terminology of some of the very common aberrations we are concerned with in this chapter and in chapter 5. One form of aberration is Defocus; as the name suggests it occurs when the focal plane is displaced from the imaging plane. The next one is Astigmatism, which is caused by a lens that lacks symmetry about the optical axis. The next aberration, coma, occurs when an off-axis point is imaged, and the PSF takes the shape of a comet. An important aberration that is especially important in high NA systems is Spherical aberration. The parabolic shape of a lens causes the angled beams in different distances from the optical axis do not converge to the same point. This is due to a curvature caused by the difference between the spherical wavefront and parabolic shape of the lens, which can be corrected by proper alignment. It also occurs when oil immersion objective lenses are used. The refractive index mismatch between the oil (or cover glass n = 1.52) and water (or biological sample n ≈ 1.33 - 1.47) [256] adds an additional curvature to the wavefront, which is directly transmitted to the back focal plane of the objective. All these aberrations are governed by Snell's law. This becomes especially important for deep tissue imaging (>~50μm).

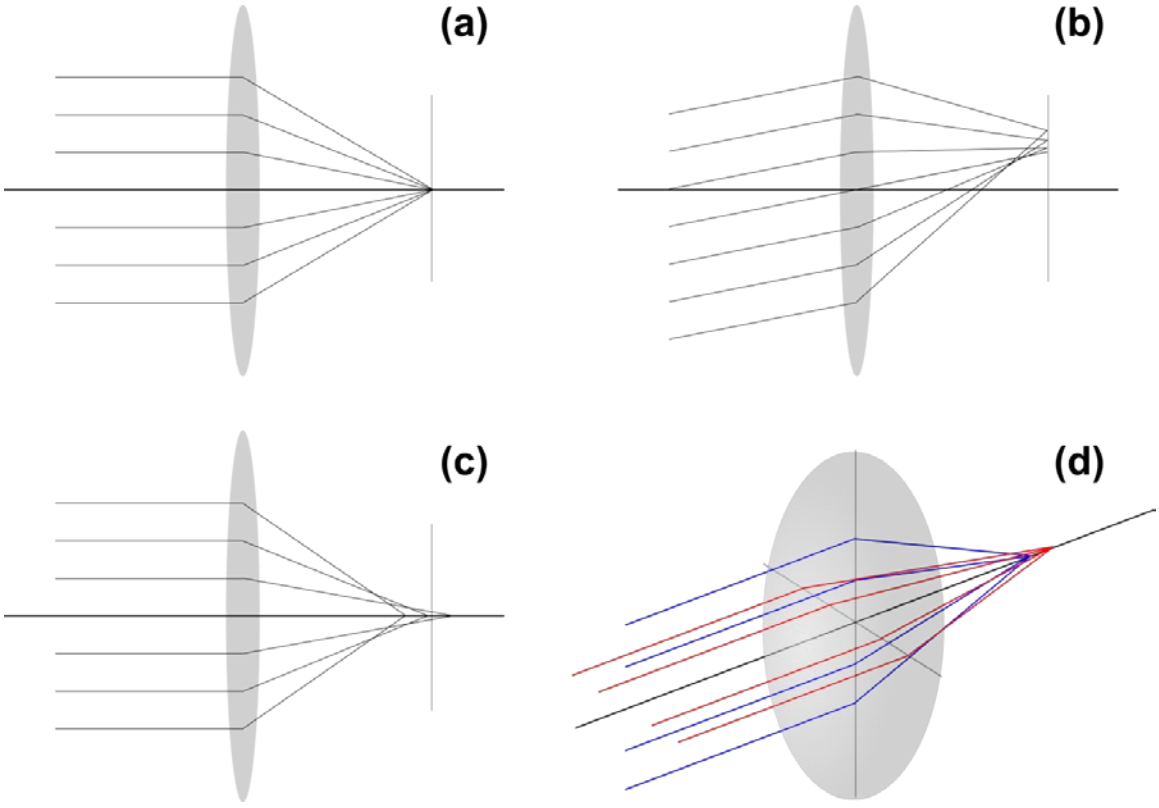

Figure 4-2 - Illustration of optical aberrations. (a) perfect focus, (b) Coma, (c) Spherical aberration, (d) Astigmatism.

4.1.1. Aberrations in biological samples

A biological sample can cause all the mentioned aberrations due to its geometrical shape, and the refractive index variations within the sample. Early attempts to characterize the deviation of the PSF from its actual position due to refractive index mismatches were done by simply using Snell's law [257-259], as shown in Figure 4-3. This analysis assumes only one refractive index interface, which causes axial shift of the focus and if the interface is tilted there would be lateral shift as well. Therefore the ratio between the actual and nominal focal points can be given by:

$$NFP = \frac{n_2}{n_1} AFP \tag{4.2}$$

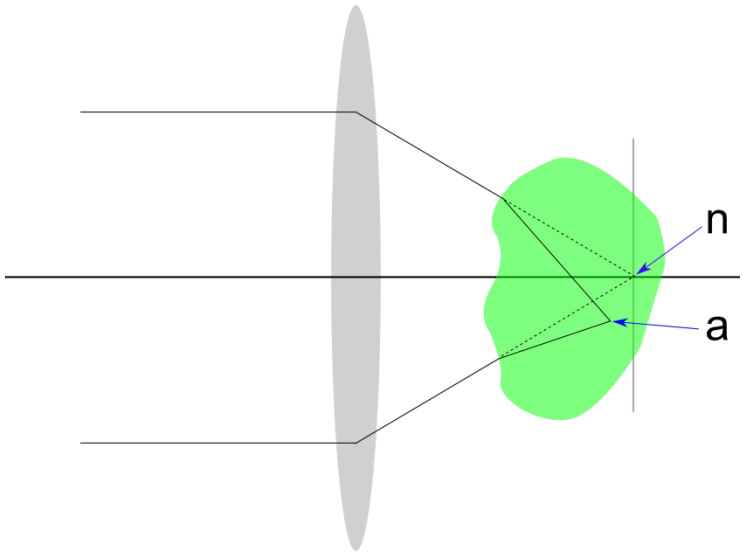

Figure 4-3 - Focus through an aberrating medium. Nominal focal point (n), and actual focal point (a) are shown.

The tomograms shown in Figure 4-1 however reveal more variations in the refractive indices of biological specimen. Even though the refractive index differences are small, they can have huge implications on the PSF. The biologically induced aberrations have been thoroughly analyzed and modelled in [121, 124, 260, 261]. To calculate an equation for an aberrated wavefront we should first find the phase of a plane which has travelled through the sample. The phase of point *L(x,y,z)* after passing through many layers of various indices of refraction $n(\tilde{x},\tilde{y},\tilde{z})$, can be determined by :

$$\phi\left(L\left(x,y,z\right)\right)=\int_{F}^{L(x,y,z)}\frac{2\pi}{\lambda}n\left(\tilde{x},\tilde{y},\tilde{z}\right)dw \tag{4.3}$$

where λ is wavelength of the beam in free space, *F* is the focal point, and *w* is the geometrical path light travels governed by Snell's law. The aberration of the wavefront from the ideal situation at plane z_0 can be written as

$$\Psi(x,y) = \int_{F}^{P(x,y,z_0)} \frac{2\pi}{\lambda}\left(n(\tilde{x},\tilde{y},\tilde{z}) - n_0(\tilde{x},\tilde{y},\tilde{z})\right)dw \tag{4.4}$$

where n_0 is the nominal refractive index of the propagating media without the aberrating media. To see the effect of the aberrating media on the PSF we can use the well-known equation relating the PSF to the pupil [262]:

$$h(u,v,\varphi) = \int_0^{2\pi}\int_0^1 P(r,\theta)\exp\left(j\frac{1}{2}ur^2 + jvr\cos(\theta-\varphi)\right)rdrd\theta \tag{4.5}$$

Now by substituting 4.4 into 4.1, and the combination into 4.5, the PSF becomes:

$$h(u,v,\varphi) = \int_0^{2\pi}\int_0^1 \exp\left(j\Psi(r,\theta)\right)\exp\left(j\frac{1}{2}ur^2 + jvr\cos(\theta-\varphi)\right)rdrd\theta \tag{4.6}$$

This effectively relates the variations of phase to the PSF. In a recent study by Braat et al. [263] effects of small and large aberrations on the PSF and OTF are explained.

4.1.2. Models of aberration

Optical aberrations in systems with a circular pupil are usually defined using Zernike polynomials [118, 264]. Zernike modes are a complete set of orthogonal polynomials defined on the unit circle, which can be used to describe and evaluate optical aberrations [265].

Other models of aberrations have also been developed, such as Lukosz [266], Braat [267], and Lukosz-Zernike [265]. They are used to reduce the error of wavefront aberration approximations for large wavefront errors.

Zernike polynomials are expressed by product of radial and azimuthal functions. They have three properties. First, they have rotational symmetry. Second, the radial

polynomial must be of degree of n, and should not have power less than m. And third the parity of the radial polynomial should match that of m. The polynomials are determined by:

$$Z_n^m(r,\theta)=\begin{cases} m<0: \sqrt{2}R_n^{-m}(r)\sin(-m\theta) \\ m=0: R_n^0 \\ m>0: \sqrt{2}R_n^m(r)\sin(m\theta) \end{cases} \tag{4.7}$$

where R is given by:

$$R_n^m=\sqrt{n+1}\sum_{s=0}^{(n-m)/2}\frac{(-1)^s(n-s)!}{s!\left((n+m)/2-s\right)!\left((n-m)/2-s\right)!}r^{n-2s} \tag{4.8}$$

In this dissertation we follow the notation of the Zernike modes from [264]. The equations and their notations are tabulated in Table 4-1. Illustration of up to third order Zernike polynomials are shown in Figure 4-4.

Table 4-1 - Table of Zernike polynomials.

n	m	No.	Equation	Description
0	0	0	1	Piston
1	1	1	$2r\cos\theta$	Tip
1	-1	2	$2r\sin\theta$	Tilt
2	0	3	$\sqrt{3}(2r^2-1)$	Defocus
2	2	4	$\sqrt{6}r^2\cos(2\theta)$	Astigmatism 90°
2	-2	5	$\sqrt{6}r^2\sin(2\theta)$	Astigmatism 45°
3	1	6	$2\sqrt{2}(3r^3-2r)\cos(\theta)$	Coma Vertical
3	-1	7	$2\sqrt{2}(3r^3-2r)\sin(\theta)$	Coma Horizontal
4	0	8	$\sqrt{5}(6r^4-6r^2+1)$	Spherical

3	3	9	$2\sqrt{2}r^3\cos(3\theta)$	Trefoil
3	-3	10	$2\sqrt{2}r^3\sin(3\theta)$	Trefoil
4	2	11	$\sqrt{10}(4r^4-3r^2)\cos(2\theta)$	2nd Astigmatism 90°
4	-2	12	$\sqrt{10}(4r^4-3r^2)\sin(2\theta)$	2nd Astigmatism 45°
5	1	13	$2\sqrt{3}(10r^5-12r^3+3r)\cos(\theta)$	2nd Coma Vertical
5	-1	14	$2\sqrt{3}(10r^5-12r^3+3r)\sin(\theta)$	2nd Coma Horizontal
5	0	15	$\sqrt{7}(10r^6-10r^4+12r^2-1)$	2nd Spherical

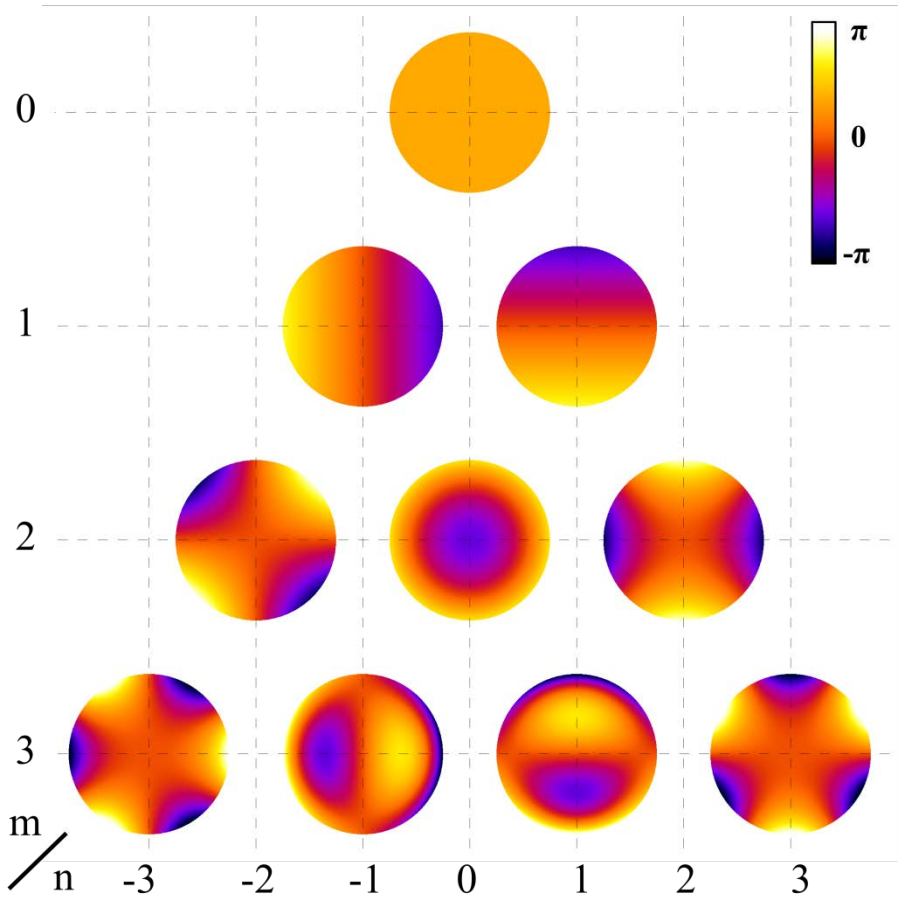

Figure 4-4 – Illustration of Zernike polynomials, Z_n^m.

Now if we have a known aberration, the coefficient of each mode can be determined by performing the following transform:

$$M_i = \frac{1}{\pi}\int_0^1\int_0^{2\pi} \Psi(r,\theta) Z_i(r,\theta) r d\theta dr \tag{4.9}$$

Likewise, a wavefront can be produced by superposing modes with known coefficient. This is mainly used for wavefront sensor-less sensing and correction.

$$\Psi_c(r,\theta) = \sum_i M_i Z_i \tag{4.10}$$

4.1.3. Strehl ratio

A measure of quality for an optical system is the Strehl ratio [262]. The Strehl ratio is the ratio between the intensity maxima of an aberrated and a perfect PSF. The Strehl ratio can be determined by [122]:

$$S = \frac{\left|\int_0^1\int_0^{2\pi} A(r,\theta)\exp\left(j\Psi(r,\theta)\right) r dr d\theta\right|^2}{\left(\int_0^1\int_0^{2\pi} A(r,\theta) r dr d\theta\right)^2} \tag{4.11}$$

Although this equation can be used for calculation of Strehl ratio, for faster estimation the following approximation can be used [116]:

$$S \approx 1 - \sigma_\Psi^2 \tag{4.12}$$

where σ_Ψ^2 is the variance of the wavefront. This is a very useful approximation; however, it can only be used for small aberrations (< 0.6 rad), since it becomes zero at 1 rad of wavefront error. Marechal's approximation uses a similar approach with lower error:

$$S'' \geq \left(1-\frac{1}{2}\sigma_{\Psi}^{2}\right)^{2} \tag{4.13}$$

In another study by Mahajan [268] another approximation is suggested for aberrations higher than 0.5 radians, for lower error:

$$S''' = \exp(-\sigma_{\Psi}^{2}) \tag{4.14}$$

4.2. Correcting elements

In this section we introduce the technologies most commonly used for compensation of wavefront error; Spatial light modulators, digital micro mirror device, and Deformable mirrors.

4.2.1. Spatial Light Modulators

A Spatial Light Modulator (SLM) is an array of pixels where each can modulate either the phase, or amplitude, or polarization of the incident beam. It can therefore be used to compensate for the distortions on the wavefront, by applying phase delays [269, 270]. SLMs are pixelated liquid crystal devices and are commonly used in the television industry. Liquid Crystals (LC) have characteristics between those of a liquid and a solid crystal, which gives them tunable optical properties such as birefringence. SLMs are either transmissive or reflective. The transmissive type uses liquid crystal technology and is called a LC-SLM [271]. While the reflective type employs liquid crystal on silicon technology and is called a LCOS-SLM [272]. Each pixel of a typical SLM consists of two polarizers, transparent electrodes, and the LC material. The two polarizers are placed in a perpendicular configuration to normally block light that is passed through the other one. The Molecular orientation of a twisted nematic aligned LC, which is the most commonly used type, is a helical structure. The electric field applied controls the

polarization deviation of the incident light. By applying appropriate voltage the polarization can change from 0° (completely blocked), to 90° (completely passed). Gray values can be made depending on the depth of modulation. Vertical and parallel nematic alignments can also be used with slightly different configuration. This configuration is suitable for Amplitude modulation, which requires linearly polarized incident light [273, 274].

For phase modulation, the second polarizer must be removed so that only a phase delay is applied. The twisted nematic alignment produces a change in the polarization, which is not desirable. Therefore for phase only modulation, a vertical or parallel nematic alignment is more suitable. Although SLMs can effectively apply phase differences, their slow speed (~ 100 Hz), wavelength dependent phase change and their sensitivity to the polarization of the incident wave, has made their application limited [119].

4.2.2. Digital Micro-mirror devices

Due to the slow speed of SLMs, digital micro-mirror devices (DMD) have been employed to speed up the process of correction. DMD technology is used in projectors, where an image is made by applying a binary pattern on an array of micro mirrors (pixels). Although in projection applications different shades of gray are produced by changing the on/off duty cycles of each pixel, for phase modulation a holographic technique called binary phase modulation [275] can be used. It has been used for correction of scattering media by passing parts of the beam with acceptable phase, and blocking the rest [276].

4.2.3. Deformable mirror

Deformable mirrors (DM) are optical elements with flexible reflecting surface. The shape of the surface of the mirror can therefore be modified to compensate for the wavefront error by adjusting the path length. Behind the reflecting surface of the DM, there are several actuators that can apply deformation to the reflected wavefront. Based on the spacing of the actuators (pitch) and their range of movement (stroke) they can be placed in two main categories of tweeter and woofer. Like in audio system where a tweeter produces high pitch sounds, and the woofer makes the low-pitch ones; higher order modes can be corrected by tweeter DM, and the low order ones by woofer. Two main types of DM exist, segmented, and continuous surface [277].

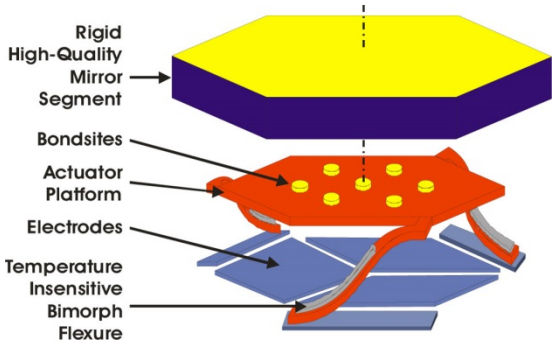

Figure 4-5 - Segmented piston/tip/tilt DM. (Credit: Iris AO)

There are two types of segmented DMs. The first segmented DMs could perform forward and backward motion (piston), where only one actuator is involved. Another type which emerged later is the DM that that each segment could perform piston, tip and tilt with 3 actuators involved in operation of each segment. Segments in this type are usually hexagonal, as shown in Figure 4-5. This type can produce shapes with less error than the piston type. The drawback is that the time consumption for calculation of each actuator for several thousand segments. Since the segments work independently of each other,

they can be used for correction of higher order aberrations, although it causes diffraction problem. The diffraction occurs since each segment acts as a slit.

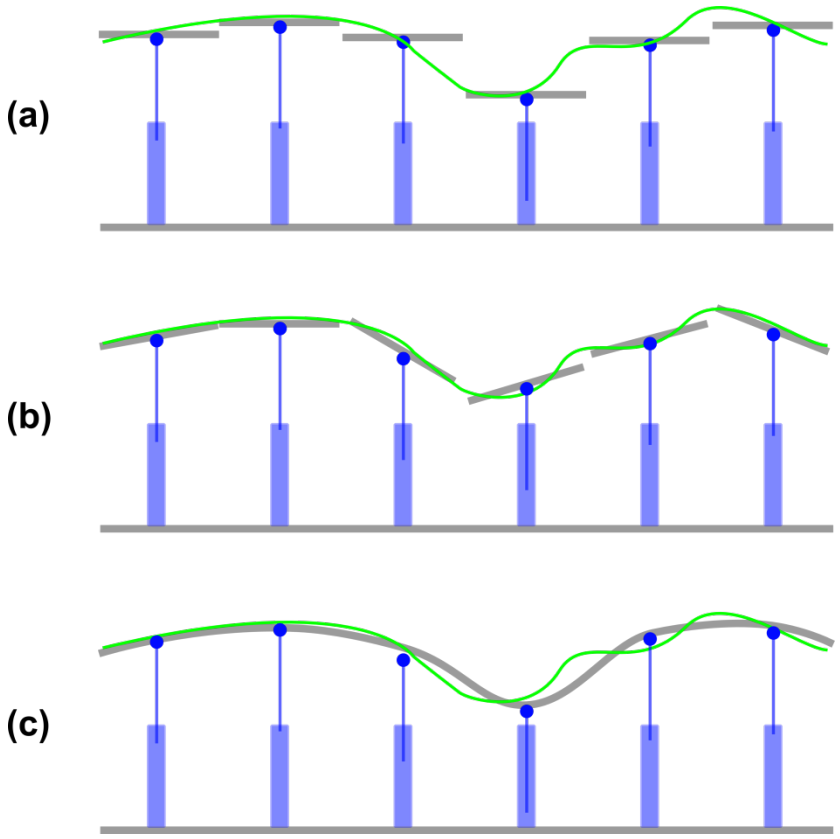

Figure 4-6 - Illustration of different types of DM, and their adaptability to low and high order shapes of wavefront. (a) piston only (b) piston, tip, and tilt (c) continuous surface. Green line represents the incident wavefront.

Different types of DM are shown in Figure 4-6. In addition to segmented DMs, there are continuous surface DMs. The actuators behind the surface control the shape of the mirror. Therefore the actuators cannot independently apply deviations to their part of the surface. For each actuator an influence function (or poke function in some literature) can be derived. The inner product of the influence function I and the actuators matrix A gives the phase:

$$\Psi_c = \bar{I} \cdot \bar{A} \tag{4.15}$$

This equation can be inversed to produce the actuator matrix, for a desired phase:

$$\bar{A} = \left(\bar{I}\right)^{-1} \Psi_c \tag{4.16}$$

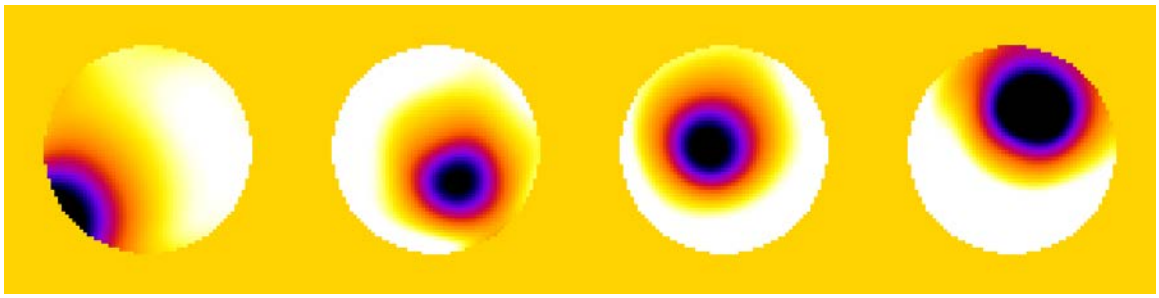

Figure 4-7 - Influence function of a few of the actuators poked, acquired by applying 0.02V to the actuator under investigation.

One may think that continuous surface DM provide the lowest error than the other types since they are not segmented and should possibly match the shape of the aberration perfectly, however because they are usually used for lower order aberration corrections, a segmented piston tip and tilt DM provides lower error for higher order correction. For astronomy purposes the fitting error is approximated for Kolmogorov atmospheric turbulence model. We reproduce it here for comparison of different DM types. The fitting error is given by [116]:

$$\sigma_F^2 = a_F \left(\frac{d}{r_0}\right)^{\frac{5}{3}} rad^2 \tag{4.17}$$

where r_0 is the coherence length - Fried parameter or “seeing cells size” - that defines the maximum diameter of a collector allowed before distortions limit its performance, a_F is the fitting error coefficient, *d* is the sub aperture size for the mirror, and *rad* the radius of the DM. Hardy AO book has evaluated the errors for each type, which we reproduced

here as Table 4-2. Using the fitting error the effect of DM as a high pass filter can be interpreted. It means that lower spatial frequencies are corrected to pass higher spatial frequency components. The spatial bandwitdth of the filter is given by $1/r_0$. The coefficient presented in Table 4-2 can be used to equate the number of segments N needed for each type to achieve the same amount of correction, using the following equation:

$$\frac{N_1}{N_2} = \left(\frac{a_{F1}}{a_{F2}} \right)^{\frac{6}{5}} \tag{4.18}$$

For example, comparing the continuous surface DM and piston only with circular segments, we see that $\left(1.07/0.28\right)^{6/5} = 5$ times more segments are required. We can also see that Piston/tip/tilt DM produces better accuracy. It has to be noted that these approximation are based on atmospheric turbulence models, and not directly applicable to biological aberrations.

Table 4-2- Fitting error coefficient for various types of DM. Source: [116]

DM type	Coefficient	Actuators per segments
Piston only (square segments)	1.26	1
Piston only (circular segments)	1.07	1
Piston/tip/tilt (square segments)	0.18	3
Piston/tip/tilt (circular segments)	0.14	3
Continuous surface	0.28	1

The actuators based on the application can be electromagnetic, piezo, or MEMS based. Their speed and hysteresis is a basis for selection of each type. Another type of

DM is bimorph, which uses two attached plates of piezoelectric wafers. By applying voltage to the combination, one contracts while the other expands, which causes curvature on the surface.

4.3. Correction strategy

The configuration of the AO system and the correction strategy will depend on the microscopy approach. Two-photon microscopy only requires correction of the excitation path so that the scanning excitation beam is focused as narrowly as possible. The emitted photons are all collected at a Photon-multiplier tube (PMT). Confocal and SIM techniques require wavefront correction on both the excitation and emission paths, since both are equally important in acquiring a sharp PSF. In widefield and SML imaging, only correction in the emission path is required because they illuminate a large field of view, and therefore the excitation path does not affect the emission PSF. Also in epi-fluorescence mode, since the excitation and emission use the same path, correction of the wavefront in the emission path automatically corrects the excitation path.

4.4. Wavefront measurement

In this section we introduce different types of wavefront measurement methods. We can put these methods into two main categories, direct and indirect. The former category involves using a sensor. Wavefront sensors were employed in astronomy as early as the 1950's. The Foucault Knife-edge test [114], and the shearing interferometer [278] were used to measure tip/tilt. The Shack-Hartman wavefront sensor (SHWS) [279], Pyramid [280], and curvature sensor [281], are some of the direct wavefront sensing methods used in astronomy. In microscopy the SHWS [282, 283] is used for many

modalities. In this section we introduce this method, as well as coherence-gated wavefront sensing [128], and the Pyramid wavefront sensor.

The latter category without the use of sensors, exploits spatial information acquired by images to measure the wavefront - with or without manipulation of the wavefront. Methods such as phase-retrieval, phase diversity, hill climbing, modal wavefront optimization, and machine learning algorithms are of this type.

4.4.1. Direct measurement

4.4.1.1. The Shack-Hartmann Wavefront Sensor

The Shack-Hartman wavefront sensor (SHWS) was R. Shack's improvement to the original aperture arrangement proposed by Hartman in 1900. The SHWS is the most common type of wavefront sensor used in microscopy [254]. It has been applied to widefield [282, 284], two-photon [127, 285, 286], confocal [287, 288], and light-sheet microscopy [289]. The SHWS uses an arrangement of micro-lenses as shown in Figure 4-8 to measure the gradient of the wavefront. The figure shows a flat wavefront as a green line. Each lenslets focusses a portion of the wavefront to a spot. When the wavefront gets aberrated, the position of each spot moves according to the gradient of the wavefront in the back pupil plane of the lens, in x,y plane. Knowing the position of the ideal PSF, and the deviated PSF we can reconstruct the wavefront.

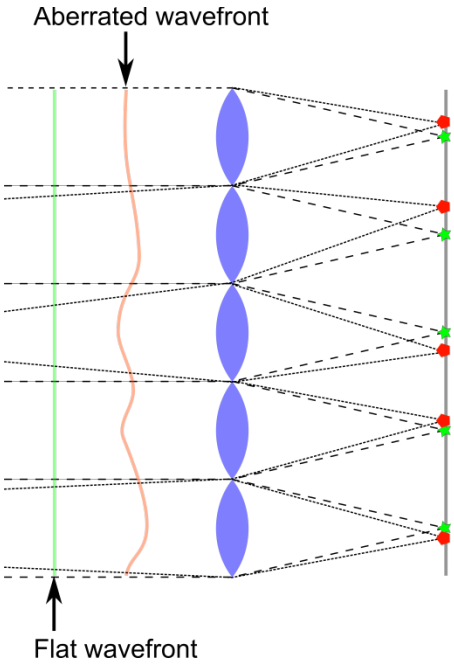

Figure 4-8 - Schematic operation of Shack-Hartman wavefron sensor. The green stars show the position of PSFs for ideal flat wavefront. The red pentagon show the location of PSFs made by aberrated wavefront. The displacement from the ideal flat wavefront correspond to the gradient of the wavefront.

A point source is required to make the flat wavefront at the back pupil plane of the SHWS. In astronomy, natural or synthetic guide stars (point sources at infinity) are used as the point source. In microscopy since natural guide stars do not exist, synthetic guide stars (SGS) have to be made. Synthetic guide stars have been made using auto-fluorescence [127] from the biological material, fluorescence from staining of sparse structures [288, 290], or micro-beads [284, 288, 291, 292].

Several methods have been used for reconstruction of the wavefront, such as least squares, Fourier based methods, and correlation approaches. The sensitivity of SHWS depends on the aperture size of the lenslets. However, a balance between the aperture size and the number of lenslets that fit in a back pupil plane has to be kept to avoid aliasing and still have the minimum error [293, 294].

4.4.1.2. Coherence gated wavefront sensing

In coherence-gated wavefront sensing (CGWS), an interferometric approach is employed to create a SHWS that redues the effect of out of focus light, to perform measurements deeper inside a sample. A low coherence length source is used in an interferometric phase-shifting arrangement [128, 295, 296]. A main problem with the traditional SHWS comes from the low NA of the lenslets which make it less sensitive to the depth variation of the aberrations, which is very important in microscopy. The CGWS takes advantage of interferometry to image the phase of the backscattered light. The depth dependent can therefore be adjusted by modification the reference arm. With the imaged phase, the wavefront can now be reconstructed using a virtual one [128, 297, 298].

4.4.1.3. Pyramid

The Pyramid wavefront sensor (PWS) uses the principle of the knife-edge test to produce the gradient of the wavefront [280]. The PWS uses a pyramid prism to produce four images with gradients in opposing directions and angles, as shown in Figure 4-9.

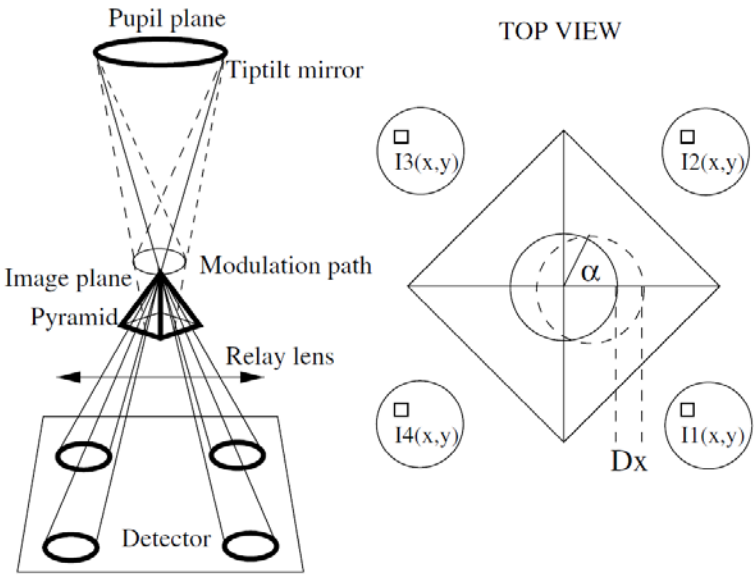

Figure 4-9 - Pyramid wavefront sensor. The wavefront is focused to the tip of a pyramid prism to make four gradient images. The images are then mixed to reconstruct the wavefront. Adapted from [280].

The images can be computationally mixed to reconstruct the wavefront. Compared to a SHWS, the PWS provides higher sensitivity and less susceptibility to aliasing [280, 299]. In contrast to the SHWS its sensitivity is not limited by the low NA of the lenslets or the number of apertures. In microscopy it has been applied for phase imaging [300], therefore it has a high potential to be applied to wavefront sensing for other modalities.

4.4.2. Indirect measurement

4.4.2.1. Phase retrieval

Phase retrieval is a wavefront sensorless –image based- technique that takes an iterative approach to minimize the error between an approximated wavefront and the actual one based on the measured 3D PSF [301-303]. An ideal complex pupil function is first assumed, and the PSF is calculated from it. The amplitude of the measured PSF then replaces the approximated PSF, although the phase function stays the same. Now an

inverse Fourier transform is applied. Using *a priori* knowledge of NA and wavelength, out of pupil components can be masked out to satisfy the constraints. The same procedure can be iterated to reduce the error to a satisfactory point. In our SML experiments without active AO, we have used this techniques, as described in [304] using fluorescent beads to correct the instrument's wavefront aberrations.

4.4.2.2. Phase diversity

Phase diversity is technique that exploits a known aberration applied to the system, to estimate the wavefront aberrations. Unlike the phase-retrieval technique, phase diversity can be used with extended (incoherent) images [305, 306]. The application of phase-diversity in 3D microscopy is discussed in [307].

4.4.2.3. Modal-based optimization

The two methods we just described apply known aberrations (defocus or otherwise), computational analysis of acquired images then produces the aberrated wavefront. The methods we present in this section and section 4.2.2.5 apply a known aberration and use image based metrics (that will be discussed in section 4.5) to evaluate the quality of the outcome. The phase of the applied aberration can be produced using equation 4.10. Several variations of model-based optimization are approached and applied to different modalities [308-313]. In general, images are acquired with a combination of several modes of an orthogonal model (Zernike or Lukosz) with different coefficients applied to the pupil. The images are evaluated using a metric to find the best coefficient of each mode. The choice of a suitable metric and the model are important in these methods to get the most spatial information without photo-bleaching of the sample.

A commonly used algorithm is Parabolic optimization [314] that approximates aberrations by measurement of the effect of applying three coefficients of a Zernike mode, and applying a parabolic fitting to it. This method requires a temporally constant object, so that the measurements are referenced correctly. The accuracy of this method can be affected with low SNR and temporally varying objects. This process is shown in Figure 4-10. The coefficients must be applied in reasonable intervals, to be able to find the center of the parabola.

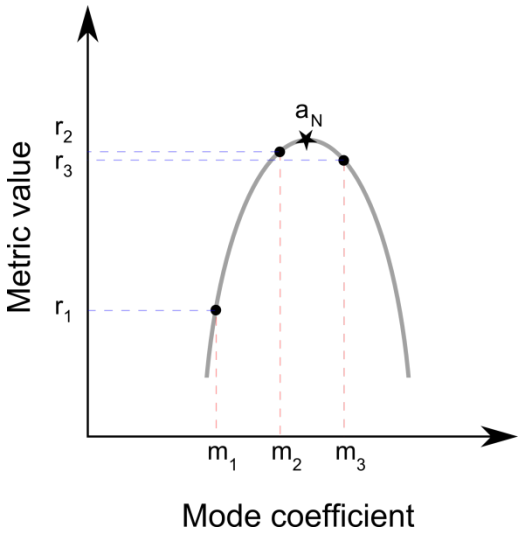

Figure 4-10 - Parabolic optimization approach. 3 measurements of aberration in reasonable intervals are performed. By applying a parabolic fitting the coefficient of the mode is defined.

4.4.2.4. Pupil segmentation

Pupil segmentation method measures the phase error by breaking down the pupil into several sub-regions. By illuminating only a sub-region of the back-pupil plane at a time, the deflection of the emitted fluorescence light from its supposed position when there is no aberration is measured. The acquired data is then used to reconstruct the whole wavefront. It has to be noted that Pupil segmentation does not use aberration models. This method is applied to two-photon [315, 316] and widefield [317] microscopy.

4.4.2.5. Machine learning methods

Most of the methods mentioned before require samples that are non-varying temporally, to be able to acquire enough information to measure the wavefront error. Machine learning algorithms such as Genetic algorithms or Particle Swarm Optimization (PSO) can break this limitation by techniques that make them prone to dynamic sample variations. Genetic Algorithms (GA) are well suited to both dynamic slowly varying aberrations and noisy measurements [318]. GAs have been used for AO correction in confocal and two-photon microscopy [319, 320], and for wavefront shaping to focus light through turbid media [318, 321]. A particular challenge in wavefront correction during SML imaging is the stochastic nature of the single molecule emission. Only a few fluorophores are emitting in any raw frame, and the number of photons emitted is highly variable, following exponential or Erlang statistics. This gives SML a dynamic characteristic that cannot be optimized with many of correction algorithms. In chapter 5 we present our implementation of a GA as well as PSO for optimization of aberration in thick samples.

4.5. Metrics for sensorless correction

An image-based metric is required as measure of the quality of the wavefront in many iterative wavefront correction schemes. Different features of an image are used, such as maximum intensity, total fluorescence intensity, image sharpness, and Fourier components; corresponding the imaging modality. In confocal and multiphoton microscopes, the total fluorescence intensity measured at a particular point is used [322, 323]. The mean image intensity has been used with two-photon microscopy [324]. In widefield microscopy, the maximum intensity of the image (or an image region) has been used as a metric [325]. Metrics based on the low-frequency spatial content of the image

and the image sharpness are also engaged in microscopy [130, 326, 327], which are again intensity dependent.

In another approach, sharpness metric was used. The sharpness metric high-pass filters the Fourier transform of an image, performs a summation, and normalizes by the total of the frequency components [133]. The metric S is defined by:

$$S = \frac{\sum_{n,m} \mu_{n,m} \tilde{I}_{n,m} \left(n^{'2} + m^{'2} \right)}{\sum_{n,m} \tilde{I}_{n,m}}$$
$$\mu_{n,m} = \begin{cases} 1 : \sqrt{n^{'2} + m^{'2}} \le \omega \\ 0 : \sqrt{n^{'2} + m^{'2}} > \omega \end{cases} \tag{4.19}$$

where $\tilde{I}$ is the Fourier transform of the image, with n and m coordinates, $n^{'} = n - \left(n_{total} - 1 \right) / 2$, $m^{'} = m - \left(m_{total} - 1 \right) / 2$, and ω is the radius of the threshold. This metric weights high frequency components the most, which are the parts with lower signal to noise ratio. Therefore the metric is vulnerable to noise.

For SML imaging however, the metric must be intensity independent due to fluctuations in the intensity of the blinking fluorophores. It must also be less prone to noise, because we are dealing with information from single blinking with typically limited number of photons. In chapter 5, we introduce a Fourier metric that exploits the high spatial frequency components, and to remove the intensity dependency normalizes it to the total fluorescence intensity.

4.6. Control system

An AO system can be configured as an open-loop or closed-loop control system. In open-loop approaches, the wavefront is measured once using direct or indirect

methods, corrected using the correction element, and for the rest of the imaging it is not measured again. The closed-loop approach is when the wavefront is measured constantly and the output is used to improve the error, or adapt to a changing environment such as dynamic aberration induced by in vivo sample. The closed-loop configuration was first implemented in microscopy using guide stars, either back scattered light [286] or fluorescent beacons [126, 292]. Sensorless AO can also work in a closed-loop system, and phase retrieval and modal-based approaches have been used [322, 328].

4.7. Conclusion

We described AO methods that were originally developed for astronomy, and their implementations in Microscopy. We showed that a wavefront can be severely aberrated by biological samples, as well as traditional sources of aberration such as imperfections in optical components and their misalignment. Correcting elements that are usually used for compensation of the aberrations were presented. Direct and indirect wavefront measurements were described, as well as metrics used for indirect measurements. In the next chapter we present our implementation of machine learning algorithms to wavefront correction for real-time SML data acquisition.

5. Implementation of AO for SML using machine learning algorithms[3,4]

In this chapter we present our implementation of machine learning algorithms to compensate for wavefront aberrations in real-time during SML imaging of thick specimens. The use of AO with SML has been reported in [131-133]. AO was used to correct for static system aberrations and to apply astigmatism for 3D SML but was not used for correction during STORM. Here we demonstrate that even in a relatively thin sample, imaging through the nucleus, AO-SML can improve the imaging. We further demonstrate AO-SML by imaging neuropeptides in the Drosophila brain through ~50µm of tissue. A particular challenge in wavefront correction during SML imaging is the stochastic nature of the single molecule emission. Only a few fluorophores are emitting in any raw frame, and the number of photons emitted is highly variable, following exponential or Erlang statistics. Therefore, many of the approaches that have been used in sensorless AO will be unsuccessful with raw SML images. Here we develop a novel Fourier based metric that is relatively independent of the intensity fluctuations. We successfully combine this metric with two machine learning methods, Genetic algorithms and Particle swarm optimization.

---

[3] Reproduced in part with permission from: K. F. Tehrani, J. Xu, Y. Zhang, P. Shen, and P. Kner, "Adaptive optics stochastic optical reconstruction microscopy (AO-STORM) using a genetic algorithm," Opt. Express **23**, 13677-13692 (2015).
http://dx.doi.org/10.1364/OE.23.013677

[4] Reproduced in part with permission from: K. F. Tehrani, J. Xu, and P. Kner, "Wavefront correction using machine learning methods for single molecule localization microscopy," (2015), pp. 93350L-93350L-93358. Copyright 2015 Society of Photo-Optical Instrumentation Engineers.
http://dx.doi.org/10.1117/12.2077269

Genetic Algorithms (GA) are well suited to both dynamic slowly varying aberrations and noisy measurements [318]. GAs have been used for AO correction in confocal and two-photon microscopy [319, 320], and for wavefront shaping to focus light through turbid media [276, 318]. GAs work on an evolutionary scheme. A population of random wavefronts is generated and then evaluated. In each transition to the next generation, the population is bred and mutated and then re-evaluated. By keeping the improved wavefronts in the population, GAs converge to a final wavefront with the best performance after several iterations. Because the wavefront is varied in a random dynamic manner, and not incrementally, GAs are well suited to dynamic and noisy conditions.

Particle Swarm Optimization (PSO) is from a family of Swarm algorithms with roots in the ‘collective intelligence’. When a large number of homogeneous agents in an environment join together to solve a problem, it is a form of collective intelligence. The algorithms are used in nature by groups of animals to solve problems such as foraging for food. Swarm intelligence is also an adaptive strategy, as are evolutionary algorithms, and therefore can be applied to the problem of dynamic aberrations induced by biological samples [329, 330].

We first present simulations of SML to show the effect of aberrations on the resolution of SML. We then discuss the metric. This is followed by a section on GA, including an explanation of the algorithm, simulations and experimental results. A similar section on PSO comes afterwards. In each of these two sections we demonstrate wavefront correction in different systems: the system aberrations, a round worm, a thin

cell, and the Central Nervous System of a *Drosophila* embryo. And finally we discuss the effect of aberrations on resolution, and give our discussion.

5.1. Simulations of SML with aberrations

To illustrate the effects of aberrations and to test and optimize our algorithms, we developed a simulation of SML imaging. A wavefront was generated from an array of N_Z Zernike modes, with the amplitude of each Zernike selected from a Gaussian distribution with standard deviation, $a = w / N_Z^{1/2}$ where *w* is the average root mean square wavefront error. The back pupil plane wavefront corresponding to the emission from a single fluorophore at the origin is then generated, with the radius of the wavefront determined by the numerical aperture and the phase of the wavefront calculated from the sum of the Zernike modes corresponding to the aberration. The intensity of the fluorophore's emission was determined from an exponential distribution with an average value corresponding to the average number of photons generated by the fluorophores. An image of each fluorophore is generated by scaling the wavefront by the square root of the intensity, and then multiplying the wavefront by a phase term $\exp\left(2\pi j\left(px+qy\right)\right)$, to place the center of emission at the position, (x,y), of the fluorophore (using the Fourier Shift Theorem) where p and q are the Fourier transform coordinates, corresponding to the position in the back pupil plane.

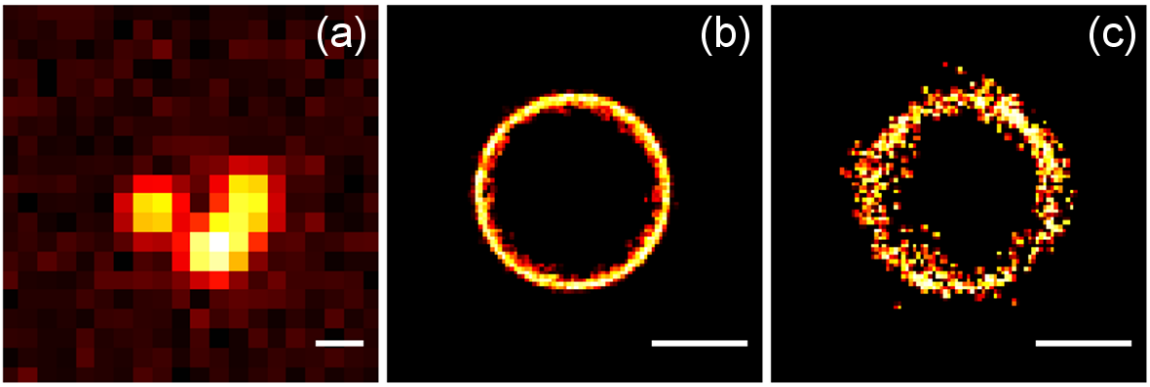

Figure 5-1 – Simulations of SML with the Genetic Algorithm. A SML dataset was generated without aberration. One raw frame is shown in (a), and the reconstructed image is shown in (b). 1824 points were localized. (c) Reconstruction of a SML dataset with 0.8 radians rms wavefront error. 941 points were localized with lower accuracy than the previous case. Scale bars are 250nm.

The wavefront aberration was generated from the first 15 Zernike modes. To test the effect of aberrations, we generated two SML datasets of a circle with a radius of 250nm consisting of 2000 raw frames. 1000 particles were placed on the circle, and, in each frame, a subset of them determined by a Poisson distribution with mean 3, were emitting photons. No aberration was applied to the first dataset (a single raw frame is shown in Figure 5-1(a)). However, a 0.8 radian RMS wavefront error was applied to the second dataset. As can be seen in the reconstructed images from the two datasets, shown in Figure 5-1 (b-c) respectively, the reconstructed image without aberrations shows a uniformly distributed circle, whereas the second dataset shows lower accuracy of localization. The degradation of the PSF also affects the number of localizations; without aberrations, 1824 points were localized, whereas only 941 points could be identified from the aberrated dataset. We also performed Fourier Ring Correlation (FRC) [217, 331] analysis (as explained in section 2.5.3) on the image stacks with and without aberrations. The resolution with no aberration applied was 19.55 nm, whereas with 0.8 radian aberration applied the resolution was 118.06 nm, which shows a considerable disparity in

the localization accuracy. We further tested the effect of a known aberration on the resolution by performing FRC on simulations with different amounts of defocus with all other aberrations set to zero. The results are shown in Figure 5-2. Figure 5-2 (g) shows that the resolution is reduced by a factor of 3 by applying 1.2 radians of defocus.

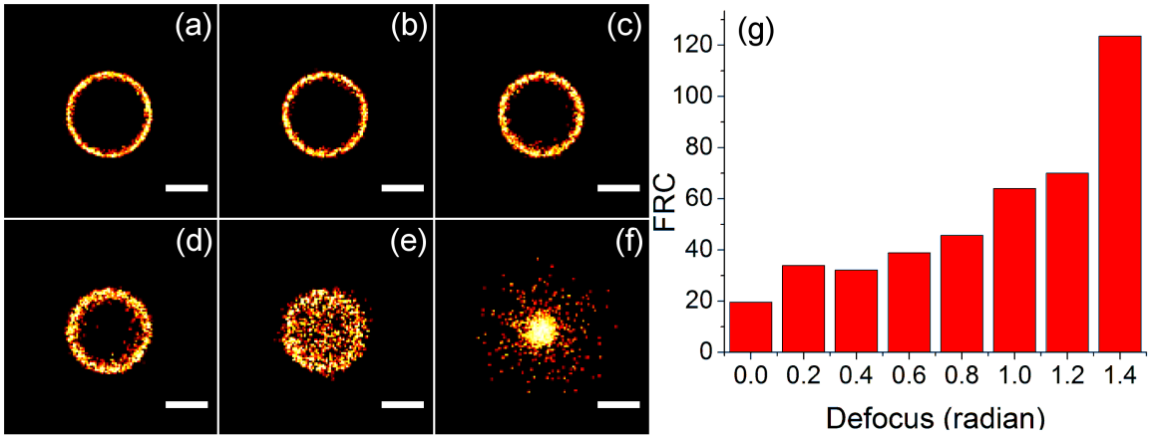

Figure 5-2 -- Simulations of the effect of defocus on the resolution. (a-f) show reconstructions of simulated stacks with 0.2, 0.6, 0.8, 1.0, 1.2, and 1.4 radian rms wavefront error respectively. (g) plot of the resolution of each simulation calculated using Fourier ring correlation analysis. Scale bars are 250nm.

5.2. Merit function

Many iterative wavefront correction schemes use metrics related to the intensity. In confocal and multiphoton microscopes, the total fluorescence intensity measured at a particular point is used [322, 323]. The mean image intensity has been used with two-photon microscopy [324]. In widefield microscopy, the maximum intensity of the image (or an image region) has been used as a metric [325]. Metrics based on the low-frequency spatial content of the image and the image sharpness are also intensity dependent [130, 326, 327].

However in real time wavefront correction for SML imaging an intensity independent metric is needed due to the large fluctuations in the intensity of single blinking fluorophores. Figure 5-3(a) shows the maximum intensity of a wavefront corrected Quantum Dot (QD) blueing SML dataset [332]. As can be seen in the figure, due to blueing, the average intensity of the fluorophores increases first, and then starts to decrease. Similarly a dataset with blinking Alexa 647 dyes in SML imaging buffer (MEA) is shown in Figure 5-3 (b), where the intensity of individual images fluctuates with $\sigma/\mu \sim 0.19$. The corresponding histograms are shown in Figure 5-3 (c-d), which show that the fluorophore photon counts follow exponential distributions (an exponential curve fit is shown). For an exponential distribution, $\sigma/\mu=1$. Hence an intensity independent algorithm is essential for wavefront correction in real time SML imaging.

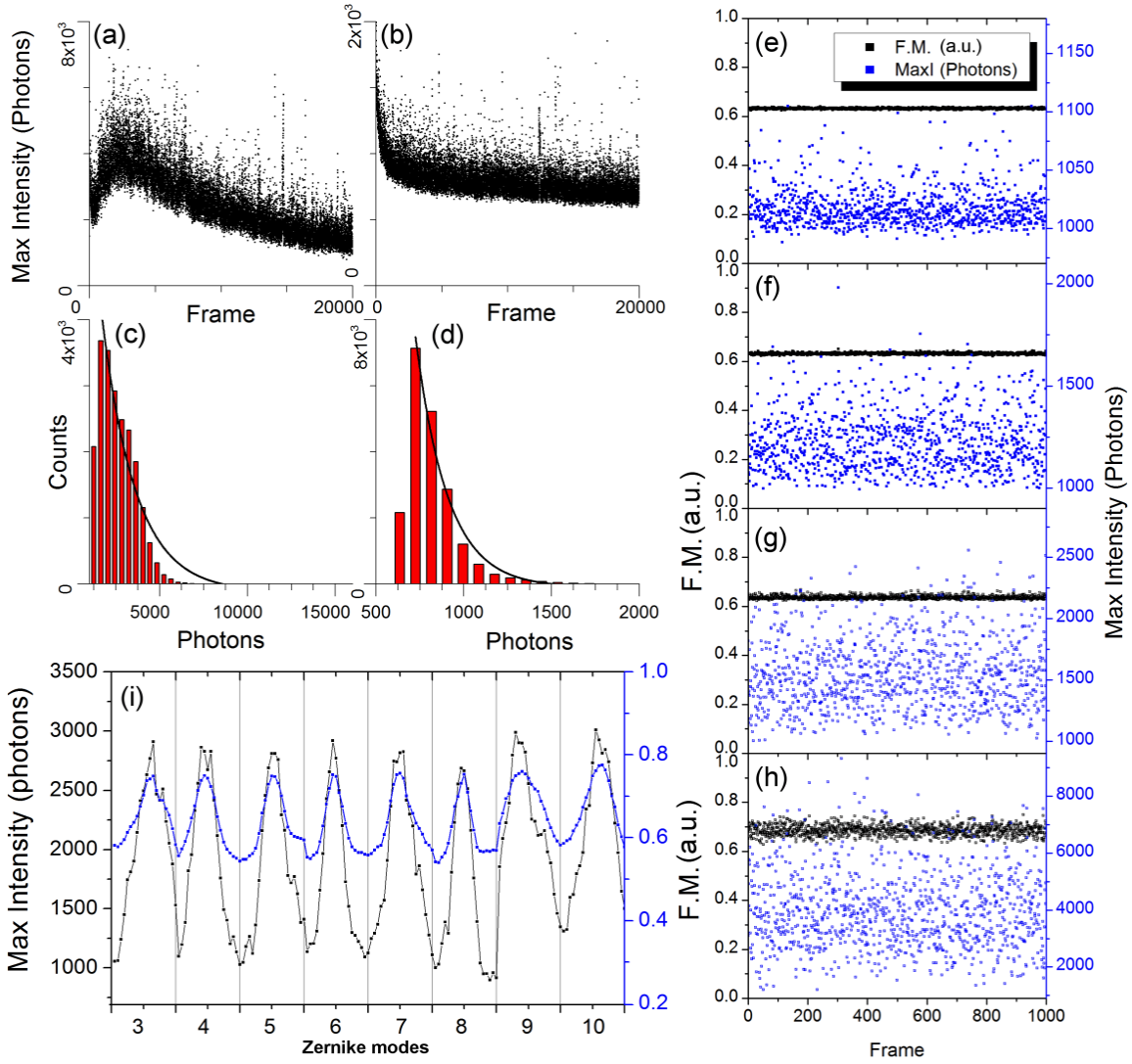

Figure 5-3 - (a-b) Maximum intensity of SML data sets with corrected wavefront using Quantum Dot blueing and Alexa dye blinking respectively, with their corresponding histograms shown in (c-d). Simulations of 10 blinking molecules on a circle for 1000 frames. The average intensity of each molecule follows an exponential distribution. The value of the FM metric (arbitrary unit a.u.) and maximum intensity (photons) for each frame are shown in (e-h) for average photon counts of 100, 500, 1000, 5000 respectively. (i) In each frame a Zernike mode amplitude is varied from –10 to 10 radians, and the maximum image intensity (left axis, black) and the FM (right axis, blue) are measured. (The Zernike modes correspond to the following aberrations: 3 – defocus; 4, 5 – astigmatism; 6, 7 – coma; 8 – spherical aberration; 9, 10 – trefoil.)

We propose a spatial frequency based metric in which the high frequency content of the image is normalized by the total intensity. The metric, FM, is defined as

$$FM = \frac{\sum_{\mu,\nu}\left(1-G(\mu,\nu)\right)\left|I(\mu,\nu)\right|\mathrm{circ}\left(\frac{\lambda}{2NA}\sqrt{\mu^2+\nu^2}\right)}{\sum_{\mu,\nu}\left|I(\mu,\nu)\right|\mathrm{circ}\left(\frac{\lambda}{2NA}\sqrt{\mu^2+\nu^2}\right)} \tag{5.1}$$

where $I(\mu,\nu)$ is the Fourier Transform of the image, $I(x,y)$, and circ() is the circle function [333]. $G(\mu,\nu)$ is the Gaussian function,

$$\mathrm{G}(\mu,\nu) = \exp\left(-\frac{\mu^2+\nu^2}{2\sigma^2}\right) \tag{5.2}$$

where σ is the standard deviation of the Gaussian distribution. The standard deviation of the Gaussian function is set to 0.4 μm^{-1} which was determined empirically to block out the low frequencies containing background fluorescence. We refer to the metric as the Fourier Metric (FM). The FM measures the high frequency content of the image normalized by the total intensity. A flat wavefront increases the high-frequency response of the OTF, so the FM value will increase as the wavefront is improved. The metric is different than other approaches such as the sharpness metric [133]. The FM uses a high-pass filter so that the higher spatial frequencies are weighted roughly equally whereas the sharpness metric weights the highest spatial frequencies the most, and these are the frequencies where the optical transfer function is the weakest. This helps the algorithm guide its way to the optimum wavefront.

The metric was tested using a series of simulations on blinking fluorophores with exponential intensity distributions and no wavefront aberration. Results from simulations on a set of blinking fluorophores in a circle with average photon counts of 100, 500, 1000, and 5000 are shown in Figure 5-3 (e-h). A background of 1000 photons/pixel is

added and Poisson noise is added to the entire image. With the background, the metric ranges from a low of about 0.2 to about 0.7.

The normalized standard deviations of the maximum intensities are 0.017, 0.12, 0.18, and 0.33. The normalized standard deviations of the Fourier Metric are 0.004, 0.005, 0.011, 0.031, which is about a factor of 10 lower than the deviation of the maximum intensity. We further tested the metric on a single intensity invariant 100nm fluorescent microsphere. Zernike mode amplitudes were scanned from -10 to 10 radians, and the maximum intensity of the fluorescent microsphere image was compared to the Fourier Metric demonstrating that the FM is peaked at zero wavefront aberration.

5.3. Genetic Algorithm

Genetic Algorithms are methods of machine learning that use an evolutionary approach to solve optimization problems that are not easily solved analytically. Aberrations in biological samples can have a dynamic characteristic and can be difficult to characterize due to weak signals. Furthermore, for aberrations larger than a few radians, the optimization problem is nonlinear [322]. Therefore, GAs are a suitable solution for minimizing the wavefront error.

Genetic algorithms can be applied to systems which have four criteria for evolutionary systems: the ability to reproduce, e.g. having genes, a population of individuals, variety among the population and differences in fitness. To apply GAs to wavefront optimization, we expand the wavefront in the Zernike basis. (We use the root mean square (RMS) normalized Zernike modes with the ordering from [334].) The genes of the algorithm are the coefficients of the expansion, and an individual is a specific wavefront with a specific set of Zernike coefficients. A population is generated from a

random distribution of Zernike coefficients over a prescribed range and successive generations of wavefronts are generated by mixing the genes of individuals in the previous generation. The fitness of each wavefront is evaluated using an image quality metric so that the wavefronts that improve the correction are preferentially selected for generating the next generation. In this way, the wavefront optimization problem satisfies the criteria for a GA [335].

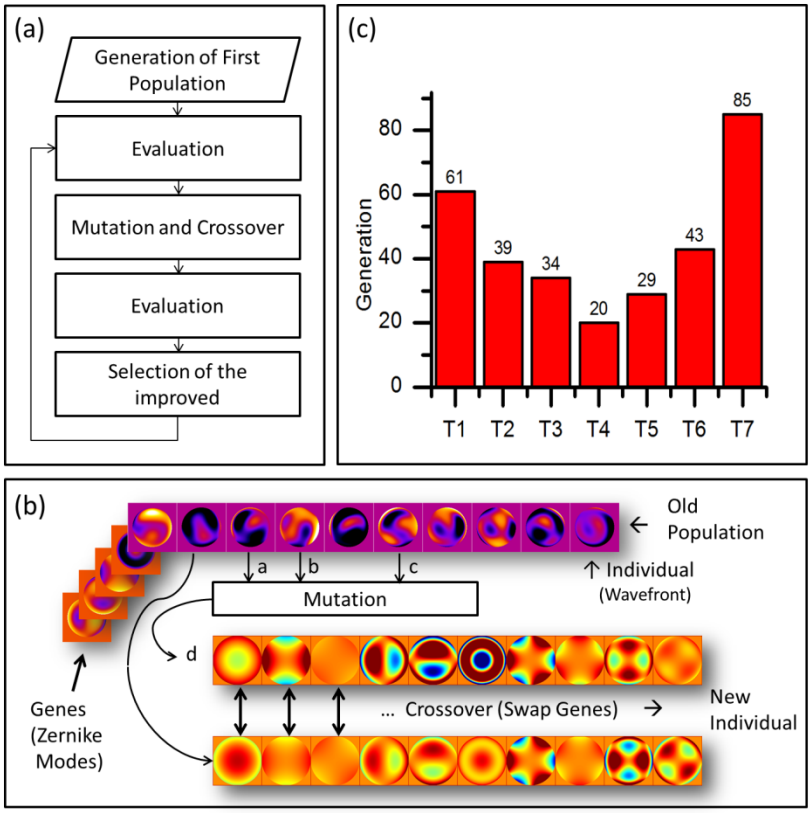

Figure 5-4 - (a) Block diagram of the Genetic Algorithm. Different values of mutation and cross over ratios affect the number of generations the algorithm requires to converge to an optimized steady state. (b) Graphical presentation of the Genetic algorithm. Several Zernike modes (genes) comprise an individual wavefront. A population of individual wavefronts is generated and evaluated. A new generation is then generated through the mutation and crossover processes. (c) Bar graph shows the generation number when the algorithm has converged to 90% of its final value for different settings. In T1 to T4, the mutation ratio is kept constant at 0.1 and the cross over ratio is increased from 0.2 to 0.8. In T5-T7, the cross over ratio is kept constant at 0.8, and the mutation ratio is increased from 0.2 to 0.6.

As shown in Figure 5-4 (a), the algorithm starts by generating *N* wavefronts with random Zernike coefficients. The random coefficients have a uniform distribution over a pre-determined amplitude range. The number *N* is determined by the number of Zernike modes used to describe the wavefront. N should be large enough to provide variety among the population, and small enough not to slow down the algorithm by requiring too many measurements. A smaller value of N increases the chance that the algorithm fails to converge. We used a robust value of 10 times the number of Zernike modes for N. After the initial population is generated, each individual wavefront is evaluated using the metric and a fitness value is assigned to each wavefront. Then a new generation is created by the mutation and crossover of the individuals from the previous generation. This algorithm we use is known as a non-dominated sorting genetic algorithm [336]. The mutation process randomly selects three individuals *a*, *b*, *c*, each represented by their coefficient vectors, and generates a new individual *d*, using polynomial mutation [337]:

$$d = a + mtr \times (b - c) \tag{5.3}$$

where *mtr* is the mutation ratio. The crossover process is then applied between each individual in the population, *a*, and the new mutated individual *d*, in which the genes — the Zernike coefficients — of the mating individuals are exchanged with a probability determined by the crossover ratio *cxr*. The two processes are applied to each individual, *a*, to create the new generation. The new generation is now evaluated, and the fitness value of each new individual *d*, is compared to the fitness of its parent, *a*. Only individuals with improved fitness will pass on to the next generation, otherwise the previous individual passes on to the next generation. This process is illustrated in Figure 5-4 (b).

We optimized the values of *mtr* and *cxr* for fastest convergence of the algorithm through a series of simulations. We found that with a crossover ratio of 0.8 and a mutation ratio of 0.1 the algorithm reaches 90% of its steady state value in less than 20 generations, as shown in Figure 5-4 (c). With mutation ratio values higher than 0.5 the system can become unstable since the coefficients of the individual *d* can be considerably larger than the original coefficients. We also found that the mutation value should be variable to avoid large fluctuations of the wavefront as the algorithm converges to the optimum. This is particularly important in real time correction and imaging, since we would like a lower variation of the wavefront when the Strehl ratio is high. We define the *mtr* as a function of the standard deviations of fitness values of the previous generations using the following equation:

$$mtr_n = \frac{mtr_{\max}}{1+\exp\left(-C\left[t_n - t_c\right]\right)} \tag{5.4}$$

where t_c is a threshold to keep the value of *mtr* low, and t_n is the slope of the decay of the previous generations standard deviation. t_n is calculated by linear regression over the past *m* generations, using the following formula:

$$t_n = \frac{\sum_{i=n-m}^{n-1}\left(g_i - \frac{1}{m}\sum_{j=n-m}^{n-1} g_j\right)\left(y_i - \frac{1}{m}\sum_{j=n-m}^{n-1} y_j\right)}{\sum_{i=n-m}^{n-1}\left(g_i - \frac{1}{m}\sum_{j=n-m}^{n-1} g_j\right)} \tag{5.5}$$

g_i is the generation number and y_i is the corresponding standard deviation value. We chose the maximum *mtr* to be 0.2 so that mtr_n stays within an optimum region. *C* defines the slope of the the quasi-linear region at the center of the sigmoid function. A typical value for *C* is 50 to provide enough sensitivity for the *mtr*.

5.3.1. Simulation of GA-AO correction for SML

We continued by simulating the correction of wavefront aberrations using our Genetic Algorithm during the acquisition of a SML dataset. The implementation of the genetic algorithm we use is the open-source Python package, DEAP [338]. For the simulated object, 1000 fluorophores were placed on a circle with a 0.25μm radius. A random aberration, consisting of the 12 Zernike modes from 3 to 15, was applied to the wavefront. The amplitude of each mode was generated from a uniform distribution. The GA was run over the first 5400 frames to reach 90% of its optimized steady state. For each raw frame, a number of emitting fluorophores was generated from a Poisson distribution with mean 10. Then this number of fluorophores was randomly selected from the list of fluorophores in the simulated object. The simulated PSF of each emitting fluorophore was generated from the wavefront consisting of the initial wavefront aberration and the wavefront applied by the GA. The intensity of each PSF was selected from a Gamma distribution with shape factor k=2.5. Gamma distribution was applied because we were able to fit the intensity histogram of the dyes with it. The very first frame without correction is shown in Figure 5-5 (b). After about 45 generations the algorithm converges to a well-corrected steady state, Figure 5-5 (c & d). In the last 10,000 frames, the relative fluctuation, σ/μ, of each Zernike mode coefficient was less than 1%. The rms wavefront error has improved from the 2.18 radian initial wavefront error to 0.27 radian after correction, which corresponds to a 0.93 strehl ratio.

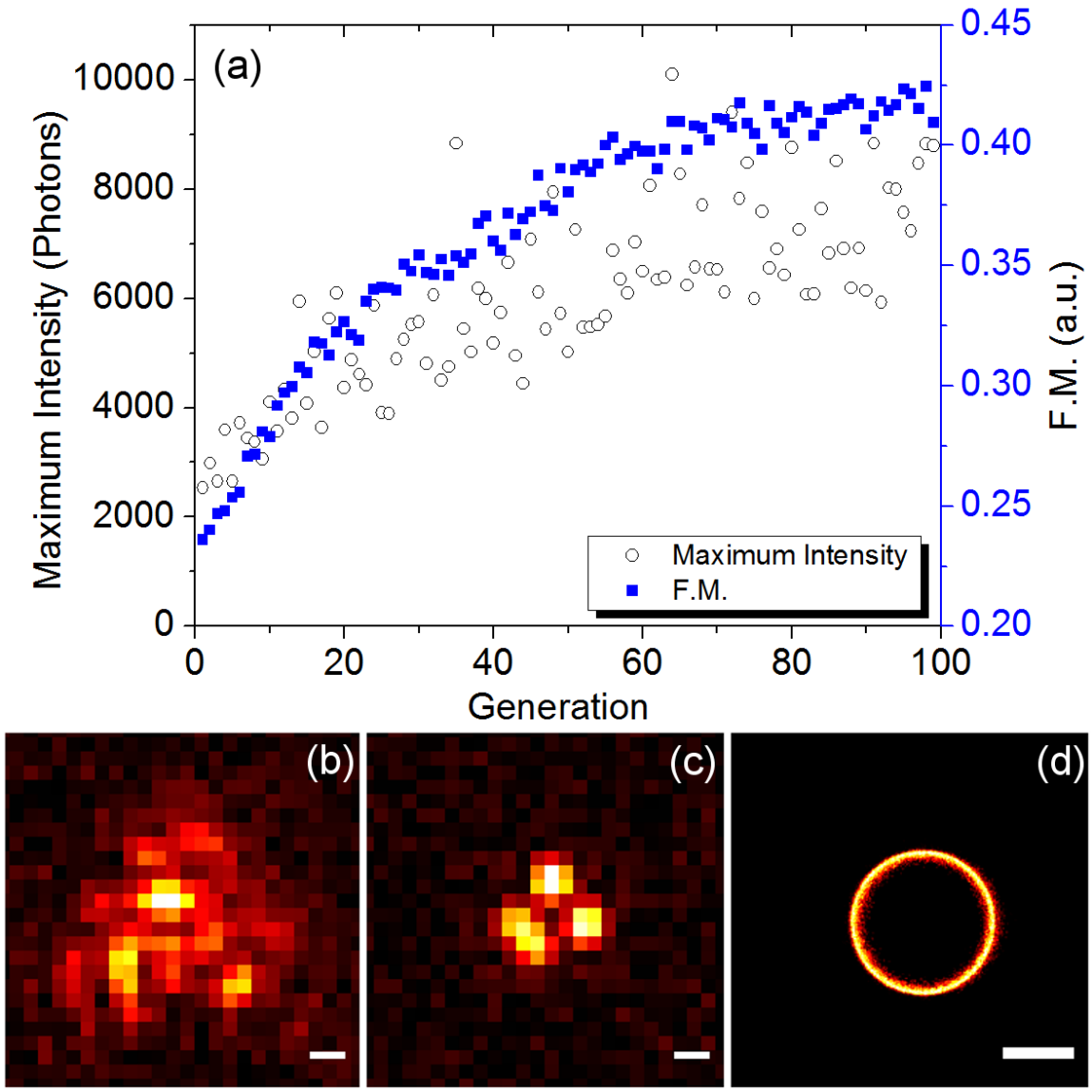

Figure 5-5 – Simulation of AO-correction using Genetic Algorithm for SML. The GA was applied to a SML simulation with a random induced aberration consisting of Zernike modes 3 to 15 with an RMS wavefront aberration of 0.9. A graph of the FM (arbitrary units, a.u.) and Maximum Intensity (photons) versus Generation is shown in (a). (b) The first frame of the dataset without correction. (c) A corrected frame from the 50th generation. (d) The reconstructed image from the last 10,000 frames (after convergence). Scale bars are 250nm.

5.3.2. Experimental result of GA-AO-SML correction for SML

First we tested GA-AO-SML on a single fluorescent microsphere on the coverslip and then fluorescent microspheres under a *C. elegans* roundworm. Next we applied GA-

AO-SML to imaging of microtubules through the nucleus of a hepG2 cell and imaging of neuropeptides inside a single neuron in a *Drosophila* (fruit fly) brain lobe.

5.3.2.1. System Aberrations

First we applied the algorithm to the problem of "flattening" the deformable mirror (DM) and correcting system aberrations. When all the DM actuators are set to a 0V actuation voltage, the mirror surface is not flat and will cause significant aberrations. To determine the DM settings that would flatten the mirror and correct system aberrations, we applied the GA-AO-SML algorithm to a sub-diffraction fluorescent microsphere attached to a coverslip at the focal plane of the objective lens. In Figure 5-6 (a) the initial PSF with an uncorrected deformable mirror can be seen. The Genetic Algorithm converged in about 20 generations to the desired PSF as shown in Figure 5-6 (b). The removed aberrations, shown in Figure 5-6 (c), represent the aberrations from the DM and the instrument. A small defocus is due to the microsphere being not exactly at the focal plane. We also performed Phase retrieval analysis (section 4.4.2.1) before and after the GA correction. The Strehl ratio had an improvement from 0.59 before the correction to 0.81 after.

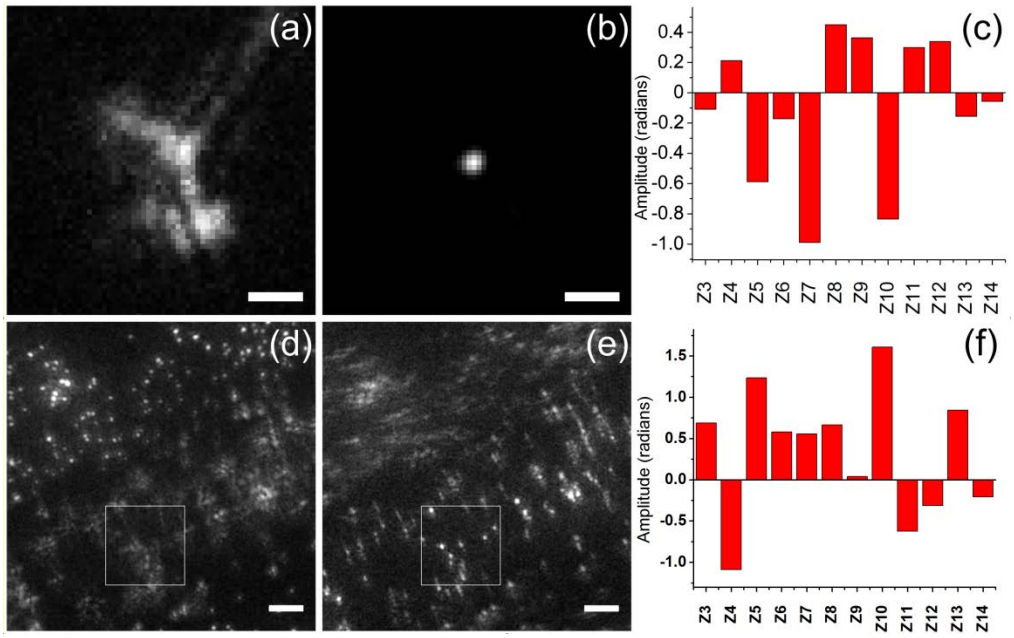

Figure 5-6 - (a-c) Genetic Algorithm corrects aberrations induced by the optical components. PSF of a 200nm fluorescent microsphere is shown before and after correction in (a) and (b) respectively. The bar diagram of corrected Zernike modes is shown in (c). The scale bars are 1µm. (d-f) Aberrations induced by C. elegans worm. Images of before and after correction, and the bar diagram of corrected Zernike modes are shown in (d),(e), and (f) respectively. Scale bars are 5µm.

We compare our GA correction with parabolic optimization [314]. We performed 10 point measurement on a search space from $-\pi$ to π radians, on 12 Zernike modes (3 to 15). The coefficient of each mode was found using parabolic fitting. This process was iterated 5 times to find the optimum wavefront. The Strehl ratio was improved from the initial 0.59 to 0.75 after the correction.

5.3.2.2. Correction of aberrations induced by a roundworm

We further tested the algorithm by inducing aberrations using a *C. elegans* roundworm which has a roughly cylindrical cross-section. Due to the shape of the worm, the main aberrations induced are defocus, astigmatism and coma. Figure 5-6 (d) shows an initial image of fluorescent microspheres imaged through the worm with the wavefront corrected for the system aberrations. The box in the image shows the Region Of Interest

(ROI) used to calculate the FM. In less than 30 generations the GA converges to 80% of its optimum, and we can see the resulting image in Figure 5-6 (e), where the PSFs under the worm are corrected but the ones outside of the worm are now aberrated. This correction was again started with all DM actuators set to 0V. Figure 5-6 (f) shows the difference in the correction due to the worm; we have subtracted the corrections required to flatten the mirror. Figure 5-6 (f) demonstrates that the sample induced a large defocus, and, due to the almost diagonal orientation of the worm, both horizontal and vertical astigmatism.

5.3.2.3. Real time wavefront correction of SML on a thin cell

We imaged microtubules stained with 565nm Qdots in hepG2 cells. hepG2 cells are thin tissue culture cells (under 10µm). Although the whole cell can be imaged with SML [236], the nucleus of the cell induces defocus and astigmatism. Figure 5-7(a) shows a widefield image. The ROI in Figure 5-7(a) indicates the region under the nucleus where AO-SML imaging was performed. As can be seen in the image, the area is not very clear, and the microtubules on the opposing side of the nucleus are not resolved. The resulting SML image can be seen Figure 5-7(b). The corrected Zernike coefficients are presented in Figure 5-7 (c). 0.3 radians of Z3 corresponds to less than 100nm of defocus. A total wavefront aberration of 0.39 radians RMS was removed. Assuming a 0.85 Strehl ratio after correction which is typical of our system, this would correspond to a 0.53 Strehl ratio before correction, calculated using the Marechal approximation [339].

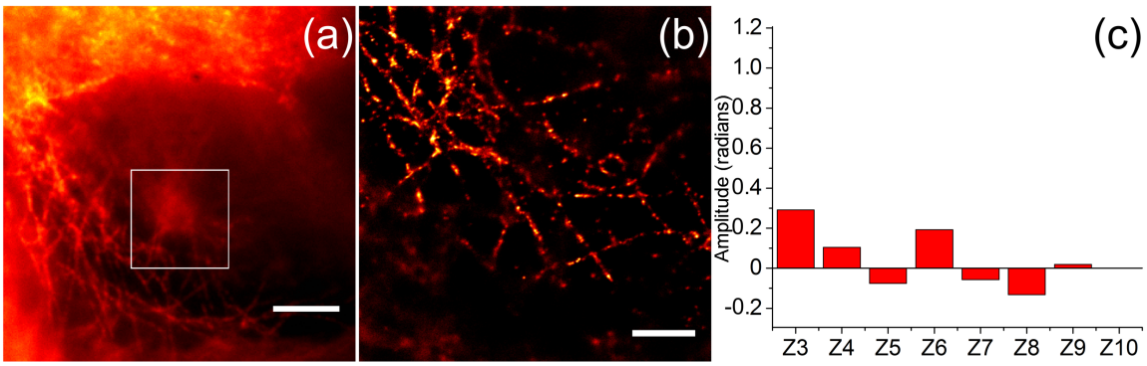

Figure 5-7 - Real time wavefront correction using AO-SML on the microtubules under the nucleus of a hepG2 cell. (a) widefield image (b) SML image reconstructed from the frames after the algorithm reached an optimized steady state (c) Bar diagram of the aberrations removed. Scalebars are (a) 5µm, (b) 2µm.

5.3.2.4. Real time wavefront correction of SML on a thick tissue

Recognition and measurement of neurotransmitters is a subject of interest in neuroscience. Considered as a good model system, the *Drosophila* larval CNS is simpler, but contains most neurotransmitters found in mammalian systems. These neurotransmitters regulate important biological processes in a similar manner to their homologs in mammals. Among them, Neuropeptide F, the *Drosophila* homolog of neuropeptide Y, is involved in a wide variety of biological processes like foraging behavior, circadian rhythm, and stress. We applied SML imaging on an NPF-positive dorsal lateral soma (dlNPF) and the NPF-positive boutons of dorsal medial soma in the suboesophageal ganglia (SOG), both of which are located about 50µm deep inside the tissue [340].

We first tested SML imaging on the tissue without correction. A wide field image of a bouton in the Ventral Nervous Cord (VNC) region without correction is shown in Figure 5-8(a), and the SML image in Figure 5-8 (b). The SML reconstruction only localized 10.47 fluorophores per square micrometer.

Figure 5-9 shows AO-SML on a NPF-positive soma in an intact *Drosophila* brain lobe. An uncorrected widefield image is shown in Figure 5-9(a). The GA converged in about 5000 frames to 90% of its optimized steady state. The frames after that are used to reconstruct the SML image shown in Figure 5-9(b). The reconstruction has a localization density of 543 fluorophores per square micrometer, more than 50-fold more than the reconstruction in Figure 5-8. Due to the thickness of the sample a larger defocus was induced as well as astigmatism, shown in Figure 5-9(c). Since the fluorescence from NPF is only expressed in a single focal plane, including defocus helps with controlling the focus at the right plane during the time consuming process of SML imaging; 1.1 radians of Z3 still only corresponds to ~220nm of defocus. However, it has to be noted that with samples that have fluorescence from several planes defocus must not be included in order to avoid convergence of the algorithm to another focal plane. A total RMS wavefront aberration of 1.49 radians was removed. If we don't include the defocus term, the RMS wavefront aberration removed was 1.06 radians. The corresponding Strehl ratio with aberrations is 0.107 including defocus. Without the defocus term the Strehl ratio is 0.32.

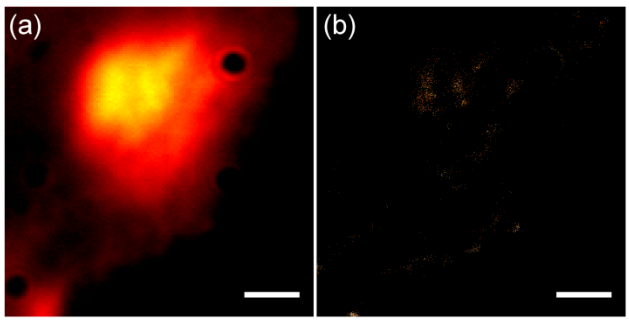

Figure 5-8 - SML image without AO correction on the Drosophila CNS. (a) widefield image of a bouton in the Ventral Nervous Cord. (b) The corresponding SML image. Only 1359 fluorophores could be localized. Scalebars are 2µm.

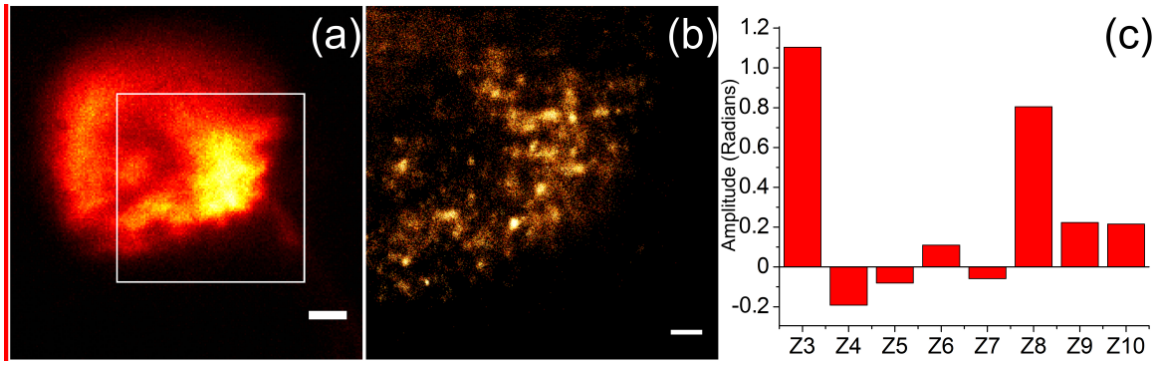

Figure 5-9 - Real time wavefront correction using AO-SML on the Drosophila CNS. (a) widefield image of a soma in a Drosophila brain lobe. The ROI indicates the area where the FM was evaluated. (b) Reconstructed SML image from frames after the algorithm reached an optimized steady state. (c) Bar diagram of the aberrations removed. Scalebars are (a) 2µm, (b) 1µm.

5.4. Particle Swarm Optimization

The algorithm works by collective intelligence, as mentioned before, which means that the particles travel through the search space to find areas that most of the population find to be advantageous as determined by some scoring method. Each particle has a personal memory of the best position it has visited, and also has access to the memories of the other particles. Then, due to their common memory, they converge to the best position. This is similar to the problem of food foraging, where the animals search their territory to find a place with food and direct the rest of the population to that place. The PSO however suffers from outdated memories and loss of diversity which can prevent a PSO from solving dynamic problems. These difficulties have been addressed by several approaches that refresh or erase the memory of the population after a given number of iterations, and that re-diversify the population through randomization or other methods [341].

Here, since we are solving the problem of several aberrations using Zernike polynomials, each particle is a wavefront made of *Nz* Zernike modes. The particles fly

over the *Nz* dimensional search space, searching for the best fitness value. After the evaluation of the wavefronts, a new generation is made by updating the speed and position of the particles. This process repeats until it converges to an optimum solution, or the maximum number of generations reached. The implementation of the PSO we use is the open-source Python package DEAP [342].

The algorithm starts by generating the initial population of particles, within the search area. The population size is typically about 20. Particles are given random values of position and speed. The Fourier Metric (FM) is used to evaluate the wavefront and give fitness value to the particles. Then the speed and position of the particles are updated using equations 1 and 2 below.

$$v_i(t+1) = v_i(t) + \left(r_1 \times \left(p_i^{best} - p_i(t)\right)\right) + \left(r_2 \times \left(p_g^{best} - p_i(t)\right)\right) \tag{5.6}$$

$$p_i(t+1) = p_i(t) + v_i(t) \tag{5.7}$$

where v_i is the speed of the i^{th} particle at time t. r_1 and r_2 are random coefficients with a uniform distribution over the search range. $P_i(t)$ is the position of the particle at time t. p_i^{best}, and p_g^{best} are the particles' personal best position and the best position for the entire group of particles. As shown in the diagram in Figure 5-10, after the update of particles, if the condition such as the maximum number of generation, or a suitable standard deviation is met, the algorithm exits.

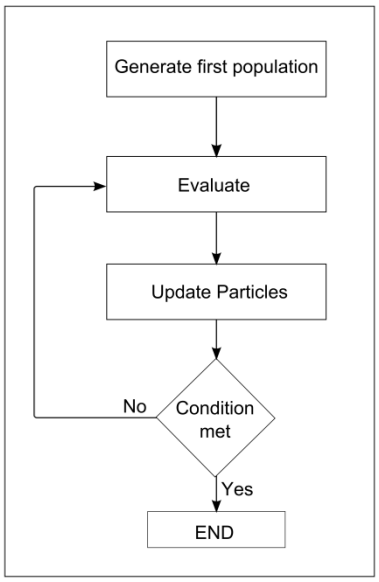

Figure 5-10 – Diagram of Particle Swarm Optimization

5.4.1. Simulation of PSO-AO correction for SML

We ran the algorithm for 100 generations, using the FM metric and the image generation method explained above, on a group of 10 PSFs blinking on a circle with a radius of 1µm. Figure 5-11 shows the results of the simulation. In Figure 5-11 (a) the FM is shown versus generation. We can see that the output of the metric has increased and the standard deviation of the metric values has decreased. Figure 5-11 (a) shows that after about 35 generations the metric has converged to an optimum value. An image from an early generation is shown on the left, and the image of a single PSF after convergence is shown on the right. In Figure 5-11 (b) the value of one coordinate is shown for all the particles as the particles converge to their final position.

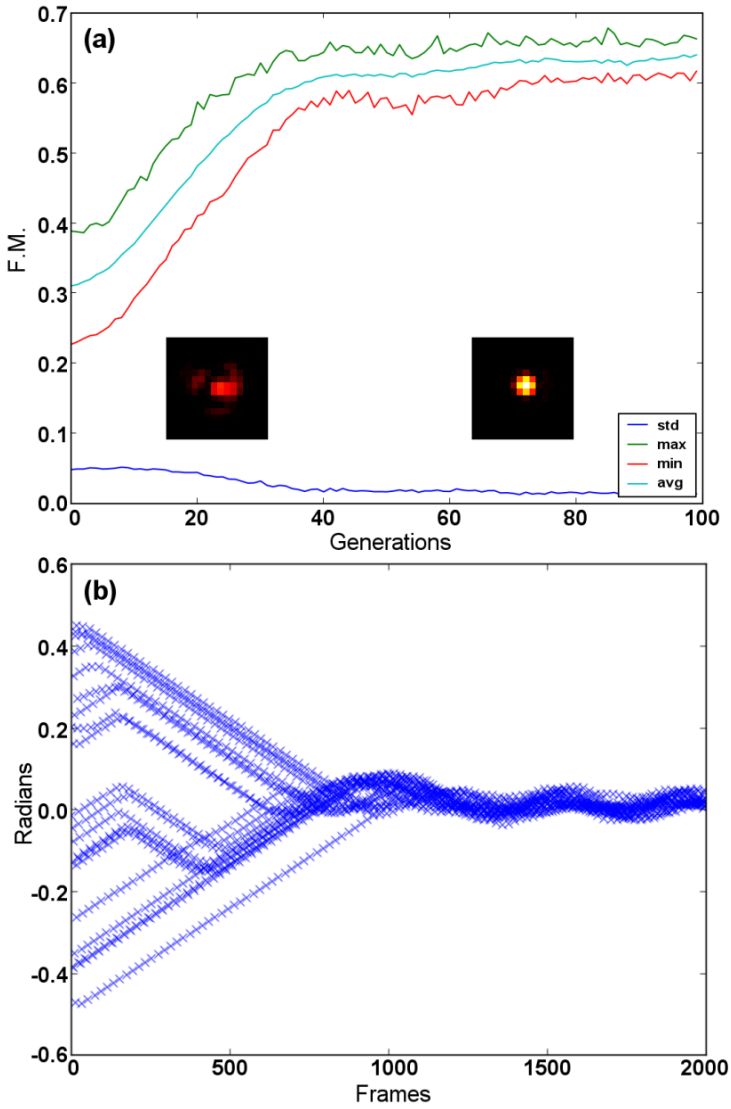

Figure 5-11 - Simulation of a group of molecules in a circle with radius of 1µm. The number of emitting fluorophores is determined by a Poisson distribution, and the fluorophores intensity is determined from an exponential distribution. (a) Plot of the FM vs. generation. The standard deviation, maximum, minimum and average metric values for each generation are shown. (b) Plot of the Z_2^2 term of the wavefront vs. frame for all the particles.

5.4.2. Experimental result of PSO-AO-SML correction for SML

First we tested PSO-AO-SML on a single fluorescent microsphere on the coverslip and then fluorescent microspheres under a *C. elegans* roundworm. Next we applied PSO-AO-SML to imaging of microtubules through the nucleus of a hepG2 cell and imaging of neuropeptides inside a single neuron in a Drosophila (fruit fly) brain lobe.

5.4.2.1. System Aberrations

Figure 5-12 shows the results of the experiment on a 100 nm fluorescent bead. The algorithm starts with a random population. 12 Zernike modes were corrected from Defocus Z_3 to second-order coma Z_{14}. The image on the left is from an early generation before the optimization converged. On the right, the image of the fluorescent bead is shown after the correction. The algorithm ran for 100 generations and reached an optimum value within 25 generations. Each generation in this experiment included 25 measurements. The values of r_1 and r_2 were 2.0. Velocity range was from -0.5 to 0.5, and the position range was from -10 to 10 radians. The peak of intensity increased 3.96 times from the first generation. The removed wavefront error was 1.2 radians. Phase retrieval after the correction revealed 77% Strehl ratio.

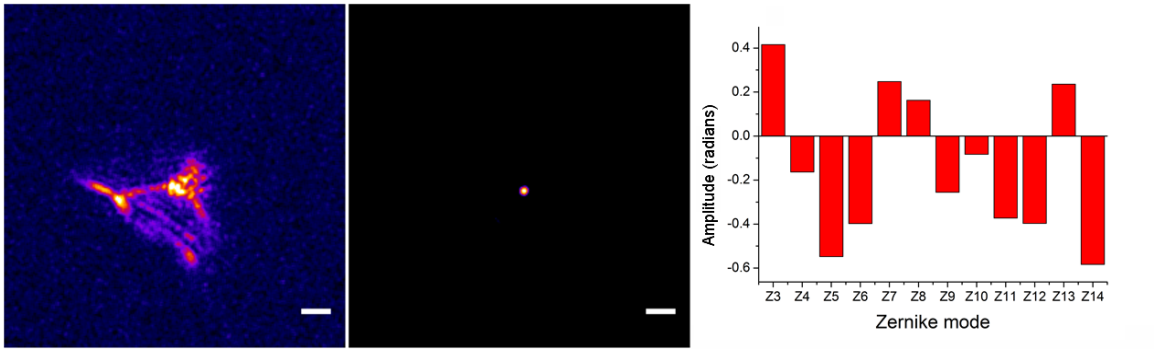

Figure 5-12 - PSO on a single bead. (a) a frame from an early generation. (b) corrected PSF. (c) Zernike coefficients of the correction. Experiment was performed with particles placed in position range from -10 to 10 radians. Velocity range was from -0.5 to 0.5. Population size was 25. Values of r1 and r2 were 1.0 and 2.0 respectively. Sigma of the correction was 0.4 μm^{-1}. Exposure time was 50 ms, and emgain 250 was used. 470 nm LED was used for illumination. Scale bars are 500nm.

Next the algorithm was applied to blinking quantum dots dried on a coverslip. We applied defocus to sample. Figure 5-13 (a)-(c) show initial, midway and final images of the acquired dataset. As can be seen in Figure 5-14 (a), the standard deviation of the FM

value has dropped to almost zero at the 20th generation. It shows the convergence of the algorithm within 500 frames (25 frames per generation).

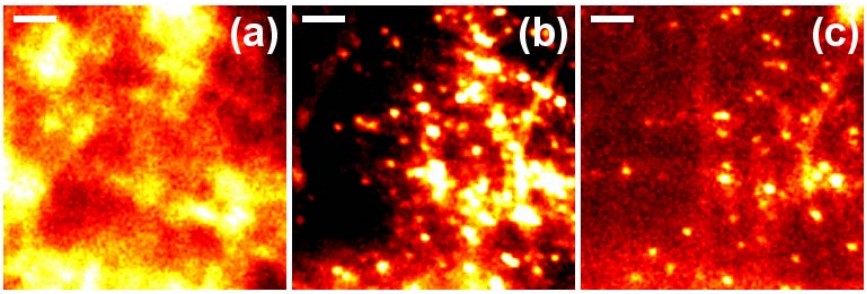

Figure 5-13 - Wavefront correction for blinking QDs. (a) shows the initial random wavefront. (b) shows an image in the 20th generation, and (c) is an image from the 80th generation. Scalebars are 2µm.

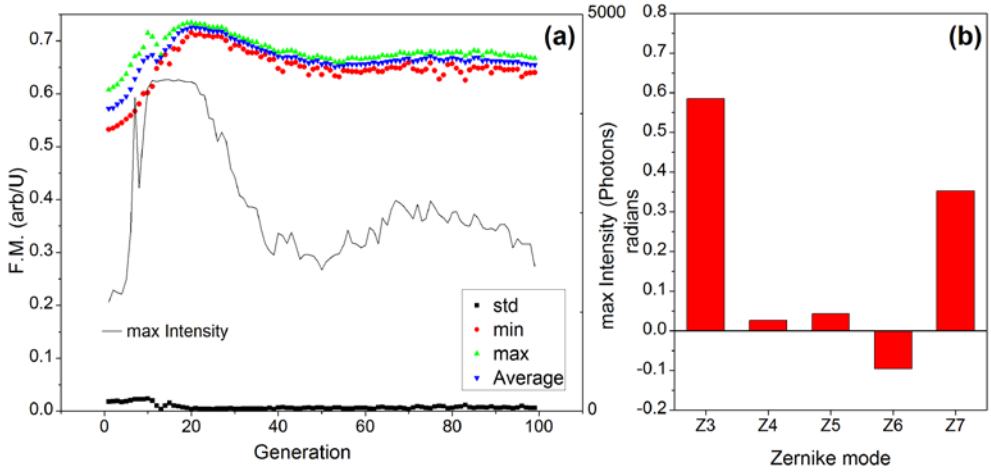

Figure 5-14 - (a) Statistical presentation of Fourier metric values for each generation. The maximum intensity of each frame is also plotted. (b) The Zernike coefficients for the optimum correction.

5.4.2.2. Correction of aberrations induced by a roundworm

Next we applied our PSO to aberrated PSFs due to a *C.elegans* roundworm. We corrected 6 zernike modes; Defocus, Astigmatism (90°, 45°), Coma (horizontal, vertical), and Spherical aberration. The population size was 25. Both r_1 and r_2 were 1.0. Particle positions ranged from -10 to 10 radians, and their velocity from -0.1 to 0.1. The results

are shown in Figure 5-15. The removed aberrations from the worm were 0.65 radians, which translates to 35% Strehl ratio before correction.

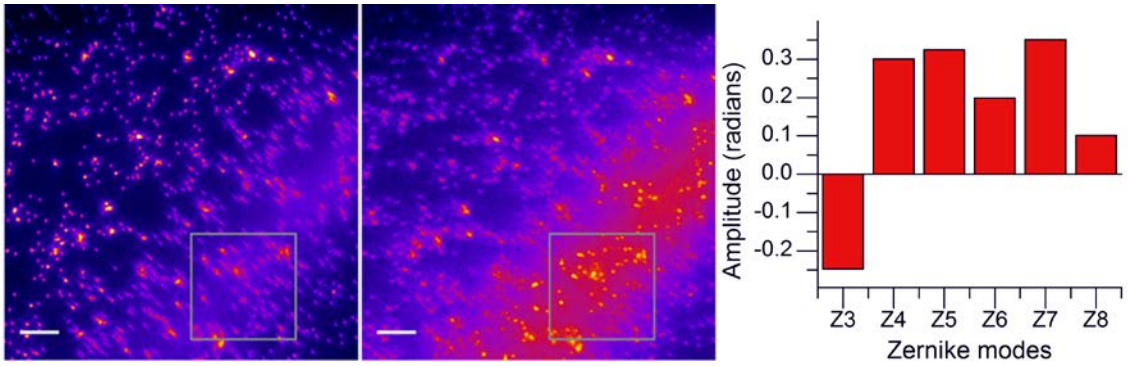

Figure 5-15 - 200nm YG beads under *C.elegans* roundworm. The ROI used for correction is shown as a box in (a) and (b). Aberrated PSFs are shown in (a). After correction PSFs are shown in (b). We can also see the increase in intensity. (c) shows the coefficients of the Zernike modes corrected. Scale bars are 2 um.

5.4.2.3. Real time wavefront correction of SML on a thin cell

With the two previous experiments we showed that the algorithm works very well with steady and dynamic intensity samples. In this next experiment we performed PSO-AO-SML on a thin cell. We imaged microtubules of a Hela cell stained with 565 nm QDs. With the same approach as explained in section 5.3.2.3, we applied AO-PSO to the nucleus of the cell. 6 Zernike modes were corrected. The population size was 25. Values of r_1 and r_2 were 1.0, and 2.0 respectively, which gives twice weight to the swarm's best position compared to the individual's. Particle positions ranged from -10 to 10 radians, and their velocity from -0.1 to 0.1. And the sigma of the merit function was 0.74. The results are shown in Figure 5-16. This experiment was done with a baseline of a corrected wavefront and the amount of removed wavefront error was 0.1 radians. The amount of corrected error is not significant due to the shape of the nucleus in the ROI.

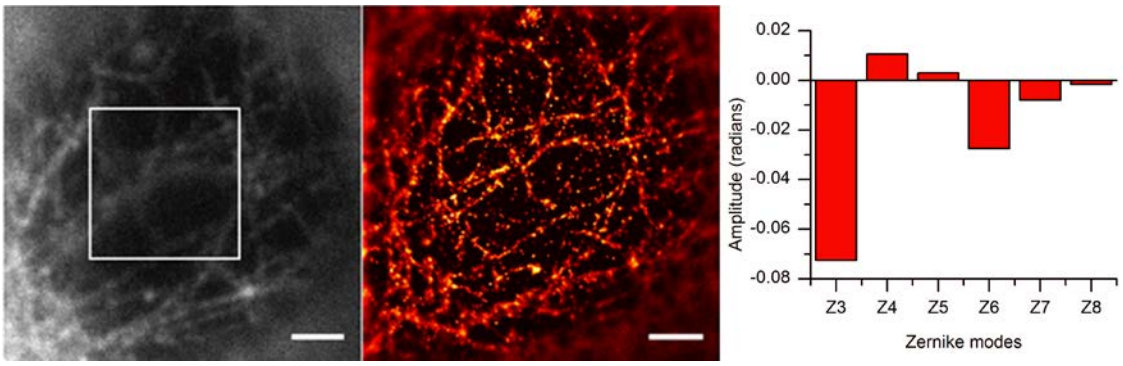

Figure 5-16 – (a) widefield image. The ROI is shown in the white box. (b) shows the final SML image; reconstructed using the frames after correction. (c) shows the coefficients of the zernike modes. Scale bars are 1 um.

5.4.2.4. Real time wavefront correction of SML on a thick tissue

We tested PSO-AO-SML on NPF-positive boutons in a *Drosophila* CNS. A discussion of the *Drosophila* CNS is presented in section 5.3.2.4. The population size was 25. Values of r_1 and r_2 were both 1.0. Particle positions ranged from -5 to 5 radians, and their velocity from -0.1 to 0.1. The sigma of the merit function was 0.4. The results are shown in Figure 5-17. This experiment was done with a baseline of a corrected wavefront for system's aberration. An rms wavefront error of 0.69 radians was measured, which corresponds to a 39% Strehl ratio before correction.

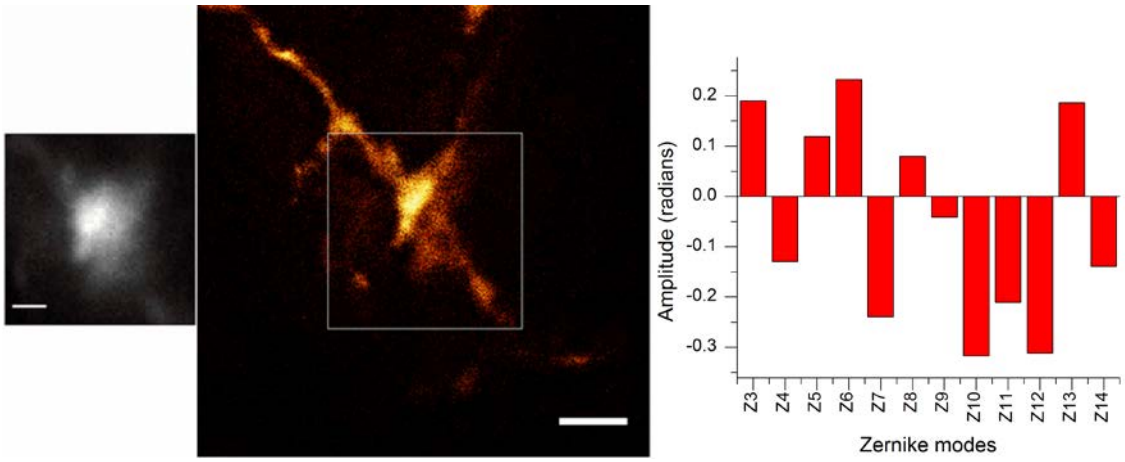

Figure 5-17 – AO-PSO-SML applied to a Boutan in the VNC region of *Drosophila* brain. A widefield image before correction is shown in (a). (b) shows the corrected SML image; reconstructed using the frames after convergence. And (c) shows the coefficients of the Zernike modes. Scale bars are 1µm.

5.5. Resolution enhancement due to wavefront correction

An increase in the Strehl ratio increases the number of photons in the PSF, decreases the PSF width, and decreases the number of background photons. Without any contribution from background fluorescence, the localization precision in SML imaging is given by [343]

$$\Delta x \cong s/\sqrt{N} \tag{5.8}$$

where s is the PSF width and N is the number of photons. We can ignore the contribution to the precision due to the finite pixel size, because it is negligible for a Nyquist sampled pixel size, $a \sim \lambda / 4\mathrm{NA}$. If the Strehl ratio is reduced by a factor of *p*, this results in a reduction in the number of photons in the PSF by ~p as well, so the localization accuracy will be reduced by $\sim\sqrt{p}$ due to the loss of photons in the PSF core. A random wavefront aberration will leave the PSF core intact but create a broad base, so we do not include a change in s in our resolution estimate [344]. Thus a Strehl ratio of

0.85 reduces the accuracy by ~8% and a Strehl ratio of 0.32 reduces the accuracy by ~77%.

The photons that are lost from the PSF core contribute to the background emission so that, even in the absence of background fluorescence, the localization uncertainty will be increased by a background fluorescence term which contributes a variance per pixel of:

$$b^2 = \frac{(1-p)N}{A/dx^2} \tag{5.9}$$

where A is the area over which the lost photons are distributed and *dx* is the pixel dimension; b^2 is the number of scattered photons per pixel. We estimate the Area to ~1.3 μm^2 based on simulations using the measurements of wavefront aberrations through tissue by Schwertner et al. [122]. Inserting Eq. (7) into the equation for localization precision from [343], we arrive at the estimate

$$\Delta x \cong \frac{s}{\sqrt{N}}\sqrt{\frac{1}{p}+\frac{4\sqrt{\pi}sdx(1-p)}{p^2A}} \tag{5.10}$$

With this additional term, a Strehl ratio of 0.85 reduces the accuracy by ~10%, and a Strehl ratio of 0.32 reduces the localization accuracy by a factor of ~2.0. From the results shown in Figs. 6 and 7, it is clear that the improvement in the image is greater than simply a factor of 2. The background fluorescence in the *Drosophila* CNS is not negligible (as in the calculation above), and the wavefront correction improves the image not only by improving the localization accuracy but also by increasing the number of positive localizations which clearly affects the resolution. Nevertheless, Eq. (8) provides an estimate of the change in localization precision due to a change in Strehl ratio, *p*.

5.6. Conclusion

In this section we presented the successful implementation of two machine learning algorithm using a novel correction metric. The Metric uses a high pass filter to measure the high frequency components of the Fourier transform. To make it intensity independent, it is normalized by the sum of all frequency components. GAs uses an evolutionary approach to solve a problem with dynamic features. Here, since fluorophore blinking has dynamic characteristics, GAs are very well suited to our requirements. Using GAs we could optimize the aberrations within 5000 frames. PSO is from the family of collective intelligence, which means that the algorithm uses the memory of the particles' and the swarm's positions to find an optimum solution to a problem. Using PSO we were able to improve the convergence to within 500 frames. We show at least a factor of two improvement in the resolution using the two algorithms.

6. DISCUSSION AND CONCLUSION

We have demonstrated that SML imaging with QDs can be extended to multiple colors without sacrificing resolution. We demonstrate that the QD blueing process can be controlled to maximize the number of achievable localizations, and we report on careful measurements of the microtubule width measured with QSTORM and demonstrate that indeed higher photon counts can be achieved with quantum dots. We demonstrated multicolor QSTORM using two QDs that are far apart in initial wavelength allows us to completely separate the blueing emission into separate channels.

We have presented two approach for correcting wavefront aberrations dynamically during SML imaging by combining a Genetic algorithm and Particle Swarm Optimization with a novel fitness metric that is insensitive to large intensity fluctuations. The genetic algorithm is further refined to reduce the mutation rate and population variability as the wavefront aberration approaches the corrected state, allowing the images to be used for both wavefront correction and the STORM reconstruction. We first applied this approach to flattening the DM and correcting system aberrations while imaging a 100nm fluorescent microsphere. We then corrected the aberrations due to imaging 100nm fluorescent microspheres through a roundworm. The same experiments were also performed using particle swarm optimization.

Applying the approach to SML, we imaged microtubules in hepG2 cells and corrected the aberrations due to imaging through the cell nucleus. While STORM can be

done through the whole cell without AO [345], removing the sample's aberrations corresponds to a RMS wavefront improvement of 0.39 radians. This corresponds to a modest 10% improvement in localization accuracy as we calculated above. We showed the results of AO-SML on NPF imaged in the cell soma approximately 100μm inside an intact Drosophila brain lobe. Here the aberrations removed correspond to an RMS value of 1.49 radians, corresponding to an improvement in localization accuracy of a factor of ~4. The overall improvement in the image is greater than this because the correction not only improves the localization accuracy, but increases the number of localizations as well. The GA converged in about 5000 frames, but this could be improved by optimizing the starting population.

We have applied Particle Swarm Optimization sensorless AO to real-time SML microscopy with a robust and efficient metric that is relatively insensitive to the large intensity fluctuations inherent in SML imaging. By performing PSO we were able to reach an steady state within 500 frames, which helps preserve more blinking events for reconstruction of the final image. We have demonstrated this approach on 2D STORM images, but our approach should be well-suited to volumetric STORM imaging in which the image plane is stepped through the sample. As the image plane moves into the sample, the aberrations will increase but the GA and PSO approaches are well-suited to correct these slowly varying dynamic aberrations and astigmatism can also be dynamically added for 3D STORM [131].

In conclusion this work can be continued in several ways. For the Q-STORM microscopy, one way that the great promise that QDs give for higher resolution SML imaging can be fulfilled by extending it to more than two colors. One possible way can

be by coating the QDs with polymers to delay their blueing. Therefore the emission from the additional channels would pass the filter at a later time that the prior channels are blued. The drawback of this approach is that it makes the QDs larger and harder to get to their target proteins inside a cell or tissue, as well as increasing the linkage error of staining.

The AO for SML imaging can also be approached in several ways. Using wavefront coding I suggest application of low order Bessel beams (a vortex beam) to reduce the conical shape of the illumination 3D PSF to its outer shell. This approach helps to remove the out of focus illumination and therefore reducing the background noise, which directly improves the resolution.

One extension of the AO for wavefront sensorless correction approaches that we showed in this dissertation is by using wavelets as metric. Wavelets have been used to improve the thresholding of PSF in SML image reconstruction [223]. They have potential to be used as intensity independent metric for the iterative wavefront correction approaches. Another possible way to extend AO for SML is by applying phase-retrieval or phase diversity techniques to real time imaging. The speed of the techniques can be improved using GPU (graphical processing unit) image processing. Since SML provides PSFs phase-retrieval can potentially be applied.

APPENDIX A. SAMPLE PREPARATION

5.1. A.1. Fluorescent Microspheres

100nm Yellow-Green Fluorescent microspheres were purchased from Life technologies. The Microspheres were dried on a number 1.5 coverslip. The coverslip was sonicated in Sodium hydroxide (J.T. Baker) for 30 minutes followed by 30minutes sonication in 98% Ethanol (J.T. Baker) after washing 3 times in deionized water. The coverslip was mounted on a slide using glycerol.

5.2. A.2. Sample preparation of microspheres under a C. elegans sample

15µl of a solution containing 200nm yellow-green fluorescent microspheres (Invitrogen) diluted by a factor of 10^5 in deionized water, was dried on an electrostatically charged glass slide (Shandon Colorfrost from Thermo Scientific). *C. elegans* roundworms were then placed on the slide on the dried layer of microspheres and fixed with Tetramisole solution, and a no. 1.5 coverslip was fixed on top with nail polish.

5.3. A.3. Tissue culture cells

HepG2 (ATCC) cells were cultured in ATCC-formulated Eagle's Minimum Essential Medium with 10% fetal bovine serum (FBS). The cells were plated onto a PLL (Poly-L-Lysine) coated glass-bottom dish at an initial confluency of about 50% and cultured for one day to let the cells attach to the dish. Hela cells were cultured in Dulbecco’s Modified Eagle Medium (Thermo

Fisher Scientific MT15-013CV with Glutamine and high glucose) with 10% FBS, 1% penn/strep, and 1% Amphotericin B. The cells were cultured on treated 5ml vented flasks (Corning), up to 90% confluency.

To immunostain,the cells, the culture medium was aspirated, and the cells were washed with Phosphate-Buffered Saline (PBS) once and fixed in a 1:1 Acetone / Methanol solution for 10 min. After 3 washes with PBS, the cells were blocked by incubation with blocking buffer, consisting of 6% Bovine Serum Albumin (BSA) and 10% normal serum in PBS, for 2 hours. Then the blocking buffer was aspirated, and the cells were incubated with Anti α-Tubulin Rabbit primary antibody (abcam) diluted in 6% BSA at 4°C overnight. Then the cells were washed 3 times with the washing buffer for 10 minutes per wash. Then Qdot 565 goat F(ab')2 anti-rabbit IgG conjugate (H+L) (Life Technologies) secondary antibody was added to the sample in 6% BSA and incubated for 2 hours, protected from light. The cells were washed again 3 times with washing buffer (0.2% BSA and 0.5% Triton X-100 in PBS) and 1 time with PBS for 10 minutes per wash and stored in PBS before imaging. Immediately before imaging, the buffer was switched to a solution containing 20% glycerol (v/v) for preserving QDs from fast oxidation [332].

5.4. A.4. Sample preparation of the Drosophila Central Nervous System (CNS)

Intact CNS tissues were freshly dissected from 74 AEL *Drosophila* larvae and immediately fixed in 4% paraformaldehyde for 1-1.5 hours. The tissues were then washed 6 times, 20 minutes each time, in PBS solution containing 0.1% TritonX-100 (PBT). About 20 tissues were incubated in 1ml rabbit anti-NPF primary antibody overnight. The primary antibody was pre-incubated with 50μg/ml C8 peptide at 4°C for 12 hours to block non-specific binding

[340]. After additional 6 PBT washes, the tissues were incubated in Alexa Fluor 647 F(ab')2 Fragment of Goat Anti-Rabbit IgG (H+L) secondary antibody purchased from Life Technologies diluted 1:500 from the original concentration overnight. The tissues were washed with PBT six times after staining. The tissues were placed in the STORM imaging buffer 20 minutes prior to imaging.

5.5. A.5. Preparation of SML imaging buffer (MEA)

The MEA buffer for Alexa 647 was prepared according to the Nikon N-STORM protocol, by mixing 310µl Buffer B, 35µl MEA buffer, and 3.5µl GLOX solution. Buffer B was made by combining 50 mM Tris pH 8.0, 10 mM NaCl, and 10% w/v glucose. 1M MEA buffer was made by mixing 77mg of Cysteamine (Sigma-Aldrich #30070) in 1ml of 0.25N HCl, , GLOX solution was made by mixing 0.56 mg/mL Glucose Oxidase (Sigma-Aldrich #G2133), 0.17 mg/mL Catalase (Sigma-Aldrich #C40), in 200µl of a buffer containing 10mM Tris ph8.0 and 50mM NaCl. The solution was vortexed, spinned down at 14,000 rpm, and only the supernatant was used.

APPENDIX B – IMAGING APPARATUS

Imaging data was acquired using an Olympus IX71 inverted microscope with a 60x oil objective (Plan Apo N). The microscope is equipped with a PriorProScan xy stage and a Prior NanoScanZ piezo stage for focusing. Fluorescence was imaged using an Andor EMCCD camera (DV887DCS-BV with 14bit ADC). At the left-side port of the IX71, additional optics are inserted to re-image the back pupil plane of the objective onto a deformable mirror (Mirao 52E, Imagine Optic). The diameter of the deformable mirror limits the system NA to 1.28. After the deformable mirror, a further image plane is generated which is then relayed to the CCD camera with an additional 3x magnification (lenses L3 and L4) so that the image is sampled at the Nyquist frequency by the CCD. A CCD pixel corresponds to 89nm at the sample plane. For QD 656nm imaging a 504nm/12 (Semrock) filter was placed in the imaging path. For Alexa 647 imaging a 700/80nm filter (FF01-515-588-700 Omega filters) was used. The QDs are excited with a 488nm laser (Cyan 488, Newport) which is coupled into a 100µm core diameter fiber. The fiber is shaken using a fiber shaker to remove speckle [346]. To excite Alexa Fluor 647, a 660nm laser (Obis 660LX, Coherent) is coupled into a separate fiber attached to the shaker. The setup used for Adaptive Optics Experiments is shown in Figure B-1.

For filtering and other image processing methods Python(x,y) version 2.7.6.1 was used. Image reconstruction was done using RapidSTORM version 2.21 [347].

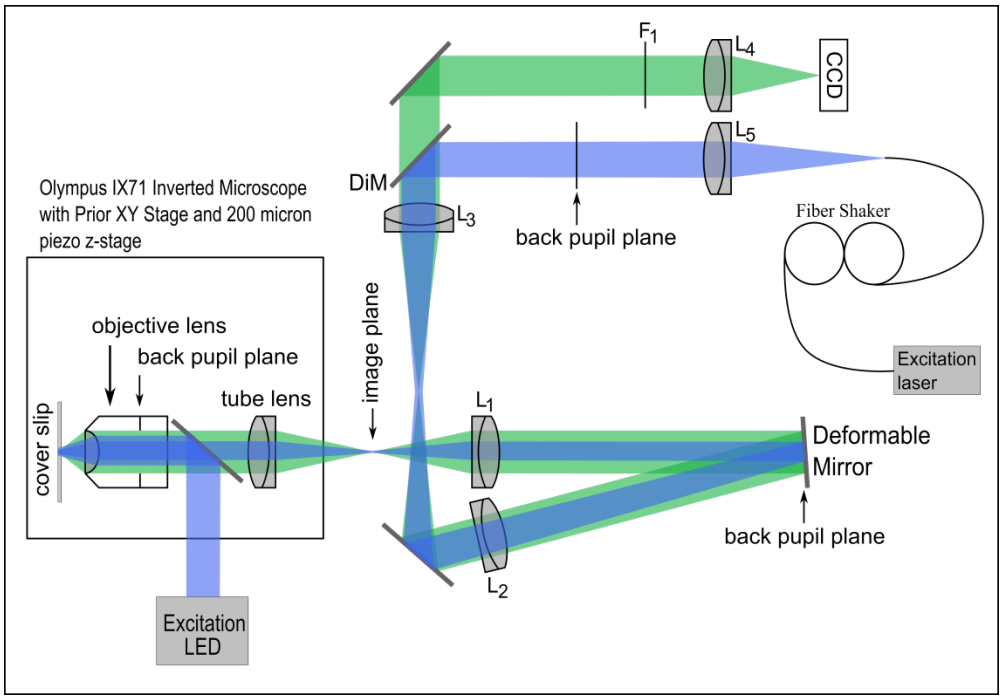

Figure B-1 - Diagram of the optical setup used for Adaptive Optics experiments.

We designed a filter plate to separate the emitted light from the two QDs in the QSTORM experiment. The AutoCAD design is shown in Figure B-2. Another plate was also designed to only hold a mirror, for fast switching between the two colors and single color modes. Pictures of the assembled mount in practice are shown in Figure B-3.

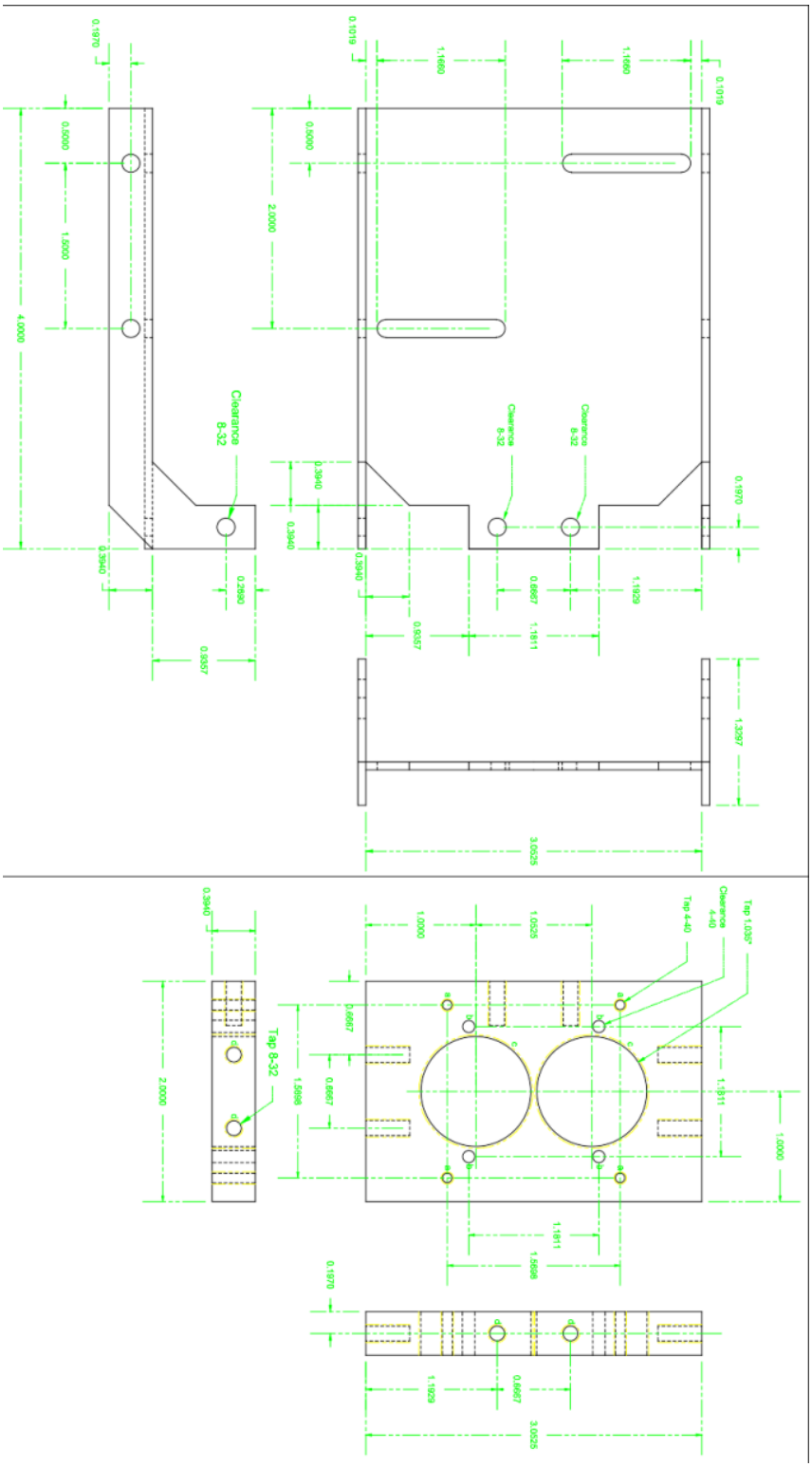

Figure B-2 - Drawing of the filter plate used for QSTORM project.

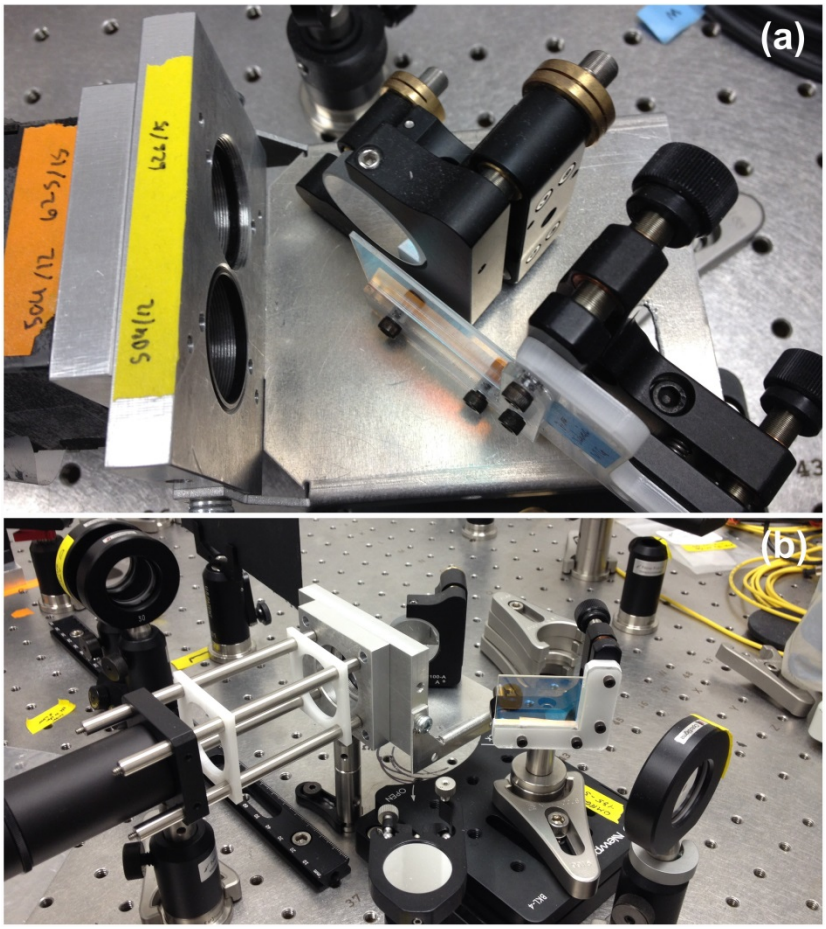

Figure B-3 - Picture of the filter plate used for QSTORM project is shown in (a). Another plate was also designed to switch easily between single color and two color modes.

REFERENCES

1. Ter-Pogossian, M.M., et al., *A Positron-Emission Transaxial Tomograph for Nuclear Imaging (PETT).* Radiology, 1975. **114**(1): p. 89-98.
2. Lauterbur, P.C., *Image Formation by Induced Local Interactions: Examples Employing Nuclear Magnetic Resonance.* Nature, 1973. **242**(5394): p. 190-191.
3. Ruska, E. and M. Knoll, *Die magnetische Sammelspule für schnelle Elektronenstrahlen. (The magnetic concentrating coil for fast electron beams.)* Z. techn. Physik 1931. **12**: p. 389-400.
4. Fernandez-Suarez, M. and A.Y. Ting, *Fluorescent probes for super-resolution imaging in living cells.* Nat Rev Mol Cell Biol, 2008. **9**(12): p. 929-943.
5. O, H., *Das Fluoreszenzmikroskop.* Z Wiss Mikrosk, 1911. **28**(330): p. 7.
6. H, L., *Das Lumineszenzmikroskop, seine Grundlagen und seine Anwendungen.* Z. Wiss. Mikrosk., 1913. **30**: p. 417-470.
7. Abbe, E., *A contribution to the theory of the microscope, and the nature of microscopic vision.*, in *Proceedings of the Bristol Naturalists' Society*. 1874. p. 200-272.
8. Abbe, E., *Beitrage zur Theorie des Mikroskops und der mikroskopischen Wahrnehmung. M.* Schultze's Archiv fur mikroskopische Anatomie, 1873. **9**: p. 413 - 468.
9. Lauterbach, M., *Finding, defining and breaking the diffraction barrier in microscopy - a historical perspective.* Optical Nanoscopy, 2012. **1**(1): p. 8.
10. Matsuda, A., et al., *Condensed mitotic chromosome structure at nanometer resolution using PALM and EGFP- histones.* PLoS One, 2010. **5**(9): p. e12768.
11. Hell, S.W. and J. Wichmann, *Breaking the diffraction resolution limit by stimulated emission: stimulated-emission-depletion fluorescence microscopy.* Optics Letters, 1994. **19**(11): p. 780-782.
12. Hell, S. and M. Kroug, *Ground-state-depletion fluorescence microscopy: a concept for breaking the diffraction resolution limit.* Appl Phys B: Lasers and Opt, 1995. **60**(5): p. 495 - 497.
13. Goodman, J.W., *Introduction to Fourier Optics*. 1996: McGraw-Hill.
14. Gustafsson, M.G., *Surpassing the lateral resolution limit by a factor of two using structured illumination microscopy.* J Microsc, 2000. **198**(Pt 2): p. 82-7.
15. Betzig, E., et al., *Imaging intracellular fluorescent proteins at nanometer resolution.* Science, 2006. **313**(5793): p. 1642-5.

16. Hess, S.T., T.P.K. Girirajan, and M.D. Mason, *Ultra-high resolution imaging by fluorescence photoactivation localization microscopy.* Biophys. J., 2006. **91**(11): p. 4258-4272.

17. Rust, M., M. Bates, and X. Zhuang, *Sub-diffraction-limit imaging by stochastic optical reconstruction microscopy (STORM).* Nat Methods, 2006. **3**(10): p. 793 - 795.

18. Heilemann, M., et al., *Subdiffraction-Resolution Fluorescence Imaging with Conventional Fluorescent Probes.* Angewandte Chemie International Edition, 2008. **47**(33): p. 6172-6176.

19. Xu, J., K.F. Tehrani, and P. Kner, *Multicolor 3D Super-resolution Imaging by Quantum Dot Stochastic Optical Reconstruction Microscopy.* ACS Nano, 2015. **9**(3): p. 2917-2925.

20. Tehrani, K.F., et al., *Adaptive optics stochastic optical reconstruction microscopy (AO-STORM) using a genetic algorithm.* Optics Express, 2015. **23**(10): p. 13677-13692.

21. Mertz, J., *Introduction to optical microscopy / Jerome Mertz*. 2010: Greenwood Village, Colo. : Roberts, c2010.

22. Rayleigh, J., *On the theory of optical images, with special reference to the microscope. Philos Mag.* Ser 5, 1896. **42**(255): p. 167 - 195.

23. Sparrow, C., *On spectroscopic resolving power.* Astrophysical J, 1916. **44**(2): p. 76 - 86.

24. Betzig, E., et al., *Breaking the Diffraction Barrier: Optical Microscopy on a Nanometric Scale.* Science, 1991. **251**(5000): p. 1468-1470.

25. Betzig, E. and J.K. Trautman, *Near-Field Optics: Microscopy, Spectroscopy, and Surface Modification Beyond the Diffraction Limit.* Science, 1992. **257**(5067): p. 189-195.

26. Synge, E.H., *XXXVIII. A suggested method for extending microscopic resolution into the ultra-microscopic region.* The London, Edinburgh, and Dublin Philosophical Magazine and Journal of Science, 1928. **6**(35): p. 356-362.

27. Pohl, D.W., W. Denk, and M. Lanz, *Optical stethoscopy: Image recording with resolution λ/20.* Applied Physics Letters, 1984. **44**(7): p. 651-653.

28. Lewis, A., et al., *Development of a 500 Å spatial resolution light microscope: I. light is efficiently transmitted through λ/16 diameter apertures.* Ultramicroscopy, 1984. **13**(3): p. 227-231.

29. de Lange, F., et al., *Cell biology beyond the diffraction limit: near-field scanning optical microscopy.* J Cell Sci, 2001. **114**(Pt 23): p. 4153-60.

30. de Bakker, B.I., et al., *Nanometer-scale organization of the alpha subunits of the receptors for IL2 and IL15 in human T lymphoma cells.* J Cell Sci, 2008. **121**(Pt 5): p. 627-33.

31. Sheppard, C.J.R. and T. Wilson, *Depth of field in the scanning microscope.* Optics Letters, 1978. **3**(3): p. 115-117.

32. Sheppard, C.J.R. and T. Wilson, *Image Formation in Scanning Microscopes with Partially Coherent Source and Detector.* Optica Acta: International Journal of Optics, 1978. **25**(4): p. 315-325.

33. Cremer, C. and T. Cremer, *Considerations on a laser-scanning-microscope with high resolution and depth of field.* Microsc Acta, 1978. **81**(1): p. 31-44.

34. Sheppard, C.J.R. and T. Wilson, *The theory of the direct-view confocal microscope.* Journal of Microscopy, 1981. **124**(2): p. 107-117.

35. Gustafsson, Agard, and Sedat, *I5M: 3D widefield light microscopy with better than 100 nm axial resolution.* Journal of Microscopy, 1999. **195**(1): p. 10-16.

36. Hell, S. and E. Stelzer, *Properties of a 4Pi confocal fluorescence microscope.* J Opt, Soc Am A: Opt, Image Sci, Vision, 1992. **9**(12): p. 2159 - 2166.

37. Brakenhoff, G.J., et al., *Three-dimensional chromatin distribution in neuroblastoma nuclei shown by confocal scanning laser microscopy.* Nature, 1985. **317**(6039): p. 748-9.

38. Glass, M. and T. Dabbs, *The experimental effect of detector size on confocal lateral resolution.* Journal of Microscopy, 1991. **164**(2): p. 153-158.

39. Sandison, D.R., et al., *Quantitative comparison of background rejection, signal-to-noise ratio, and resolution in confocal and full-field laser scanning microscopes.* Applied Optics, 1995. **34**(19): p. 3576-3588.

40. Wilson, T., *The Role of the Pinhole in Confocal Imaging System*, in *Handbook of Biological Confocal Microscopy*, J. Pawley, Editor. 1995, Springer US. p. 167-182.

41. Gustafsson, M.G.L., *Extended resolution fluorescence microscopy.* Current Opinion in Structural Biology, 1999. **9**(5): p. 627-628.

42. Gustafsson, M.G.L., D.A. Agard, and J.W. Sedat, *Sevenfold improvement of axial resolution in 3D wide-field microscopy using two objective lenses.* Proceedings of SPIE, 1995(1): p. 147.

43. Gustafsson, M.G.L., D.A. Agard, and J.W. Sedat. *3D widefield microscopy with two objective lenses: experimental verification of improved axial resolution*. 1996.

44. Nagorni, M. and S.W. Hell, *Coherent use of opposing lenses for axial resolution increase in fluorescence microscopy. I. Comparative study of concepts.* Journal of the Optical Society of America A, 2001. **18**(1): p. 36-48.

45. Zipfel, W.R., R.M. Williams, and W.W. Webb, *Nonlinear magic: multiphoton microscopy in the biosciences.* Nat Biotech, 2003. **21**(11): p. 1369-1377.

46. Hell, S. and E.H.K. Stelzer, *Fundamental improvement of resolution with a 4Pi-confocal fluorescence microscope using two-photon excitation.* Optics Communications, 1992. **93**(5–6): p. 277-282.

47. Denk, W., J. Strickler, and W. Webb, *Two-photon laser scanning fluorescence microscopy.* Science, 1990. **248**(4951): p. 73-76.

48. McClain, W.M., *Two-photon molecular spectroscopy.* Accounts of Chemical Research, 1974. **7**(5): p. 129-135.

49. Friedrich, D.M. and W.M. McClain, *Two-Photon Molecular Electronic Spectroscopy.* Annual Review of Physical Chemistry, 1980. **31**(1): p. 559-577.

50. Friedrich, D.M., *Two-photon molecular spectroscopy.* Journal of Chemical Education, 1982. **59**(6): p. 472.

51. Birge, R.R., *Two-photon spectroscopy of protein-bound chromophores.* Accounts of Chemical Research, 1986. **19**(5): p. 138-146.

52. Callis, P.R., *TWO-PHOTON–INDUCED FLUORESCENCE.* Annual Review of Physical Chemistry, 1997. **48**(1): p. 271-297.

53. Franken, P.A., et al., *Generation of Optical Harmonics.* Physical Review Letters, 1961. **7**(4): p. 118-119.

54. Gannaway, J.N. and C.J.R. Sheppard, *Second-harmonic imaging in the scanning optical microscope.* Optical and Quantum Electronics, 1978. **10**(5): p. 435-439.

55. Sheppard, C.J. and R. Kompfner, *Resonant scanning optical microscope.* Appl Opt, 1978. **17**(18): p. 2879-82.

56. Gauderon, R., P.B. Lukins, and C.J. Sheppard, *Effect of a confocal pinhole in two-photon microscopy.* Microsc Res Tech, 1999. **47**(3): p. 210-4.

57. Campagnola, P.J. and L.M. Loew, *Second-harmonic imaging microscopy for visualizing biomolecular arrays in cells, tissues and organisms.* Nat Biotech, 2003. **21**(11): p. 1356-1360.

58. Cox, G., et al., *3-dimensional imaging of collagen using second harmonic generation.* J Struct Biol, 2003. **141**(1): p. 53-62.

59. Barad, Y., et al., *Nonlinear scanning laser microscopy by third harmonic generation.* Applied Physics Letters, 1997. **70**(8): p. 922-924.

60. Muller, M., et al., *3D microscopy of transparent objects using third-harmonic generation.* J Microsc, 1998. **191**(3): p. 266-274.

61. Squier, J., et al., *Third harmonic generation microscopy.* Optics Express, 1998. **3**(9): p. 315-324.

62. Kaiser, W. and C.G.B. Garrett, *Two-Photon Excitation in CaF2:Eu2+.* Physical Review Letters, 1961. **7**(6): p. 229-231.

63. Diaspro, A., G. Chirico, and M. Collini, *Two-photon fluorescence excitation and related techniques in biological microscopy.* Quarterly Reviews of Biophysics, 2005. **38**(02): p. 97-166.

64. Diaspro, A., et al., *Multi-photon excitation microscopy.* BioMedical Engineering OnLine, 2006. **5**: p. 36-36.

65. Lukosz, W., *Optical Systems with Resolving Powers Exceeding the Classical Limit.* Journal of the Optical Society of America, 1966. **56**(11): p. 1463-1471.

66. Lukosz, W., *Optical Systems with Resolving Powers Exceeding the Classical Limit. II.* Journal of the Optical Society of America, 1967. **57**(7): p. 932-939.

67. Hell, S. and J. Wichmann, *Breaking the diffraction resolution limit by stimulated emission: stimulated-emission-depletion fluorescence microscopy.* Opt Lett, 1994. **19**(11): p. 780 - 782.

68. Klar, T.A. and S.W. Hell, *Subdiffraction resolution in far-field fluorescence microscopy.* Optics Letters, 1999. **24**(14): p. 954-956.

69. Klar, T.A., et al., *Fluorescence microscopy with diffraction resolution barrier broken by stimulated emission.* Proceedings of the National Academy of Sciences, 2000. **97**(15): p. 8206-8210.

70. Donnert, G., et al., *Macromolecular-scale resolution in biological fluorescence microscopy.* Proceedings of the National Academy of Sciences, 2006. **103**(31): p. 11440-11445.

71. Donnert, G., et al., *Two-Color Far-Field Fluorescence Nanoscopy.* Biophysical Journal, 2007. **92**(8): p. L67-L69.

72. Schmidt, R., et al., *Spherical nanosized focal spot unravels the interior of cells.* Nat Meth, 2008. **5**(6): p. 539-544.

73. Hell, S.W., *Far-field optical nanoscopy.* Science, 2007. **316**(5828): p. 1153-1158.

74. Hell, S.W., *Toward fluorescence nanoscopy.* Nature Biotechnology, 2003. **21**(11): p. 1347-1355.

75. Heintzmann, R. and C.G. Cremer. *Laterally modulated excitation microscopy: improvement of resolution by using a diffraction grating*. 1999.

76. Gustafsson, M.G.L., et al., *Three-Dimensional Resolution Doubling in Wide-Field Fluorescence Microscopy by Structured Illumination.* Biophys. J., 2008. **94**(12): p. 4957-4970.

77. Gustafsson, M.G., *Nonlinear structured-illumination microscopy: wide-field fluorescence imaging with theoretically unlimited resolution.* Proc Natl Acad Sci U S A, 2005. **102**(37): p. 13081-6.

78. Kner, P., et al., *Super-resolution video microscopy of live cells by structured illumination.* Nat Methods, 2009. **6**(5): p. 339-42.

79. Ober, R., et al., *Quantitative Aspects of Single-Molecule Microscopy: Information-theoretic analysis of single-molecule data.* Signal Processing Magazine, IEEE, 2015. **32**(1): p. 58-69.

80. Sharonov, A. and R.M. Hochstrasser, *Wide-field subdiffraction imaging by accumulated binding of diffusing probes.* Proceedings of the National Academy of Sciences, 2006. **103**(50): p. 18911-18916.

81. Sharonov, A., et al., *Lipid diffusion from single molecules of a labeled protein undergoing dynamic association with giant unilamellar vesicles and supported bilayers.* Langmuir, 2008. **24**(3): p. 844-50.

82. Kuo, C. and R.M. Hochstrasser, *Super-resolution Microscopy of Lipid Bilayer Phases.* Journal of the American Chemical Society, 2011. **133**(13): p. 4664-4667.

83. Lew, M.D., et al., *Three-dimensional superresolution colocalization of intracellular protein superstructures and the cell surface in live Caulobacter crescentus.* Proceedings of the National Academy of Sciences, 2011. **108**(46): p. E1102-E1110.

84. Dertinger, T., et al., *Fast, background-free, 3D super-resolution optical fluctuation imaging (SOFI).* Proceedings of the National Academy of Sciences of the United States of America, 2009. **106**(52): p. 22287-22292.

85. Moerner, W.E. and L. Kador, *Optical detection and spectroscopy of single molecules in a solid.* Physical Review Letters, 1989. **62**(21): p. 2535-2538.

86. Orrit, M. and J. Bernard, *Single pentacene molecules detected by fluorescence excitation in a p-terphenyl crystal.* Physical Review Letters, 1990. **65**(21): p. 2716-2719.

87. Brooks Shera, E., et al., *Detection of single fluorescent molecules.* Chemical Physics Letters, 1990. **174**: p. 553-557.

88. Rigler, R. and J. Widengren, *Ultrasensitive detection of single molecules by fluorescence correlation spectroscopy.* BioScience, 1990. **3**: p. 180-183.

89. Nie, S., D. Chiu, and R. Zare, *Probing individual molecules with confocal fluorescence microscopy.* Science, 1994. **266**(5187): p. 1018-1021.

90. Funatsu, T., et al., *Imaging of single fluorescent molecules and individual ATP turnovers by single myosin molecules in aqueous solution.* Nature, 1995. **374**(6522): p. 555-559.

91. Betzig, E., *Proposed method for molecular optical imaging.* Optics Letters, 1995. **20**(3): p. 237-239.

92. Dickson, R.M., et al., *On/off blinking and switching behaviour of single molecules of green fluorescent protein.* Nature, 1997. **388**(6640): p. 355-358.

93. Patterson, G.H. and J. Lippincott-Schwartz, *A photoactivatable GFP for selective photolabeling of proteins and cells.* Science, 2002. **297**(5588): p. 1873-7.

94. Bates, M., et al., *Multicolor super-resolution imaging with photo-switchable fluorescent probes.* Science, 2007. **317**(5845): p. 1749-53.

95. Dani, A., et al., *Superresolution imaging of chemical synapses in the brain.* Neuron, 2010. **68**(5): p. 843-56.

96. Huang, B., et al., *Whole-cell 3D STORM reveals interactions between cellular structures with nanometer-scale resolution.* Nat Methods, 2008. **5**(12): p. 1047-52.

97. Huang, B., et al., *Three-dimensional super-resolution imaging by stochastic optical reconstruction microscopy.* Science, 2008. **319**(5864): p. 810-3.

98. Shroff, H., et al., *Live-cell photoactivated localization microscopy of nanoscale adhesion dynamics.* Nat Meth, 2008. **5**: p. 417-423.

99. Mlodzianoski, M.J. and J. Bewersdorf, *3D-Resolution In FPALM/PALM/STORM.* Biophysical Journal, 2009. **96**(3, Supplement 1): p. 636a-637a.

100. Pavani, S.R.P., et al., *Three-dimensional, single-molecule fluorescence imaging beyond the diffraction limit by using a double-helix point spread function.* Proceedings of the National Academy of Sciences, 2009. **106**(9): p. 2995-2999.

101. Shtengel, G., et al., *Interferometric fluorescent super-resolution microscopy resolves 3D cellular ultrastructure.* Proceedings of the National Academy of Sciences, 2009. **106**(9): p. 3125-3130.

102. Shim, S.H., et al., *Super-resolution fluorescence imaging of organelles in live cells with photoswitchable membrane probes.* Proceedings of the National Academy of Sciences of the United States of America, 2012. **109**(35): p. 13978-13983.

103. Zhuang, X., *Nano-imaging with STORM.* Nat Photonics, 2009. **3**(7): p. 365 - 367.

104. Thompson, R.E., D.R. Larson, and W.W. Webb, *Precise nanometer localization analysis for individual fluorescent probes.* Biophys J, 2002. **82**(5): p. 2775-2783.

105. Dempsey, G.T., et al., *Evaluation of fluorophores for optimal performance in localization-based super-resolution imaging.* Nat Meth, 2011. **8**(12): p. 1027-1036.

106. Olivier, N., et al., *Resolution Doubling in 3D-STORM Imaging through Improved Buffers.* PLoS ONE, 2013. **8**(7): p. e69004.

107. Xu, J.Q., K.F. Tehrani, and P. Kner, *Multicolor 3D Super-resolution Imaging by Quantum Dot Stochastic Optical Reconstruction Microscopy.* Acs Nano, 2015. **9**(3): p. 2917-2925.

108. Hoyer, P., et al., *Quantum Dot Blueing and Blinking Enables Fluorescence Nanoscopy.* Nano Lett, 2010. **11**(1): p. 245-250.

109. van Sark, W., et al., *Photooxidation and photobleaching of single CdSe/ZnS quantum dots probed by room-temperature time-resolved spectroscopy.* Journal of Physical Chemistry B, 2001. **105**(35): p. 8281-8284.

110. Resch-Genger, U., et al., *Quantum dots versus organic dyes as fluorescent labels.* Nature Methods, 2008. **5**(9): p. 763-775.

111. Lidke, K., et al., *Superresolution by localization of quantum dots using blinking statistics.* Opt Express, 2005. **13**(18): p. 7052 - 7062.

112. Whitford, A.E. and G.E. Kron, *Photoelectric Guiding of Astronomical Telescopes.* Review of Scientific Instruments, 1937. **8**(3): p. 78-82.

113. Babcock, H.W., *A Photoelectric Guider for Astronomical Telescopes.* Astronomical Journal, 1948. **107**: p. 73.

114. Babcock, H.W., *THE POSSIBILITY OF COMPENSATING ASTRONOMICAL SEEING.* Publications of the Astronomical Society of the Pacific, 1953. **65**(386): p. 229-236.

115. Fried, D.L., *Optical Resolution Through a Randomly Inhomogeneous Medium for Very Long and Very Short Exposures.* Journal of the Optical Society of America (1917-1983), 1966. **56**(10): p. 1372.

116. Hardy, J.W., *Adaptive optics for astronomical telescopes*. Oxford series in optical and imaging sciences ; 16. 1998, New York: Oxford University Press. 438.

117. Hell, S., et al., *Aberrations in confocal fluorescence microscopy induced by mismatches in refractive-index.* Journal of Microscopy, 1993. **169**: p. 391-405.

118. Noll, R.J., *Zernike polynomials and atmospheric turbulence*. Journal of the Optical Society of America, 1976. **66**(3): p. 207-211.

119. Vellekoop, I.M. and A.P. Mosk, *Focusing coherent light through opaque strongly scattering media.* Optics Letters, 2007. **32**(16): p. 2309-2311.

120. Booth, M.J., *Adaptive optics in microscopy.* Philos Transact A Math Phys Eng Sci, 2007. **365**(1861): p. 2829-43.

121. Booth, M.J., M.A.A. Neil, and T. Wilson, *Aberration correction for confocal imaging in refractive-index-mismatched media.* J Microsc, 1998. **192**(2): p. 90-98.

122. Schwertner, M., M. Booth, and T. Wilson, *Characterizing specimen induced aberrations for high NA adaptive optical microscopy*. Opt. Express, 2004. **12**(26): p. 6540-6552.

123. Schwertner, M., et al., *Measurement of specimen-induced aberrations of biological samples using phase stepping interferometry.* Journal of Microscopy, 2004. **213**(1): p. 11-19.

124. Booth, M.J., et al., *Adaptive aberration correction in a confocal microscope.* Proc Natl Acad Sci U S A, 2002. **99**(9): p. 5788-92.

125. Kam, Z., et al., *Modelling the application of adaptive optics to wide-field microscope live imaging.* J Microsc, 2007. **226**(Pt 1): p. 33-42.

126. Azucena, O., et al., *Adaptive optics wide-field microscopy using direct wavefront sensing.* Opt. Lett., 2011. **36**(6): p. 825-827.

127. Tao, X., et al., *Adaptive optical two-photon microscopy using autofluorescent guide stars.* Optics Letters, 2013. **38**(23): p. 5075-5078.

128. Rueckel, M., J.A. Mack-Bucher, and W. Denk, *Adaptive wavefront correction in two-photon microscopy using coherence-gated wavefront sensing.* Proc Natl Acad Sci U S A, 2006. **103**(46): p. 17137-42.

129. Patton, B.R., D. Burke, and M.J. Booth, *Adaptive optics from microscopy to nanoscopy*. Multiphoton Microscopy in the Biomedical Sciences Xiv, 2014. **8948**: p. 6.

130. Débarre, D., et al., *Adaptive optics for structured illumination microscopy.* Opt. Express, 2008. **16**(13): p. 9290-9305.

131. Izeddin, I., et al., *PSF shaping using adaptive optics for three-dimensional single-molecule super-resolution imaging and tracking.* Opt. Express, 2012. **20**(5): p. 4957-4967.

132. Patton, B.R., D. Burke, and M.J. Booth. *Adaptive optics from microscopy to nanoscopy*. in *Proc. SPIE*. 2014.

133. Burke, D., et al., *Adaptive optics correction of specimen-induced aberrations in single-molecule switching microscopy.* Optica, 2015. **2**(2): p. 177-185.

134. Tehrani, K.F., et al., *Adaptive optics stochastic optical reconstruction microscopy (AO-STORM) using a genetic algorithm.* Optics Express, 2015. **23**(10): p. 13677-13692.

135. Tucker, S., W.T. Cathey, and E. Dowski, Jr., *Extended depth of field and aberration control for inexpensive digital microscope systems.* Optics Express, 1999. **4**(11): p. 467-474.

136. Buchwalow, I.B. and W. Böcker, *Immunohistochemistry. [electronic resource] : basics and methods*. 2010: Berlin ; London : Springer, 2010.

137. Kapuscinski, J., *DAPI: a DNA-specific fluorescent probe.* Biotech Histochem, 1995. **70**(5): p. 220-33.

138. Cooper, J.A., *Effects of cytochalasin and phalloidin on actin.* The Journal of Cell Biology, 1987. **105**(4): p. 1473-1478.

139. Ataka, K. and V.A. Pieribone, *A Genetically Targetable Fluorescent Probe of Channel Gating with Rapid Kinetics.* Biophysical Journal, 2002. **82**(1): p. 509-516.

140. Fakhrudin, N., et al., *Computer-Aided Discovery, Validation, and Mechanistic Characterization of Novel Neolignan Activators of Peroxisome Proliferator-Activated Receptor γ.* Molecular Pharmacology, 2010. **77**(4): p. 559-566.

141. Freitag, M., et al., *GFP as a tool to analyze the organization, dynamics and function of nuclei and microtubules in Neurospora crassa.* Fungal Genetics and Biology, 2004. **41**(10): p. 897-910.

142. Lakowicz, J.R., *Principles of Fluorescence Spectroscopy*. 2006.

143. Creemers, T.M.H., et al., *Photophysics and optical switching in green fluorescent protein mutants.* Proceedings of the National Academy of Sciences, 2000. **97**(7): p. 2974-2978.

144. Zondervan, R., et al., *Photoblinking of Rhodamine 6G in Poly(vinyl alcohol): Radical Dark State Formed through the Triplet.* The Journal of Physical Chemistry A, 2003. **107**(35): p. 6770-6776.

145. Ando, R., H. Mizuno, and A. Miyawaki, *Regulated Fast Nucleocytoplasmic Shuttling Observed by Reversible Protein Highlighting.* Science, 2004. **306**(5700): p. 1370-1373.

146. Habuchi, S., et al., *Reversible single-molecule photoswitching in the GFP-like fluorescent protein Dronpa.* Proceedings of the National Academy of Sciences of the United States of America, 2005. **102**(27): p. 9511-9516.

147. Dedecker, P., et al., *Subdiffraction Imaging through the Selective Donut-Mode Depletion of Thermally Stable Photoswitchable Fluorophores: Numerical Analysis and Application to the Fluorescent Protein Dronpa.* Journal of the American Chemical Society, 2007. **129**(51): p. 16132-16141.

148. Flors, C., et al., *A Stroboscopic Approach for Fast Photoactivation−Localization Microscopy with Dronpa Mutants.* Journal of the American Chemical Society, 2007. **129**(45): p. 13970-13977.

149. Lukyanov, K.A., et al., *Photoactivatable fluorescent proteins.* Nat Rev Mol Cell Biol, 2005. **6**(11): p. 885-890.

150. Hess, S.T., et al., *Dynamic clustered distribution of hemagglutinin resolved at 40 nm in living cell membranes discriminates between raft theories.* Proceedings of the National Academy of Sciences, 2007. **104**(44): p. 17370-17375.

151. Verkhusha, V.V. and A. Sorkin, *Conversion of the Monomeric Red Fluorescent Protein into a Photoactivatable Probe.* Chemistry & Biology, 2005. **12**(3): p. 279-285.

152. Lippincott-Schwartz, J. and G.H. Patterson, *Fluorescent Proteins for Photoactivation Experiments*, in *Methods in Cell Biology*, F.S. Kevin, Editor. 2008, Academic Press. p. 45-61.

153. Ando, R., et al., *An optical marker based on the UV-induced green-to-red photoconversion of a fluorescent protein.* Proceedings of the National Academy of Sciences, 2002. **99**(20): p. 12651-12656.

154. Tsutsui, H., et al., *Semi-rational engineering of a coral fluorescent protein into an efficient highlighter.* 2005(1469-221X (Print)).

155. Wiedenmann, J., et al., *EosFP, a fluorescent marker protein with UV-inducible green-to-red fluorescence conversion.* Proceedings of the National Academy of Sciences of the United States of America, 2004. **101**(45): p. 15905-15910.

156. Hess, S.T., A.A. Heikal, and W.W. Webb, *Fluorescence Photoconversion Kinetics in Novel Green Fluorescent Protein pH Sensors (pHluorins).* The Journal of Physical Chemistry B, 2004. **108**(28): p. 10138-10148.

157. Bates, M., T. Blosser, and X. Zhuang, *Short-Range Spectroscopic Ruler Based on a Single-Molecule Optical Switch.* Physical Review Letters, 2005. **94**(10).

158. Irie, M., et al., *Organic chemistry: a digital fluorescent molecular photoswitch.* Nature, 2002. **420**(6917): p. 759-60.

159. Fukaminato, T., et al., *Digital Photoswitching of Fluorescence Based on the Photochromism of Diarylethene Derivatives at a Single-Molecule Level.* Journal of the American Chemical Society, 2004. **126**(45): p. 14843-14849.

160. Förster, T., *Zwischenmolekulare Energiewanderung und Fluoreszenz.* Annalen der Physik, 1948. **437**(1-2): p. 55-75.

161. Selvin, P.R., *[13] Fluorescence resonance energy transfer,* in *Methods in Enzymology*, S. Kenneth, Editor. 1995, Academic Press. p. 300-334.

162. Ha, T., et al., *Probing the interaction between two single molecules: fluorescence resonance energy transfer between a single donor and a single acceptor.* Proceedings of the National Academy of Sciences, 1996. **93**(13): p. 6264-6268.

163. Weiss, S., *Measuring conformational dynamics of biomolecules by single molecule fluorescence spectroscopy.* Nat Struct Biol, 2000. **7**(9): p. 724-9.

164. Zhuang, X., et al., *A Single-Molecule Study of RNA Catalysis and Folding.* Science, 2000. **288**(5473): p. 2048-2051.

165. Moerner, W.E. and D.P. Fromm, *Methods of single-molecule fluorescence spectroscopy and microscopy.* Review of Scientific Instruments, 2003. **74**(8): p. 3597-3619.

166. Heilemann, M., et al., *Carbocyanine Dyes as Efficient Reversible Single-Molecule Optical Switch.* Journal of the American Chemical Society, 2005. **127**(11): p. 3801-3806.

167. Vogelsang, J., et al., *A Reducing and Oxidizing System Minimizes Photobleaching and Blinking of Fluorescent Dyes.* Angewandte Chemie International Edition, 2008. **47**(29): p. 5465-5469.

168. Bagshaw, C.R. and D. Cherny, *Blinking fluorophores: what do they tell us about protein dynamics?* Biochem Soc Trans, 2006. **34**(Pt 5): p. 979-82.

169. van de Linde, S., et al., *Photoinduced formation of reversible dye radicals and their impact on super-resolution imaging.* Photochemical & Photobiological Sciences, 2011. **10**(4): p. 499-506.

170. Olivier, N., et al., *Simple buffers for 3D STORM microscopy.* Biomedical Optics Express, 2013. **4**(6): p. 885-899.

171. Dabbousi, B.O., et al., *(CdSe)ZnS Core−Shell Quantum Dots: Synthesis and Characterization of a Size Series of Highly Luminescent Nanocrystallites.* The Journal of Physical Chemistry B, 1997. **101**(46): p. 9463-9475.

172. Walling, M.A., J.A. Novak, and J.R.E. Shepard, *Quantum Dots for Live Cell and In Vivo Imaging.* International Journal of Molecular Sciences, 2009. **10**(2): p. 441-491.

173. Chan, W.C. and S. Nie, *Quantum dot bioconjugates for ultrasensitive nonisotopic detection.* Science, 1998. **281**(5385): p. 2016-8.

174. Goldman, E.R., et al., *Avidin: A Natural Bridge for Quantum Dot-Antibody Conjugates.* Journal of the American Chemical Society, 2002. **124**(22): p. 6378-6382.

175. Nagy, A., et al., *Comprehensive Analysis of the Effects of CdSe Quantum Dot Size, Surface Charge, and Functionalization on Primary Human Lung Cells.* ACS Nano, 2012. **6**(6): p. 4748-4762.

176. Bruchez, M., et al., *Semiconductor Nanocrystals as Fluorescent Biological Labels.* Science, 1998. **281**(5385): p. 2013-2016.

177. Mattoussi, H., G. Palui, and H.B. Na, *Luminescent quantum dots as platforms for probing in vitro and in vivo biological processes.* Advanced Drug Delivery Reviews, 2012. **64**(2): p. 138-166.

178. Leatherdale, C.A., et al., *On the Absorption Cross Section of CdSe Nanocrystal Quantum Dots.* J. Phys. Chem. B, 2002. **106**(31): p. 7619-7622.

179. Fernández-Suárez, M. and A.Y. Ting, *Fluorescent probes for superresolution imaging in living cells.* Nature Reviews Molecular Cell Biology, 2008. **9**: p. 929-943.

180. Huang, B., *Super-resolution optical microscopy: multiple choices.* Current Opinion in Chemical Biology, 2010. **14**(1): p. 10-14.

181. Patterson, G.H., *Fluorescence microscopy below the diffraction limit.* Seminars in Cell & Developmental Biology, 2009. **20**(8): p. 886-893.

182. Jianquan, X., et al., *Micelle-templated composite quantum dots for super-resolution imaging.* Nanotechnology, 2014. **25**(19): p. 195601.

183. Norris, D.J., M.G. Bawendi, and L.E. Brus, *Optical Properties of Semiconductor Nanocrystals (Quantum Dots)*, in *Molecular electronics A 'Chemistry for the 21st Sentury' Monograph*, J. Jortner and M. Ratner, Editors. p. 281-323.

184. Efros, A.L. and M. Rosen, *Random Telegraph Signal in the Photoluminescence Intensity of a Single Quantum Dot.* Physical Review Letters, 1997. **78**(6): p. 1110-1113.

185. Nirmal, M., et al., *Fluorescence intermittency in single cadmium selenide nanocrystals.* Nature, 1996. **383**(6603): p. 802-804.

186. Dertinger, T., et al., *Fast, background-free, 3D super-resolution optical fluctuation imaging (SOFI).* Proc. Natl. Acad. Sci. U. S. A., 2009. **106**(52): p. 22287-22292.

187. Watanabe, T.M., et al., *Real-time nanoscopy by using blinking enhanced quantum dots.* Biophys J, 2010. **99**(7): p. L50-2.

188. Wang, Y., et al., *3D Super-Resolution Imaging with Blinking Quantum Dots.* Nano Lett., 2013. **13**(11): p. 5233-5241.

189. Fan, Q., et al. *Photo-switchable quantum dots based on reversible FRET*. 2014.

190. van Sark, W., et al., *Blueing, bleaching, and blinking of single CdSe/ZnS quantum dots.* Chemphyschem, 2002. **3**(10): p. 871-879.

191. Tehrani, K.F., J. Xu, and P.A. Kner. *Multi-color quantum dot stochastic optical reconstruction microscopy (qSTORM)*. 2015.

192. Manley, S., J. Gunzenhäuser, and N. Olivier, *A starter kit for point-localization super-resolution imaging.* Current Opinion in Chemical Biology, 2011. **15**(6): p. 813-821.

193. Ha, T., *Single-Molecule Fluorescence Resonance Energy Transfer.* Methods, 2001. **25**(1): p. 78-86.

194. Aitken, C.E., R.A. Marshall, and J.D. Puglisi, *An Oxygen Scavenging System for Improvement of Dye Stability in Single-Molecule Fluorescence Experiments.* Biophysical Journal, 2008. **94**(5): p. 1826-1835.

195. Iwane, A.H., et al., *Single molecular assay of individual ATP turnover by a myosin-GFP fusion protein expressed in vitro.* FEBS Lett, 1997. **407**(2): p. 235-8.

196. Yasuda, R., et al., *F1-ATPase is a highly efficient molecular motor that rotates with discrete 120 degree steps.* Cell, 1998. **93**(7): p. 1117-24.

197. Kishino, A. and T. Yanagida, *Force measurements by micromanipulation of a single actin filament by glass needles.* Nature, 1988. **334**(6177): p. 74-76.

198. Bates, M., T.R. Blosser, and X. Zhuang, *Short-Range Spectroscopic Ruler Based on a Single-Molecule Optical Switch.* Physical Review Letters, 2005. **94**(10): p. 108101.

199. Dempsey, G.T., et al., *Photoswitching Mechanism of Cyanine Dyes.* Journal of the American Chemical Society, 2009. **131**(51): p. 18192-18193.

200. van de Linde, S., et al., *Direct stochastic optical reconstruction microscopy with standard fluorescent probes.* Nat. Protocols, 2011. **6**(7): p. 991-1009.

201. Jones, S.A., et al., *Fast, three-dimensional super-resolution imaging of live cells.* Nat Meth, 2011. **8**(6): p. 499-505.

202. Folling, J., et al., *Fluorescence nanoscopy by ground-state depletion and single-molecule return.* Nat Methods, 2008. **5**(11): p. 943-5.

203. Deschenes, L.A. and D.A. Vanden Bout, *Single-Molecule Studies of Heterogeneous Dynamics in Polymer Melts Near the Glass Transition.* Science, 2001. **292**: p. 255.

204. Weston, K.D., et al., *Single-molecule detection fluorescence of surface-bound species in vacuum.* Chemical Physics Letters, 1999. **308**(1–2): p. 58-64.

205. Cheezum, M.K., W.F. Walker, and W.H. Guilford, *Quantitative comparison of algorithms for tracking single fluorescent particles.* Biophysical Journal, 2001. **81**(4): p. 2378-2388.

206. Lacoste, T.D., et al., *Ultrahigh-resolution multicolor colocalization of single fluorescent probes.* Proceedings of the National Academy of Sciences of the United States of America, 2000. **97**(17): p. 9461-9466.

207. Michalet, X. and S. Weiss, *Using photon statistics to boost microscopy resolution.* Proceedings of the National Academy of Sciences of the United States of America, 2006. **103**(13): p. 4797-4798.

208. Bobroff, N., *Position measurement with a resolution and noise-limited instrument.* Review of Scientific Instruments, 1986. **57**(6): p. 1152-1157.

209. Adler, J. and S. Pagakis, *Reducing image distortions due to temperature-related microscope stage drift.* J Microsc, 2003. **210**: p. 131 - 137.

210. Carter, A., et al., *Stabilization of an optical microscope to 0.1 nm in three dimensions.* Appl Opt, 2007. **46**: p. 421 - 427.

211. Pertsinidis, A., Y. Zhang, and S. Chu, *Subnanometre single-molecule localization, registration and distance measurements.* Nature, 2010. **466**: p. 647 - 651.

212. Mennella, V., et al., *Subdiffraction-resolution fluorescence microscopy reveals a domain of the centrosome critical for pericentriolar material organization.* Nat Cell Biol, 2012. **14**: p. 1159 - 1168.

213. Mlodzianoski, M., et al., *Sample drift correction in 3D fluorescence photoactivation localization microscopy.* Opt Express, 2011. **19**: p. 15009 - 15019.

214. Mcgorthy, R., D. Kamiyama, and B. Huang, *Active microscope stabilization in three dimensions using image correlation.* Optical Nanoscopy, 2013. **2**: p. 2 - 3.

215. Xu, K., H. Babcock, and X. Zhuang, *Dual-objective STORM reveals three-dimensional filament organization in the actin cytoskeleton.* Nat Methods, 2012. **9**: p. 185 - 188.

216. Zessin, P.J.M., et al., *A hydrophilic gel matrix for single-molecule super-resolution microscopy.* Optical Nanoscopy, 2013. **2**(4): p. 1-8.

217. Banterle, N., et al., *Fourier ring correlation as a resolution criterion for super-resolution microscopy.* Journal of Structural Biology, 2013. **183**(3): p. 363-367.

218. Saxton, W.O. and W. Baumeister, *The correlation averaging of a regularly arranged bacterial cell envelope protein.* Journal of Microscopy, 1982. **127**(2): p. 127-138.

219. York, A.G., et al., *Confined activation and subdiffractive localization enables whole-cell PALM with genetically expressed probes.* Nature methods, 2011. **8**(4): p. 327-33.

220. Niu, L. and J. Yu, *Investigating Intracellular Dynamics of FtsZ Cytoskeleton with Photoactivation Single-Molecule Tracking.* Biophysical Journal. **95**(4): p. 2009-2016.

221. Henriques, R., et al., *QuickPALM: 3D real-time photoactivation nanoscopy image processing in ImageJ.* Nat Meth, 2010. **7**(5): p. 339-40.

222. Wolter, S., et al., *Real-time computation of subdiffraction-resolution fluorescence images.* Journal of Microscopy, 2010. **237**(1): p. 12-22.

223. Izeddin, I., et al., *Wavelet analysis for single molecule localization microscopy.* Optics Express, 2012. **20**(3): p. 2081-2095.

224. Shim, S.-H., et al., *Super-resolution fluorescence imaging of organelles in live cells with photoswitchable membrane probes.* Proc Natl Acad Sci U S A, 2012. **109**(35): p. 13978-13983.

225. van de Linde, S., et al., *The effect of photoswitching kinetics and labeling densities on super-resolution fluorescence imaging.* J. Biotechnol., 2010. **149**(4): p. 260-6.

226. Geyer, F.C., et al., *Genomic profiling of mitochondrion-rich breast carcinoma: chromosomal changes may be relevant for mitochondria accumulation and tumour biology.* Breast Cancer Research and Treatment, 2012. **132**(1): p. 15-28.

227. Grupp, K., et al., *High mitochondria content is associated with prostate cancer disease progression.* Molecular Cancer, 2013. **12**: p. 11.

228. Hall, C.J., et al., *Epidermal cells help coordinate leukocyte migration during inflammation through fatty acid-fuelled matrix metalloproteinase production.* Nat Commun, 2014. **5**.

229. Shtengel, G., et al., *Interferometric fluorescent super-resolution microscopy resolves 3D cellular ultrastructure.* Proc Natl Acad Sci U S A, 2009. **106**(9): p. 3125-30.

230. Juette, M.F., et al., *Three-dimensional sub-100 nm resolution fluorescence microscopy of thick samples.* Nat Meth, 2008. **5**(6): p. 527-529.

231. Ram, S., et al., *High accuracy 3D quantum dot tracking with multifocal plane microscopy for the study of fast intracellular dynamics in live cells.* Biophys J, 2008. **95**(12): p. 6025-43.

232. Revelo, N.H., et al., *A new probe for super-resolution imaging of membranes elucidates trafficking pathways.* The Journal of Cell Biology, 2014. **205**(4): p. 591-606.

233. Bock, H., et al., *Two-color far-field fluorescence nanoscopy based on photoswitchable emitters.* Applied Physics B, 2007. **88**(2): p. 161-165.

234. Shroff, H., et al., *Dual-color superresolution imaging of genetically expressed probes within individual adhesion complexes.* Proceedings Of The National Academy Of Sciences Of The United States Of America, 2007. **104**(51): p. 20308-20313.

235. Bates, M., et al., *Multicolor super-resolution imaging with photo-switchable fluorescent probes.* Science, 2007. **317**(5845): p. 1749-1753.

236. Huang, B., et al., *Whole-cell 3D STORM reveals interactions between cellular structures with nanometer-scale resolution.* Nature Methods, 2008. **5**(12): p. 1047-1052.

237. van Sark, W.G.J.H.M., et al., *Blueing, Bleaching, and Blinking of Single CdSe/ZnS Quantum Dots.* ChemPhysChem, 2002. **3**(10): p. 871-879.

238. Shroff, H., et al., *Live-cell photoactivated localization microscopy of nanoscale adhesion dynamics.* Nat. Methods, 2008. **5**: p. 417-423.

239. Heilemann, M., et al., *Subdiffraction-Resolution Fluorescence Imaging with Conventional Fluorescent Probes.* Angew. Chem. Int. Ed., 2008. **47**(33): p. 6172-6176.

240. Weber, K., P.C. Rathke, and M. Osborn, *Cytoplasmic microtubular images in glutaraldehyde-fixed tissue culture cells by electron microscopy and by immunofluorescence microscopy.* Proc Natl Acad Sci U S A, 1978. **75**(4): p. 1820-1824.

241. Heilemann, M., et al., *Super-Resolution Imaging with Small Organic Fluorophores.* Angew. Chem. Int. Ed., 2009. **48**(37): p. 6903-6908.

242. Ries, J., et al., *A simple, versatile method for GFP-based super-resolution microscopy via nanobodies.* Nat Meth, 2012. **9**(6): p. 582-4.

243. Vaughan, J.C., S. Jia, and X.W. Zhuang, *Ultrabright photoactivatable fluorophores created by reductive caging.* Nature Methods, 2012. **9**(12): p. 1181-U135.

244. Dempsey, G.T., et al., *Photoswitching mechanism of cyanine dyes.* J. Am. Chem. Soc., 2009. **131**(51): p. 18192-3.

245. Rust, M.J., M. Bates, and X. Zhuang, *Sub-diffraction-limit imaging by stochastic optical reconstruction microscopy (STORM).* Nat. Methods, 2006. **3**(10): p. 793-796.

246. van de Linde, S., et al., *The effect of photoswitching kinetics and labeling densities on super-resolution fluorescence imaging.* J Biotechnol, 2010. **149**(4): p. 260-6.

247. Li, Z., et al., *The importance of dendritic mitochondria in the morphogenesis and plasticity of spines and synapses.* Cell, 2004. **119**(6): p. 873-87.

248. Boldogh, I.R. and L.A. Pon, *Mitochondria on the move.* Trends Cell Biol, 2007. **17**(10): p. 502-10.

249. Saxton, W.M. and P.J. Hollenbeck, *The axonal transport of mitochondria.* Journal of Cell Science, 2012. **125**(9): p. 2095-2104.

250. Karbowski, M. and R.J. Youle, *Dynamics of mitochondrial morphology in healthy cells and during apoptosis.* Cell Death Differ., 2003. **10**(8): p. 870-80.

251. Medda, R., et al., *4Pi microscopy of quantum dot-labeled cellular structures.* J Struct Biol, 2006. **156**(3): p. 517-23.

252. Wilson, T. and C. Sheppard, *Theory and practice of scanning optical microscopy*. 1984: London ; Orlando : Academic Press, 1984.

253. Bourgenot, C., et al., *Comparison of closed loop and sensorless adaptive optics in widefield optical microscopy*. Journal of the European Optical Society - Rapid publications. Vol. 8. 2013.

254. Booth, M.J., *Adaptive optical microscopy: the ongoing quest for a perfect image.* Light-Science & Applications, 2014. **3**: p. 7.

255. Choi, W., et al., *Tomographic phase microscopy.* Nat Methods, 2007. **4**(9): p. 717-9.

256. Jacobsen, H. and S.W. Hell, *Effect of the specimen refractive index on the imaging of a confocal fluorescence microscope employing high aperture oil immersion lenses.* Bioimaging, 1995. **3**(1): p. 39-47.

257. Shaw, P.J. and D.J. Rawlins, *The point-spread function of a confocal microscope: its measurement and use in deconvolution of 3-D data.* Journal of Microscopy, 1991. **163**(2): p. 151-165.

258. Carlsson, K., *The influence of specimen refractive index, detector signal integration, and non-uniform scan speed on the imaging properties in confocal microscopy.* Journal of Microscopy, 1991. **163**(2): p. 167-178.

259. Visser, T.D., J.L. Oud, and G.J. Brakenhoff, *Refractive index and axial distance measurements in 3-D microscopy.* SPIE MILESTONE SERIES MS, 1996. **131**: p. 286-289.

260. Schwertner, M., M.J. Booth, and T. Wilson, *Simulation of specimen-induced aberrations for objects with spherical and cylindrical symmetry.* J. Microsc., 2004. **215**(3): p. 271-280.

261. Schwertner, M., M.J. Booth, and T. Wilson, *Specimen-induced distortions in light microscopy.* Journal of Microscopy, 2007. **228**(1): p. 97-102.

262. Born, M., et al., *Principles of Optics: Electromagnetic Theory of Propagation, Interference and Diffraction of Light.* 1999: Cambridge University Press.

263. Braat, J.J.M. and A.J.E.M. Janssen, *Derivation of various transfer functions of ideal or aberrated imaging systems from the three-dimensional transfer function.* Journal of the Optical Society of America A, 2015. **32**(6): p. 1146-1159.

264. WYANT, J.C., *Basic Wavefront Aberration Theory for Optical Metrology*, in *APPLIED OPTICS AND OPTICAL ENGINEERING*. 1992. p. 28-39.

265. Booth, M.J., *Wavefront sensorless adaptive optics for large aberrations.* Optics Letters, 2007. **32**(1): p. 5-7.

266. Lukosz, W., *Der Einfluß der Aberrationen auf die Optische Übertragungsfunktion bei Kleinen Orts-Frequenzen.* Optica Acta: International Journal of Optics, 1963. **10**(1): p. 1-19.

267. Braat, J., *Polynomial expansion of severely aberrated wave fronts.* Journal of the Optical Society of America A, 1987. **4**(4): p. 643-650.

268. Mahajan, V.N., *Strehl ratio for primary aberrations in terms of their aberration variance.* Journal of the Optical Society of America, 1983. **73**(6): p. 860-861.

269. Maurer, C., et al., *What spatial light modulators can do for optical microscopy.* Laser & Photonics Reviews, 2011. **5**(1): p. 81-101.

270. Neff, J.A., R.A. Athale, and S.H. Lee, *Two-dimensional spatial light modulators: a tutorial.* Proceedings of the IEEE, 1990. **78**(5): p. 826-855.

271. Cho, D.J., et al., *Characteristics of a 128×128 liquid-crystal spatial light modulator for wave-front generation.* Optics Letters, 1998. **23**(12): p. 969-971.

272. Mu, Q., et al., *An adaptive optics imaging system based on a high-resolution liquid crystal on silicon device.* Optics Express, 2006. **14**(18): p. 8013-8018.

273. Török, P. and F.-J. Kao, *Optical imaging and microscopy. [electronic resource] : techniques and advanced systems*. Springer series in optical sciences: v. 87. 2007: Berlin ; New York : Springer, c2007. 2nd rev. ed.

274. Birch, P.M., R. Young, and C. Chatwin, *Spatial Light Modulators (SLMs)*, in *Optical and Digital Image Processing*. 2011, Wiley-VCH Verlag GmbH & Co. KGaA. p. 179-200.

275. Conkey, D.B., A.M. Caravaca-Aguirre, and R. Piestun, *High-speed scattering medium characterization with application to focusing light through turbid media.* Optics Express, 2012. **20**(2): p. 1733-1740.

276. Zhang, X. and P. Kner, *Binary wavefront optimization using a genetic algorithm.* J. Opt., 2014. **16**(12): p. 125704.

277. Kubby, J., *Wavefront Correctors*, in *Adaptive Optics for Biological Imaging*. 2013, CRC Press. p. 109-149.

278. Southwell, W.H., *Wave-front estimation from wave-front slope measurements.* Journal of the Optical Society of America, 1980. **70**(8): p. 998-1006.

279. Platt, B.C. and R. Shack, *History and principles of Shack-Hartmann wavefront sensing.* J Refract Surg, 2001. **17**(5): p. S573-7.

280. Vérinaud, C., *On the nature of the measurements provided by a pyramid wave-front sensor*. Optics Communications, 2004. **233**(1–3): p. 27-38.

281. Roddier, F., C. Roddier, and N. Roddier. *Curvature Sensing: A New Wavefront Sensing Method*. 1988.

282. Beverage, J.L., R.V. Shack, and M.R. Descour, *Measurement of the three-dimensional microscope point spread function using a Shack-Hartmann wavefront sensor.* J Microsc, 2002. **205**(Pt 1): p. 61-75.

283. Azucena, O., et al. *Implementation of a Shack-Hartmann wavefront sensor for the measurement of embryo-induced aberrations using fluorescent microscopy*. in *MEMS Adaptive Optics III*. 2009. San Jose, CA, USA: SPIE.

284. Tao, X., et al., *Adaptive optics microscopy with direct wavefront sensing using fluorescent protein guide stars.* Opt Lett, 2011. **36**: p. 3389-3391.

285. Aviles-Espinosa, R., et al., *Measurement and correction of in vivo sample aberrations employing a nonlinear guide-star in two-photon excited fluorescence microscopy.* Biomed Opt Express, 2011. **2**: p. 3135-3149.

286. Cha, J.W., J. Ballesta, and P.T. So, *Shack-Hartmann wavefront-sensor-based adaptive optics system for multiphoton microscopy.* Journal of Biomedical Optics, 2010. **15**(4): p. 046022.

287. Rahman, S.A. and M.J. Booth, *Direct wavefront sensing in adaptive optical microscopy using backscattered light.* Applied Optics, 2013. **52**(22): p. 5523-5532.

288. Tao, X., et al., *Adaptive optics confocal microscopy using direct wavefront sensing.* Opt Lett, 2011. **36**: p. 1062-1064.

289. Jorand, R., et al., *Deep and clear optical imaging of thick inhomogeneous samples.* PLoS ONE, 2012. **7**: p. e35795.

290. Tao, X., et al., *Live imaging using adaptive optics with fluorescent protein guide-stars.* Opt. Express, 2012. **20**(14): p. 15969-15982.

291. Azucena, O., et al., *Wavefront aberration measurements and corrections through thick tissue using fluorescent microsphere reference beacons.* Opt. Express, 2010. **18**(16): p. 17521-17532.

292. Vermeulen, P., et al., *Adaptive optics for fluorescence wide-field microscopy using spectrally independent guide star and markers.* J Biomed Opt, 2011. **16**(7): p. 076019.

293. Neal, D.R., J. Copland, and D.A. Neal. *Shack-Hartmann wavefront sensor precision and accuracy*. 2002.

294. Chew, T.Y., R.M. Clare, and R.G. Lane, *A comparison of the Shack–Hartmann and pyramid wavefront sensors.* Optics Communications, 2006. **268**(2): p. 189-195.

295. Wang, J., et al., *Measuring aberrations in the rat brain by coherence-gated wavefront sensing using a Linnik interferometer.* Biomed Opt Express, 2012. **3**: p. 2510-2525.

296. Tuohy, S. and A.G. Podoleanu, *Depth-resolved wavefront aberrations using a sensor.* Opt Express, 2010. **18**: p. 3458-3476.

297. Feierabend, M., M. Rückel, and W. Denk, *Coherence-gated wave-front sensing in strongly scatteringsamples.* Optics Letters, 2004. **29**(19): p. 2255-2257.

298. Rueckel, M. and W. Denk, *Properties of coherence-gated wavefront sensing.* Journal of the Optical Society of America A, 2007. **24**(11): p. 3517-3529.

299. Korkiakoski, V., et al., *Comparison between a model-based and a conventional pyramid sensor reconstructor.* Applied Optics, 2007. **46**(24): p. 6176-6184.

300. Iglesias, I. and F. Vargas-Martin, *Quantitative phase microscopy of transparent samples using a liquid crystal display.* Journal of Biomedical Optics, 2013. **18**(2): p. 026015-026015.

301. Hanser, B.M., et al., *Phase retrieval for high-numerical-aperture optical systems.* Optics Letters, 2003. **28**(10): p. 801-3.

302. Hanser, B.M., et al., *Phase-retrieved pupil functions in wide-field fluorescence microscopy.* J Microsc, 2004. **216**(Pt 1): p. 32-48.

303. Deming, R.W., *Phase retrieval from intensity-only data by relative entropy minimization.* J. Opt. Soc. Am. A, 2007. **24**(11): p. 3666-3679.

304. Kner, P., et al., *Closed loop adaptive optics for microscopy without a wavefront sensor.* Three-Dimensional and Multidimensional Microscopy: Image Acquisition and Processing Xvii, 2010. **7570**.

305. Gonsalves, R.A., *Phase retrieval and diversity in adaptive optics.* Optical Engineering, 1982. **21**: p. 829-832.

306. Paxman, R.G., et al., *Evaluation of phase-diversity techniques for solar-image restoration.* Astrophysical Journal, 1996. **466**(2): p. 1087-1096.

307. Kner, P., *Adaptive optics for biological microscopy using phase diversity.* Mems Adaptive Optics Vi, 2012. **8253**.

308. Bourgenot, C., et al., *3D adaptive optics in a light sheet microscope.* Optics Express, 2012. **20**(12): p. 13252-13261.

309. Debarre, D., et al., *Adaptive optics for structured illumination microscopy.* Opt Express, 2008. **16**: p. 9290-9305.

310. Debarre, D., et al., *Image-based adaptive optics for two-photon microscopy.* Opt Lett, 2009. **34**: p. 2495-2497.

311. Jesacher, A., et al., *Adaptive harmonic generation microscopy of mammalian embryos.* Opt Lett, 2009. **34**: p. 3154-3156.

312. Olivier, N., D. Debarre, and E. Beaurepaire, *Dynamic aberration correction for multiharmonic microscopy.* Opt Lett, 2009. **34**: p. 3145-3147.

313. Gould, T.J., et al., *Adaptive optics enables 3D STED microscopy in aberrating specimens.* Opt. Express, 2012. **20**(19): p. 20998-21009.

314. Booth, M.J., D. Débarre, and T. Wilson, *Image-based wavefront sensorless adaptive optics.* Proc. SPIE, 2007. **6711**: p. 671102-671102-7.

315. Ji, N., D.E. Milkie, and E. Betzig, *Adaptive optics via pupil segmentation for high-resolution imaging in biological tissues.* Nat Methods, 2010. **7**(2): p. 141-7.

316. Ji, N., T.R. Sato, and E. Betzig, *Characterization and adaptive optical correction of aberrations during in vivo imaging in the mouse cortex.* Proc Natl Acad Sci USA, 2012. **109**: p. 22-27.

317. Scrimgeour, J. and J.E. Curtis, *Aberration correction in wide-field fluorescence microscopy by segmented-pupil image interferometry.* Opt Express, 2012. **20**: p. 14534-14541.

318. Conkey, D.B., et al., *Genetic algorithm optimization for focusing through turbid media in noisy environments.* Opt. Express, 2012. **20**(5): p. 4840-4849.

319. Wright, A.J., et al., *Exploration of the optimisation algorithms used in the implementation of adaptive optics in confocal and multiphoton microscopy.* Microsc Res Tech, 2005. **67**(1): p. 36-44.

320. Sherman, L., et al., *Adaptive correction of depth-induced aberrations in multiphoton scanning microscopy using a deformable mirror.* J. Microsc., 2002. **206**(Pt 1): p. 65-71.

321. Xiaolong, Z. and K. Peter, *Binary wavefront optimization using a genetic algorithm.* Journal of Optics, 2014. **16**(12): p. 125704.

322. Booth, M.J., *Wave front sensor-less adaptive optics: a model-based approach using sphere packings.* Opt. Express, 2006. **14**(4): p. 1339-1352.

323. Albert, O., et al., *Smart microscope: an adaptive optics learning system for aberration correction in multiphoton confocal microscopy.* Opt. Lett., 2000. **25**(1): p. 52-54.

324. Débarre, D., et al., *Image-based adaptive optics for two-photon microscopy.* Opt. Lett., 2009. **34**(16): p. 2495-2497.

325. Thomas, B., et al., *Enhanced resolution through thick tissue with structured illumination and adaptive optics.* Journal of Biomedical Optics, 2015. **20**(2): p. 026006-026006.

326. Debarre, D., M.J. Booth, and T. Wilson, *Image based adaptive optics through optimisation of low spatial frequencies.* Opt. Express, 2007. **15**(13): p. 8176-8190.

327. Fienup, J.R. and J.J. Miller, *Aberration correction by maximizing generalized sharpness metrics.* J. Opt. Soc. Am. A, 2003. **20**(4): p. 609-620.

328. Kner, P., et al. *Closed loop adaptive optics for microscopy without a wavefront sensor*. in *SPIE (Three-Dimensional and Multidimensional Microscopy: Image Acquisition and Processing XVII)*. 2010. San Francisco, California, USA: SPIE.

329. Kennedy, J., R.C. Eberhart, and Y. Shi, *chapter seven - The Particle Swarm*, in *Swarm Intelligence*, J. Kennedy and R.C.E. Shi, Editors. 2001, Morgan Kaufmann: San Francisco. p. 287-325.

330. Blum, C. and D. Merkle, *Swarm intelligence : introduction and applications*. Natural computing series. 2008: Berlin ; London : Springer, 2008.

331. Nieuwenhuizen, R.P.J., et al., *Measuring image resolution in optical nanoscopy.* Nat Meth, 2013. **10**(6): p. 557-562.

332. Xu, J., K.F. Tehrani, and P. Kner, *Multicolor 3D super-resolution imaging by quantum dot stochastic optical reconstruction microscopy.* ACS Nano, 2015. **9**: p. 2917-2925.

333. Goodman, J.W., *Introduction to Fourier optics*. 2 ed. McGraw-Hill Series in Electrical and Computer Engineering, ed. S.W. Director. 1996, Boston, Massachusetts: McGraw-Hill.

334. Wyant, J.C., *Basic wavefront aberration theory for optical metrology*, in *Applied Optics and Optical Engineering*, R.R. Shannon and J.C. Wyant, Editors. 1992, Academic Press. p. 28-39.

335. Koza, J.R., *Genetic Programming: On the Programming of Computers by Means of Natural Selection (Complex Adaptive Systems)*. 6th ed. 1998: Bradford.

336. Deb, K., et al., *A fast and elitist multiobjective genetic algorithm: NSGA-II.* Evolutionary Computation, IEEE Transactions on, 2002. **6**(2): p. 182-197.

337. Deb, K. and D. Deb, *Analysing mutation schemes for real-parameter genetic algorithms.* Int. J. Artif. Intell. Soft Comput., 2014. **4**(1): p. 1-28.

338. Fortin, F.-A., et al., *DEAP: Evolutionary algorithms made easy* J. Mach. Learn. Res., 2012. **13**: p. 2171-2175.

339. Mahajan, V.N., *Strehl ratio for primary aberrations in terms of their aberration variance*. J. Opt. Soc. Am., 1983. **73**(6): p. 860-861.

340. Shen, P. and H.N. Cai, *Drosophila neuropeptide F mediates integration of chemosensory stimulation and conditioning of the nervous system by food.* J Neurobiol, 2001. **47**(1): p. 16-25.

341. Leonard, B. and A. Engelbrecht, *Scalability Study of Particle Swarm Optimizers in Dynamic Environments*, in *Swarm Intelligence*, M. Dorigo, et al., Editors. 2012, Springer Berlin Heidelberg. p. 121-132.

342. Fortin, F.-A., et al., *DEAP: Evolutionary Algorithms Made Easy.* Journal of Machine Learning Research, 2012. **13**: p. 2171-2175.

343. Thompson, R.E., D.R. Larson, and W.W. Webb, *Precise nanometer localization analysis for individual fluorescent probes.* Biophys. J., 2002. **82**(5): p. 2775-2783.

344. Goodman, J.W., *Statistical Optics*. 1 ed. Wiley series in pure and applied optics. 1985, New York: Wiley Interscience. 550.

345. York, A.G., et al., *Confined activation and subdiffractive localization enables whole-cell PALM with genetically expressed probes.* Nat. Methods, 2011. **8**(4): p. 327-33.

346. Shao, L., et al., *Super-resolution 3D microscopy of live whole cells using structured illumination.* Nat. Methods, 2011. **8**(12): p. 1044-6.

347. Wolter, S., et al., *Real-time computation of subdiffraction-resolution fluorescence images.* J. Microsc., 2010. **237**(1): p. 12-22.